University of Windsor
Scholarship at UWindsor

Electronic Theses and Dissertations | Theses, Dissertations, and Major Papers

1-1-2019

Lumped Parameter Thermal Network Modelling for Thermal Characterization and Protection of Traction Motors in Electric Vehicle Application

Firoz Uddin Ahmed
University of Windsor

Follow this and additional works at: https://scholar.uwindsor.ca/etd

Recommended Citation

Ahmed, Firoz Uddin, "Lumped Parameter Thermal Network Modelling for Thermal Characterization and Protection of Traction Motors in Electric Vehicle Application" (2019). *Electronic Theses and Dissertations*. 8156.
https://scholar.uwindsor.ca/etd/8156

This online database contains the full-text of PhD dissertations and Masters' theses of University of Windsor students from 1954 forward. These documents are made available for personal study and research purposes only, in accordance with the Canadian Copyright Act and the Creative Commons license—CC BY-NC-ND (Attribution, Non-Commercial, No Derivative Works). Under this license, works must always be attributed to the copyright holder (original author), cannot be used for any commercial purposes, and may not be altered. Any other use would require the permission of the copyright holder. Students may inquire about withdrawing their dissertation and/or thesis from this database. For additional inquiries, please contact the repository administrator via email (scholarship@uwindsor.ca) or by telephone at 519-253-3000ext. 3208.

Lumped Parameter Thermal Network Modelling for Thermal Characterization and Protection of Traction Motors in Electric Vehicle Application

By

Firoz Uddin Ahmed

A Dissertation
Submitted to the Faculty of Graduate Studies
through the Department of Electrical & Computer Engineering
in Partial Fulfillment of the Requirements for
the Degree of Doctor of Philosophy
at the University of Windsor

Windsor, Ontario, Canada

2019

© 2019 Firoz Uddin Ahmed

Lumped Parameter Thermal Network Modelling for Thermal Characterization and Protection of Traction Motors in Electric Vehicle Application

by

Firoz Uddin Ahmed

APPROVED BY:

_____

M. Nasir Uddin, External Examiner
Lakehead University

_____

V. Stoilov
Department of Mechanical, Automotive & Materials Engineering

_____

M. Ahmadi
Department of Electrical & Computer Engineering

_____

M. Azzouz
Department of Electrical & Computer Engineering

_____

N. Kar, Advisor
Department of Electrical & Computer Engineering

December 13th, 2019

DECLARATION OF CO-AUTHORSHIP /PREVIOUS PUBLICATIONS

I hereby declare that this dissertation incorporates material from joint research work with Dr. Narayan C. Kar, Dr. Eshan Ghosh, Dr. Mahdi Sangdehi, Pratik Roy, Ali Towhidi, S. Mukundan and H. Dhulipati from University of Windsor, Ontario. In all cases, only primary contribution of the author towards these publications are included in the dissertation. The contributions of co-authors were primarily the assistance and guidance in experimentation, manuscript review and improvement.

I am aware of the University of Windsor Policy on Authorship and I certify that I acknowledge the contribution of the researchers in my dissertation and I have received written permission from each of the co-author(s) to include the above-mentioned published material in the dissertation. I certify that, with the above qualifications, this dissertation is the product of my own work.

The dissertation includes selected sections and complete research work conducted in four original papers that have published/submitted in peer reviewed IEEE Transactions and international conferences, as follows:

Dissertation Chapter	Publication title/full citation	Publication status
Chapter 2	**F. Ahmed**, E. Ghosh, and N. C. Kar, " Transient Thermal Analysis of a Copper Rotor Induction Motor using a Lumped Parameter Temperature Network Model," in *IEEE Transportation Electrification Conference and Expo (ITEC)*, Michigan, USA, June 2016.	*Published*
Chapter 3	**F. Ahmed**, N. C. Kar, "Analysis of End-Winding Thermal Effects in a Totally Enclosed Fan-Cooled Induction Motor with a Die Cast Copper Rotor," *IEEE Transactions on Industry Applications*, Vol. 53, No. 3, May 2017.	*Published*
	F. Ahmed, P. Roy, M. Towhidi, G. Feng and N. C. Kar, "CFD and LPTN Hybrid Technique to Determine Convection Coefficient in End-winding of TEFC Induction	*Published*

Chapter 4	Motor with Copper Rotor," IECON - 45th Annual Conference of the IEEE Industrial Electronics Society, Portugal, October 2019.	
Chapter 5	**F. Ahmed**, E. Ghosh, S. Mukundan, H. Dhulipati, and N. C. Kar, "LPTN and FEA Modelling for Thermal Characterization of an Interior Permanent Magnet Synchronous Motor (IPMSM) for Electric Vehicle Application," *Energy and Sustainability Conference*, Windsor, ON, Canada, June 2018.	*Presented*
Chapter 5	**F. Ahmed**, E. Ghosh, M. Towhidi, S. Mukundan, H. Dhulipati, and N. C. Kar, "LPTN Modelling for Thermal Characterization and Protection of an Interior Permanent Magnet Synchronous Motor (IPMSM) for Electric Vehicle Application.," submitted in the Journal of Engineering (IET), JOE-2019-1294.	Submitted

I hereby certify that I have obtained a written permission from the copyright owners to include the published material in the dissertation. I certify that the research work has been completed during my study as a graduate student at the University of Windsor.

I certify that, to the best of my knowledge, my dissertation does not interfere with anyone's copyright nor violate any proprietary rights and any ideas, techniques, quotations and any related material from research work of other people included in the dissertation, published or otherwise, are fully acknowledged in accordance with the standard referencing practices. Furthermore, to the extent that I have included copyrighted material that surpasses the bounds of fair dealing within the meaning of the Canada Copyright Act, I certify that I have obtained a written permission from the copyright owner(s) to these material in the dissertation and all the copies of copyright permissions are included in the appendices.

I hereby declare that this is a true copy of my dissertation, including any final revisions, as approved by the committee and the graduate studies office, and that this dissertation has not been submitted to any other University or Institution.

ABSTRACT

This thesis investigates thermal modelling of traction motors for thermal characterization and protection in electric vehicle application. The requirements for traction motor characteristics include high power density; high torque at low speed for starting and climbing; high power at high speed for cruising; wide speed range; a fast torque response; high efficiency over wide torque and speed ranges and high reliability. High torque and power density requirements in traction motors mean increasing current and consequently, higher temperature rise in the motor. When the temperature of the winding and magnet in traction motors exceed permissible thermal limit frequently due to lack of proper understanding and managing of the thermal conditions it will have a short-term and a long term impacts on the motor operation. In the short-term, it will never be able to produce required torque and power for standard driving conditions of electric vehicle. In the long-term, it will have the detrimental effects on the life of insulation material and consequently, it will cause permanent insulation breakdown and on the other hand, demagnetization due to higher temperature will cause a permanent damage to the motor. Hence, it is extremely important to predict temperature rise in the motor accurately and regulate liquid cooling accordingly so that the motor does not fail to produce required torque and power for any driving conditions. This research work proposes a higher order lumped parameter thermal network (LPTN) model to determine a comprehensive thermal characterization of the traction motors. Such characterization predicts the temperature of the winding, magnet and other parts of the motor. The proposed model is capable of taking inputs dynamically of motor operating parameters in electric vehicle and generate a motor loss model that feeds loss results into LPTN thermal model to predict motor temperature. The proposed model investigates cooling requirements to the motor so that the motor continues to produce the rated torque and power. The LPTN model results are validated through thermal tests on a copper rotor induction motor (CRIM) and an interior permanent magnet synchronous motor (IPMSM) in the laboratory.

DEDICATION

Dedicated to my parents, wife and children.

ACKNOWLEDGEMENTS

First, I would like to thank my supervisor Prof. Dr. Narayan C. Kar so much for giving me an opportunity to pursue my PhD research under his supervision in the Center of Automotive Research and Green Energy Laboratory at the University of Windsor, one of the leading research facilities in the transportation electrification in Canada. I am grateful to my supervisor for his outstanding guidance and support that helped me to learn cutting-edge engineering knowledge and principles in my cross-discipline field of study. His continuous support and feedback helped me to stay focus in the proposed study and successfully conduct research and publish scientific results. He gave me an opportunity to work in an industrial collaborative research project where I was able to learn the needs and applications of my proposed study in real life. With his continuous supervision and input, I was able to apply my research knowledge and expertise in the laboratory to design and execute a promising and efficient solution for thermal modelling that potentially be used for electric vehicle market. On the other hand, as a mature student it was not so easy to manage health and family during my study. His advice and encouragement helped me mentally so much to overcome many difficult situations. I offer my sincere thanks and gratitude to my supervisor for everything during my study at the University of Windsor.

I was very fortunate being able to work with a talented group of people in the lab where everyone works hard and produce high standard innovations. I would like to thank my lab colleagues Dr. Eshaan Ghosh, Dr. Chunyan Li, Dr. Guodong Feng, Dr. Lakshmi Varaha Iyer, Dr. Anas Labak, Himavarsha Dhulipati, Shruthi Mukundan, Pratik Roy, and Ali Towhidi for their support that helped me to understand the problem and develop solutions through collaborative research work. I would like to thank my committee members for serving on my PhD committee and providing me a valuable feedback and input in my research work.

I am grateful to my parents, wife and children for their support that gave me strength to overcome many difficult situations during my study.

TABLE OF CONTENTS

DECLARATION OF CO-AUTHORSHIP /PREVIOUS PUBLICATIONS iii

ABSTRACT vi

DEDICATION vii

ACKNOWLEDGEMENTS viii

LIST OF TABLES xiii

LIST OF FIGURES xv

LIST OF ACRONYMS xviii

CHAPTER 1 1

INTRODUCTION 1

1.1. Overview and Motivations 1

1.2 Needs for Improved Thermal Design and Analysis of Traction Motors 3

1.3 Methodologies for Thermal Modelling of Traction Motor 7

1.3.1 Fundamentals of Heat Transfer 8

1.3.2 Convection Coefficient in the End-winding of Traction motor 9

1.4 Background Study for LPTN modelling for Thermal Characterization and Protection of Traction Motors in EV applications 10

1.5 Research Objectives 12

1.6 Research contribution for LPTN modelling for Thermal Characterization and Protection of Traction Motors in EV applications 14

1.7 Organization of the Dissertation Highlighting Research Contributions 15

1.8 References 17

CHAPTER 2 20

TRANSIENT THERMAL ANALYSIS OF A COPPER ROTOR INDUCTION MOTOR USING A LUMPED PARAMETER TEMPERATURE NETWORK MODEL 20

2.1 Introduction.....20

2.2 Investigation of transient thermal behavior.....21

2.2.1 Motor Loss Approximations.....21

2.2.2 Lumped Parameter (LPTN) Thermal Network Model.....23

2.3 Experimental Setup.....28

2.4 Results and Analysis.....28

2.5 Conclusion.....34

2.6 References.....34

CHAPTER 3.....36

ANALYSIS OF END-WINDING THERMAL EFFECTS IN A TOTALLY ENCLOSED FAN COOLED INDUCTION MOTOR WITH DIE CAST COPPER ROTOR.....36

3.1. Introduction.....36

3.2 Thermal Overload Protection Techniques and Thermal Model of Induction Motor.....38

3.3 Proposed Higher Order Thermal Model Solution.....41

3.3.1Motor Loss Approximations.....41

3.3.2 Higher Order Thermal Model.....42

3.3.3 Analytical Solution of Temperature rise in LPTN Model.....47

3.4 Experimental Investigation.....57

3.4.1 Experimental Setup.....57

3.4.2 Results and Analysis.....59

3.4.2.1 The proposed higher order LPTN model predicted temperature estimation and validated with experiments......59

3.4.2.2 Analysis of higher order thermal model results compared to 1st order thermal model in industry applications.....60

3.4.2.3 Heating time constant.....63

3.4.2.4 Analysis of cooling effects of stator end-winding on fan side and drive side.65

3.5 Conclusion.....66

3.6 References.....67

CHAPTER 4.....69

CFD AND LPTN HYBRID TECHNIQUE TO DETERMINE CONVECTION COEFFICIENT IN END-WINDING OF TEFC INDUCTION MOTOR WITH COPPER ROTOR.....69

4.1 Introduction.....69

4.2 Advances in copper rotor technology and End-winding cooling challenges.....72

4.3 Determination of Heat Transfer Coefficients.....73

4.3.1 Natural Convection Coefficients from End-winding.....73

4.3.2 Determination of Air Flow Characteristics in the Stator End-winding Region using Computational Fluid Dynamic (CFD) technique.....78

4.3.2 Validation of Air Flow Characteristics in the End-winding Region through Experiments.....83

4.3.4 Forced Convection Coefficients from End-winding.....83

4.4 Conclusion.....90

4.5 References.....91

CHAPTER 5.....93

LPTN MODELLING FOR THERMAL CHARACTERIZATION AND PROTECTION OF AN INTERIOR PERMANENT MAGNET SYNCHRONOUS MOTOR (IPMSM) FOR ELECTRIC VEHICLE APPLICATION.....93

5.1 Introduction.....93

5.2 Integrated Lumped Parameter Thermal Network Model (LPTN).....95

5.2.1 Loss Model Setup for the Integrated Thermal Model.....95

5.2.2 Proposed LPTN Model Setup for the Proposed IPMSM Motor.....97

5.2.3 Heat Transfer and Proposed Analytical Solution.....99
5.4 Experimental Setup 102
5.5 Results and Discussion.....105
5.5.1 Comparison of LPTN and Experimental Results - Air Cooling 105
5.5.2 LPTN Results – Liquid Cooling.....109
5.6 Conclusion.....111
5.7 References 112
CHAPTER 6 114
DISCUSSIONS AND CONCLUSIONS 114
6.1 Discussions and conclusions.....114
6.2 Future work.....115
APPENDICES 116
Appendix A: List of Publications.....116
A.1. Published peer-reviewed Journal and Conference papers during my tenure as a graduate student at the University of Windsor.....116
Appendix B: Industrial Collaborative Research.....118
B.1. Industrial research contributions during my tenure as a graduate student at the University of Windsor.....118
Appendix C: Permissions for Using Publication.....119
VITA AUCTORIS.....121

LIST OF TABLES

Table 1.1 3
Electric Propulsion used in Automotive Industry. 3
Table 1.2 3
Traction Propulsion System Evaluation [5] 3
Table 1.3 5
Performance at Continuous Operating Temperature Limit 5
Table 1.4 11
Temperature Limits for Different Insulation Classes 11
Table 2.1 22
Copper Rotor Induction Test Motor Data Sheet 22
Table 2.2 22
Motor Losses (Watts) for Different Loading at 1,500 rpm 22
Table 2.3 25
Thermal Network Model Temperature Nodes and Thermal Resistances 25
Thermal properties at room temperature considered for thermal resistance and capacitance calculation 26
Table 2.5 26
Key physical dimensions considered for thermal resistance calculation 26
Table 3.1 37
Temperature Limits for Different Insulation Classes 37
Table 3.2 41
Copper Rotor Induction Test Motor Data 41
Table 3.3 42
Copper Rotor Induction Motor Losses at 1,500 RPM 42
Table 3.4 46
Lumped Parameter Thermal Network Model Parameter 46
Table 3.5 47
Thermal Properties at Room Temperature Considered for Thermal Resistance and Capacitance Calculation 47
Table 3.6 47
Key Physical Dimension Data of the Test Motor 47
Table 3.7 59

Resistance Temperature Detectors (RTD) Used in the Experimental Setup 59
Table 3.8 63
Heating Time Constant for different loading Experiments..... 63
Table 4.1 74
Simplified Lumped Parameter Thermal Network (LPTN) Model Parameter 74
Table 4.2 77
Copper Rotor Induction Test Motor Data..... 77
Table 4.3 77
Key Physical Dimension Data of the Test Motor 77
Table 4.4 77
No Load Test Results for CRIM..... 77
Table 4. 5 78
No Load Test Results for CRIM..... 78
Table 4.6 87
Combined Natural and Forced Convection Heat Transfer Coefficients at different rotor rpm 87
Table 5.1 96
Technical Specifications and Physical Dimensions of IPMSM 97
Table 5.2 97
Loss Data from Electromagnetic Simulation of IPMSM..... 97
Table 5.3 98
Lumped Parameter Thermal Network Model Parameter..... 99
Table 5.4 100
Material Thermal Properties of IPMSM Motor 100
Table 5.5 110
Heat Removal by the Liquid Cooling in LPTN Model..... 110

LIST OF FIGURES

Figure. 1.1. Speed and Torque for combined UDDS and HWFET drive cycles [8]. 5

Figure. 1.2. Torque-speed characterstics IPMSM [8]. 6

Figure. 1.3. Winding and manget tmeprature linked to torque-speed characterstics for IMPSM [8]. 6

Figure. 1.4. End-winding region of a squirrel cage induction motor and air circulation in the region [17] 10

Figure 2.1. Copper Rotor Induction Motor (a) Stator (b) Rotor. 21

Figure 2.2. Proposed lumped parameter thermal network (LPTN) model for copper rotor induction motor. 23

Figure 2.3. Thermal experimental setup. (a) Test motor coupled with the dyno. (b) Torque/speed monitor and RTD sensors connected to DAQ unit. 29

Figure 2.4. Experimental end-winding temperature rise at drive side for 1,500 rpm and 30

loading 30 Nm, 50 Nm and 70 Nm with TEFC fan cooling. 30

Figure 2.5. Comparison between experimental and predicted end-winding temperature 31

rise at drive side for 1,500 rpm and 70Nm loading torque. 31

Figure 2.6. Comparison between experimental and predicted end-winding temperature rise at drive side for 1,500 rpm and 50 Nm loading torque. 31

Figure 2.7. Comparison between experimental and predicted end-winding temperature 32

rise at drive side for 1,500 rpm and 30 Nm loading torque. 32

Figure 2.8. End-winding temperature rise at drive side for 1,500 rpm and loading torque. 32

(a) 30 Nm. (b) 50 Nm. (c) 70 Nm with TEFC fan cooling. 32

Figure 2.9. Comparison of End-winding temperature rise at drive side for TEFC fan cooling 70 Nm loading torque, without fan cooling and NO Loading torque. 33

Figure 2.10. End-winding temperature rise without fan cooling and loading. (a) 70 Nm. (b) 0 Nm. agrees with the temperature rise recorded using infrared camera technique. .. 33

Figure. 3.1. Typical thermal limit curves per IEEE 620-1996 [10]. 40

Figure. 3.3. Induction motor construction for the proposed thermal model. 45

Figure. 3.4. A proposed higher order thermal network model. 45

Figure. 3.5. Induction motor. (a) Copper rotor. (b) Aluminum rotor. 53

Figure. 3.6. Air circulation in the end region between Stator end-windings/rotor end-rings and endcap in an aluminum rotor induction motor. 54

Figure. 3.7. Combined free and forced Convection in the end region between Stator end-windings/rotor end-rings and endcap in a copper rotor induction motor..... 54

Figure 3.8. Schematic diagram of the experimental setup. 57

Figure 3.9. Thermal experimental setup. (a) Torque-speed controller. (b) CRIM test motor. 58

Figure 3.10. Experimental results of stator end-winding temperature rise for different loading at 1,500 rpm speed. 59

Figure 3.11. Comparison of experimental and predicted results of stator end-winding temperature rise for different loading at 1,500 rpm speed. 60

Figure 3.12. Comparison of experimental and predicted results by 1st order model and higher order model for 70 Nm loading at 1,500 rpm speed. 61

Figure 3.13. Comparison of experimental and predicted results by 1st order model and higher order model for 50 Nm loading at 1,500 rpm speed. 62

Figure 3.14. Comparison of experimental and predicted results by 1st order model and higher order model for 30 Nm loading at 1,500 rpm speed. 62

Figure 3.15. Higher order model predicted results at different location for 30 Nm loading at 1,500 rpm speed. 63

Figure 3.16. Thermal heating constants for different loading of 30 Nm (38%), 50 Nm (63%) and 70 Nm (88%). 64

Figure 3.17. Thermal heating constants at different speed. 64

Figure 3.18. Stator end-winding temperature for different speed. 65

Figure. 3.19. Comparison of stator end-winding temperature rise for 70 Nm loading at 1,500 rpm speed with and without small fan. 66

Figure 4.1. TEFC induction motor. (a) Stator. (b) Copper rotor. (c) Aluminum rotor. 70

Figure. 4.2. Published correlations for the equivalent heat-exchange coefficients in the end-regions for TEFC induction motors [4]-[11]. 72

Figure. 4.3. A simplified Lumped Parameter model for end-winding..... 73

Figure 4.4. Measured temperatures for end-winding and inner air in the end-region. 76

Figure. 4.5. CRIM sectional view for the proposed study. 79

Figure 4.6. CFD models (a) with rotor fins (b) with rotor fins. 79

Figure 4.7. Air flow pattern at rotor speed 1,200 rpm. 80

Figure 4.8. Air flow pattern at rotor speed 600 rpm. 80

Figure 4.9. Air flow pattern at rotor speed 200 rpm. 81

Figure 4.10. Air flow pattern at rotor speed 1,200 rpm with a small fin. 81

Figure 4.11. Air flow pattern at rotor speed 600 rpm with a small fin. 82

Figure 4.12. Air flow pattern at rotor speed 200 RPM with a small fin 82

Figure 4.13. Experimental Set-up (a) DC thermal test (b) air velocity measurement test on a 20-hp IM with copper rotor. 84
Figure 4.14. Measured air velocity in the vertical axis to the end-winding plane. 85
Figure 4.15. Measured air velocity in the horizontal axis to the end-winding plane. 85
Figure 4.16. Combined convection coefficient varies with rotor speed rpm. 88
Figure 4.17. Combined convection coefficient with rotor peripheral speed (m/s). 88
Figure 4.18. Comparison of proposed correlation for convection coefficient with the published ones by other models 89
Figure 4.19. Convection coefficient in the end-winding of the motor that has no fins on its rotor end-rings. 90
Figure 5.1. Motor speed and torque for UDDS and HWFET [14]. 96
Figure 5.2. Parts of IPMSM. (a) rotor with shaft and bearings. (b) Assembled motor. ... 96
Figure 5.3. Proposed simplified Lumped Parameter Thermal Network Model for IPMSM (a) fan cooling (b) liquid cooling. 98
Figure 5.6. Convection coefficient in the end-winding in the motor. 102
Figure 5.4. Proposed simplified LPTN model with liquid cooling 103
Figure 5.5. Proposed simplified LPTN model with air cooling. 104
Figure 5.7. Thermal Test Setup for 4.3 kW IPMSM. 105
Figure 5.8. LPTN predicted temperature for motor parts. 106
Figure 5.9. Winding temperature for different loading conditions. 106
Figure 5.10. Winding temperature for 70 Nm loading torque. 107
Figure 5.11. Winding temperature for 58 Nm loading torque. 107
Figure 5.12. Winding temperature for 40 Nm loading torque. 108
Figure 5.13. Winding temperature with/without fan cooling. 109
Figure 5.14. Winding temperature for different heat removal. 110
Figure 5.15. Motor parts temperature for 60% heat removal. 110

LIST OF ACRONYMS

CFD	Computational Fluid Dynamics
CHARGE	Center for Hybrid Automotive Research and Green Energy
CRIM	Copper Rotor Induction Motor
DAQ	Data Acquisition
DC	Direct Current
EV	Electric Vehicle
EPRI	Electric Power Research Institute
FEA	Finite Element Analysis
GHG	Greenhouse Gas
HWFET	Highway Fuel Economy Driving Schedule
HEV	Hybrid Electric Vehicle
IM	Induction Motor
IEEE	Institute of Electrical and Electronics Engineers
IPMSM	Interior Permanent Magnet Synchronous Motor
UDDS	Urban Dynamometer Driving Schedule
LPTN	Lumped Parameter Thermal Network
NEMA	National Electrical Manufacturers Association
RTD	Resistance Temperature Detector
PM	Permanent Magnet
PMSM	Permanent Magnet Synchronous Motor
TEFC	Totally Enclosed Fan-cooled

CHAPTER 1

INTRODUCTION

1.1. Overview and Motivations

Climate change not only causes a serious detrimental impact to the natural environment but also, poses one of the largest threats to the socio-economic and political systems worldwide. According to 2011 National Round Table study on the Environment and Economy, climate change could cost Canada $21-43 billion per year by 2050 [1]. There are serious growing concerns demonstrated and identified by the international community over climate change and hence, a Paris climate agreement was reached and ratified near unanimously to limit global warming to well below 2^0C above pre-industrial levels. It is an obvious and clear choice to adopt a low carbon economy to reduce greenhouse gas (GHG) emissions significantly in order to meet the Paris agreement. Canada has set a target of 30% GHG reduction below 2005 levels by 2030 and 80% reduction below 2005 levels by 2050. Transportation sector in Canada has the second largest source of GHG emissions which is 24% of the total and of which, 12% is generated from the light duty vehicles [1]. As a result, the Government of Canada and the provinces has clearly understood and recognized that EVs can contribute significantly to reduce GHG emissions as well as develop a zero-carbon economy. Canadian interest in electric vehicles (EV) is currently all-time high and EV sales have grown significantly over last seven years. In 2011, EV sales were 125 thousands which has increased to over 2 million in the year of 2017 [2]. This is a significant and impressive growth and many policies and incentive programs offered by the Government of Canada and the provinces. Lower vehicle prices, increased driving range and fast battery charging infrastructure are encouraging more people to buy electric vehicles. Through the Electric Vehicle and Alternative Fuel Infrastructure initiative, the Government of Canada is investing $96.4 million to build coast to coast charging network for electric vehicles and gas stations for hydrogen fuel cell electric vehicles and $10 million for the development of US-CANADA codes and standards for low emission electric vehicles [1]. All levels of governments and stakeholders have made a significant progress towards this development of Alternative Fuel Infrastructure. In the United States, Clean Air Act is a federal law to control air pollution from stationary and

mobile sources. The zero-emission vehicle program offered by California Air Resources Board is designed to reduce emissions from mobile sources that shows the roadmap towards building a healthy and sustainable community [3]. Considering climate agreement and environmental policies, automotive manufacturers are making more and more zero emission vehicles and it is predicted that 50% of the total vehicle sales will be EV globally by 2050 [4].

Electric Machines are at the center focus to replace internal combustion engines and generate equal mechanical power at relatively higher efficiency. This has created a huge demand of electric machines that are to be used to provide propulsive force for vehicles. Every EV has one electric motor and could be multiple depending on the vehicle architecture. Over the last decade, EV designs have changed, however, rapid advancement of the drive and power electronic technology created ample opportunities for the improvement of EV motor designs. Automotive manufacturers are in remarkable competition to produce the best EV product which is ever efficient and cost-effective. Hence, selecting a traction motor is a challenging task for the designers. In the 20^{th} century, direct current (DC) motors were widely used for traction motor applications. However, in the recent years, EVs primarily use induction machines (IMs) and permanent magnet (PMs) machines and on the other hand, switching reluctance motors are gaining much interest. Table 1.1 lists the examples of traction motors that are currently being used in hybrid electric or full electric vehicles [4]-[5].

A comparative study among these four traction motors based on the factors including power density, efficiency, controllability, reliability, technical maturity and cost has been completed [5]. Table 1.2 describes the factors assigned to each of the motor candidate towards their suitability for traction motor applications. From this comparative study, IMs demonstrates the best suitability over PMs. IMs have the advantages over PMs for controllability, reliability, technical maturity and cost. On the other hand, PMs have the advantages over IMs for power density and efficiency. It is clear that more research and development can enhance the suitability between these IMs and PMs for EV applications. This thesis, in particular, investigates thermal design of the EV motors and how thermal parameters affects the performance characteristics of the motor as well as active cooling

requirements in order to keep the motor temperatures within the safe operating limit for various duty cycles of the vehicles.

TABLE 1.1

ELECTRIC PROPULSION USED IN AUTOMOTIVE INDUSTRY.

Model	Type of Electric Motor
Daimler-Chrysler	Induction Motor
Ford Focus Electric	Permanent Magnet Synchronous Motor
Mitsubishi i-MiEV	Permanent Magnet Synchronous Motor
Chevrolet Spark EV	Permanent Magnet Synchronous Motor
Nissan Leaf	Permanent Magnet Synchronous Motor
Chevrolet Volt	Permanent Magnet Synchronous Motor
BMW X5	Induction Motor
Tesla Model S	Induction Motor
BMW X5 xDrive40e	Induction motor
Tesla Model X	Induction motor
PSA Peugoet	DC motor
Toyota Prius	Permanent Magnet Synchronous Motor
Holden/ECommodore	Switched Reluctance Motor
Honda/Insight	Permanent Magnet Synchronous Motor

TABLE 1.2

TRACTION PROPULSION SYSTEM EVALUATION [5]

	Traction Motor Types			
Characteristics	Direct Current Motor	Induction Motor	Permanent Magnet Motor	Switched Reluctance Motor
Power density	2.5	3.5	5	3.5
Efficiency	2.5	3.5	5	3.5
Controllability	5	5	4	3
Reliability	3	5	4	5
Technical maturity	5	5	4	4
Cost	4	5	3	4
Total	22	27	25	23

1.2 Needs for Improved Thermal Design and Analysis of Traction Motors

The following section includes traction motor overview and performance characteristics, EV drive cycles, link between performance parameters and temperature as well as active cooling needs. The requirements for traction motor characteristics include high power

density; high torque at low speed for starting and climbing; high power at high speed for cruising; wide speed range; a fast torque response; high efficiency over wide torque and speed ranges; high reliability and reasonable cost. Hence, traction motors are generally designed to produce peak torque and peak power which are much greater than rated torque and power. However, for frequent urban and suburban driving, it requires low speed, low torque and power which could cause waste of energy. That is why, it is imperative to investigate the effects of driving conditions on these motor performance characteristics to find the correct size of the motor with high power density and efficiency. On the other hand, thermal analysis of electric machines has always received less attention compared to electromagnetic design of the machines in the past [6]. The motor designers used to thrive to improve the electromagnetic design of the motor whereas thermal aspects were dealt superficially. However, as the industry demands high torque and power density from the electric motor specifically, for electric vehicle applications, thermal analysis has gotten more and more attention from the researchers in order to provide improved motor efficiency and power density. High torque density requirement means increasing current and consequently, higher temperature rise in the motor. From thermal point of view, Table 1.3 compares total losses in the copper rotor induction motor and permanent magnet motor that actually contribute to heating for their performance at continuous operating limit. CRIM has greater losses than PM for 118 Nm of torque at 900 rpm rating [7]. Hence, CRIM requires higher active cooling compared to IPMSM in order to maintain similar torque and speed conditions. In [8], interior permanent magnet synchronous motor (IPMSM) was tested for its performance in terms of torque and thermal condition under standard driving cycles of Urban Dynamometer Driving Schedule (UDDS) and Highway Fuel Economy Driving Schedule. Winding and magnet temperatures were calculated for both driving cycles for various loading conditions. Figure. 1.1 shows the speed and torque requirements under combined UDDS and HWFET drive cycles where maximum torque is 60 Nm and rated torque is 29.5 Nm. Figure 1.2 shows torque-speed characteristics curves for IPMSM where peak torque is 57 Nm and the rated torque is around 29.5 Nm under UDDS and HWFET driving cycles. It can be seen that there are some points beyond rated torque at high speed conditions. In order to link thermal performance with electromagnetic performance, winding and magnet temperatures are investigated as shown in Figure 1.3.

TABLE 1.3

PERFORMANCE AT CONTINUOUS OPERATING TEMPERATURE LIMIT

Parameters	IPMSM	CR-IM
Stack length (mm)	84	105
Speed (rpm)	900	900
Torque (Nm)	118	118
Efficiency (%)	92.5	88.2
Losses (W)	897	1485
Coolant (^{o}C)	105	105
Winding (^{o}C)	156	156

Design temperature limits for winding and magnet are 140^{o}C and 130^{o}C respectively without any active cooling. IPMSM was able to meet the requirements of prodcuing rated torque of 30 Nm under the design temperature limit for urban driving conditions. However, IPMSM still does not satisfy completely for HWFET driving conditions as shown in the Figure 1.2. This confirms the requirements of active cooling for IPMSM in order to fully satisfy both UDDS and HWFET driving cycles. Moreover, it is never recommended to design the traction motor that reaches design temperature limit at rated condition as shown in Figure 1.3.

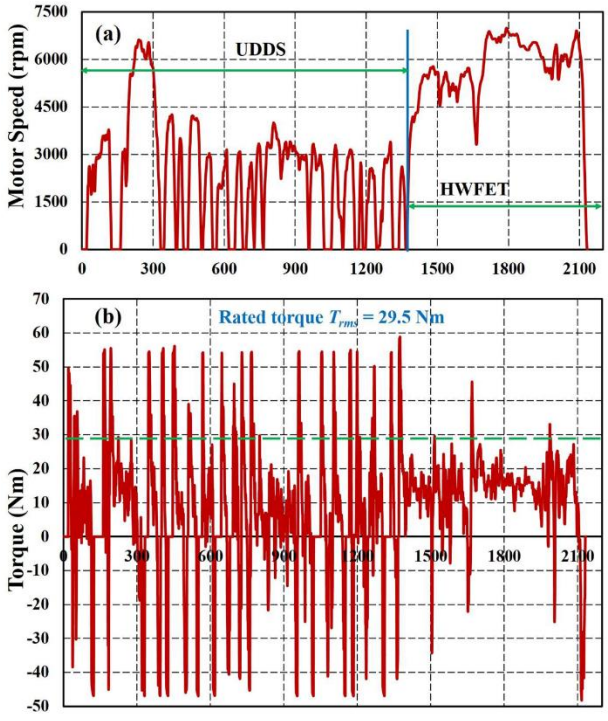

Figure. 1.1. Speed and Torque for combined UDDS and HWFET drive cycles [8].

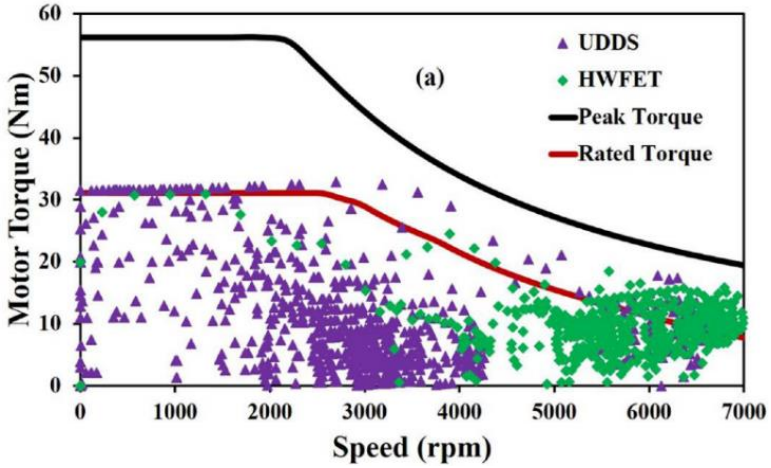

Figure. 1.2. Torque-speed characterstics IPMSM [8].

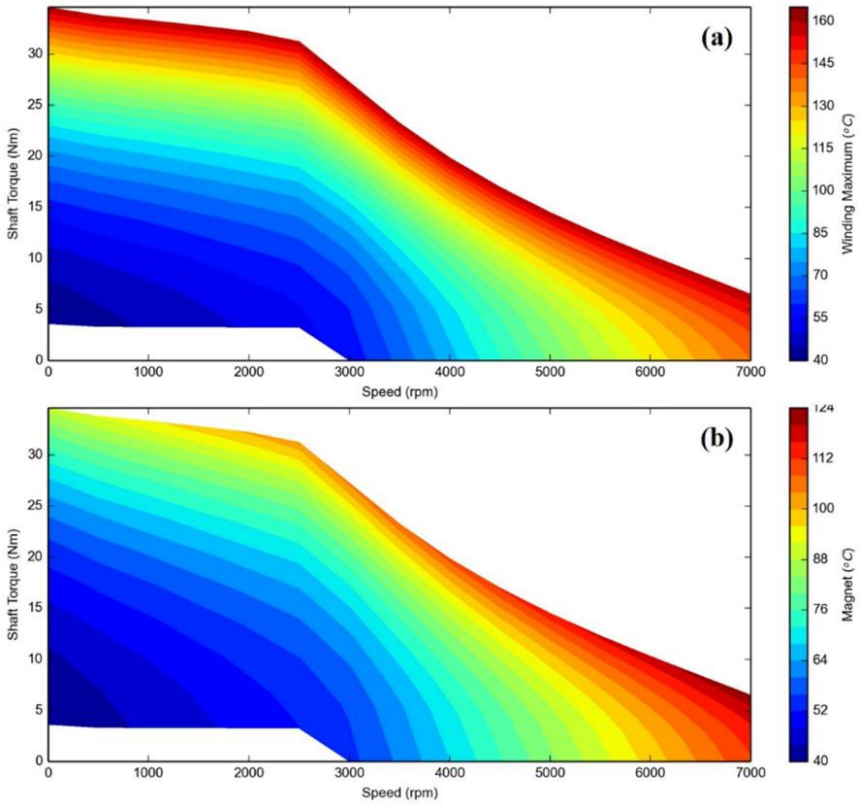

Figure. 1.3. Winding and manget tmeprature linked to torque-speed characterstics for IMPSM [8].

The operating temperature limit should be well below the design temperature which is only possible with active cooling in the motor. Tractions motors are expected to produce high torque while starting and climbing, hence an adequate cooling can help to keep the operating tempeture with in the safe limit. If the temperature of the winding and permanent

magnet exceed permissible thermal limit frequently due to lack of proper understanding and managing of the thermal conditions of the motor, it will not only reduce the motor performance as well as it will have the detrimental effects on the life of insulation material and consequently, it will cause permanent insulation breakdown. On the other hand, demagnetization due to higher temperature will cause a permanent damage to the motor. So the correct evaluation of performance of traction motors will be determined by the driving conditions as well as how thermal design can fully staify these driving conditions efficiently.

1.3 Methodologies for Thermal Modelling of Traction Motor

Two different thermal modelling techniques that are used today to determine motor temperature are analytical Lumped Parameter Thermal Network (LPTN) and numerical modelling. Lumped Parameter Thermal Network (LPTN) is widely and commonly used by the researchers and motor designers to calculate temperature as it is much faster and involves only use of heat transfer empirical relationships. The numerical methods are very effective when complex modelling of heat and air flow conditions exist. However, numerical technique is less attractive over Lumped Parameter Thermal Network (LPTN) due to its longer computational time and related costs. The most efficient procedure to analyze the heat transfer exchange in an electric motor is based on lumped parameters, as indicated in many technical literatures of this subject [9]-[14]. Lumped heat capacity system refers to a system that may be considered uniform in temperature. In lumped-heat-capacity analysis, it considers that the internal resistance of the body is negligible in comparison with the external resistance [15]. As the motor is built from different materials, heat transfer will be different through different motor components. Each motor component is considered as lumped heat capacity element which is considered to be uniform in temperature. A lumped parameter model consists of thermal resistances and capacitances to build a thermal network where heat transfer takes place through several paths in the motor. Each motor component is considered as a temperature node. In steady-state analysis, the net energy transfer into the node is zero, while for the unsteady-state analysis, the net energy transfer into the node must be evidenced as an increase in internal energy of the element. Each node behaves like a small lumped heat capacity and the interaction of all the nodes determines the thermal behavior of the motor in a transient process. In order to

determine the temperature rise at the various components or at each node, it requires only dimensional information and thermal parameters. It is much easier and faster to compute the temperature rise using heat transfer principles and formulas. The motor is considered as a cylindrical structure and symmetrical around the shaft axis. Hence, the model shows the heat transfer in radial direction from the center of the shaft axis towards the frame. As it is considered as cylindrical structure, heat transfer through each of the cylinder is assumed to be uniform in radial direction and the only heat transfer takes place in axial direction through the shaft, then to the endcaps.

1.3.1 Fundamentals of Heat Transfer

The heat from the motor is removed by conduction, convection and radiation heat transfer. Forced convection heat transfer is comparatively effective method of heat transfer. The cooling channel has to be designed with careful considerations so that required amount of coolant can flow through the motor. The following equations describe the basic heat transfer that takes place in an electrical machine [17].

i) Thermal resistance of any specific material is defined by the temperature change per unit heat flow through the material.

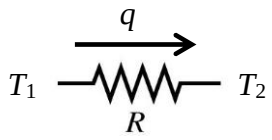

$$q = \Delta T / R \tag{1.1}$$

where, q is the heat flow, ΔT is the temperature difference, and R is the thermal resistance of the specific material.

ii) Fourier's law states the heat transfer by conduction and can be described as follows:

$$q = -k \times A \times \Delta T / \Delta x \tag{1.2}$$

where, q is the heat flow, ΔT is the temperature difference, k is the thermal conductivity of the material and Δx is the thickness of the material.

iii) The heat flow due to radiation heat transfer is defined by the Stefan-Boltzman equation which is given below:

$$q = \varepsilon \times \sigma \times \left(T_1^4 - T_2^4\right) \tag{1.3}$$

where, q is the heat flow, T_1 is the thermodynamic temperature of radiating surface and T_2 is the thermodynamic temperature of absorbing surface, ε is the relative emissivity between the emitting and absorbing surfaces and σ is the Stefan-Boltzmann constant 5.67 x 10^{-8} W/m^2K^4.

iv) To express the overall effect of convection, Newton's Law of Cooling is used:

$$q = h \times A \times \left(T_w - T_F\right) \tag{1.4}$$

where q is the heat flow, h is the convection heat transfer coefficient, A is convective surface area, T_f is temperature of the fluid, T_w is the temperature of the wall surface.

v) The heat capacity is analogous to the electrical capacitance and the electric charge stored in a capacitator is q which can be expressed as:

$$q = CU \tag{1.5}$$

where C is the capacitance of the capacitor and U the voltage over the capacitor.

vi) The quantity of heat stored in a body can be expressed as:

(1.6)

where m is the mass of the body, C_p is the specific heat capacity and ΔT is the temerature rise caused by heat flow.

vii) Now comparing both equations the heat capacity,

$$C_{th} = m \times C_p \tag{1.7}$$

which is analogous to the electrical capacitance.

1.3.2 Convection Coefficient in the End-winding of Traction motor

Convection coefficient in the end-winding region is one of the improtant thermal parameters in lumped parameter thermal network model. Complex nature of heat and air flow in the end-winding region makes the task quite challenging to determine end-winding convection coefficient. Such air circulation characteristics in the end-winding region vary

due to several factors such as shape and length of stator end-winding, rotor geometry and end space clearance. The end-windng region can be divided into two parts; the space between the end-winding and frame and the space between the rotor and the end-winding. Rotor speed primarily influences the air circulation in the space between the end-winding and the rotor as shown in Figure 1.4. [17]

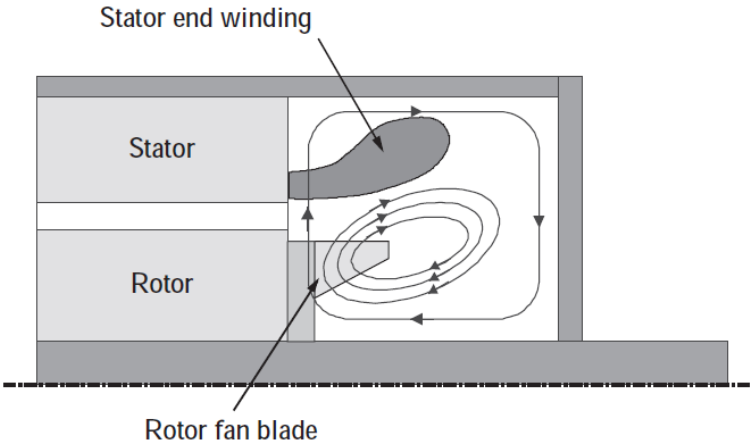

Figure. 1.4. End-winding region of a squirrel cage induction motor and air circulation in the region [17]

1.4 Background Study for LPTN modelling for Thermal Characterization and Protection of Traction Motors in EV applications

In the section 1.2, it has been identified that temperature rise caused by the motor losses has direct effects on motor performance in terms of torque, efficiency and power density. So, a careful thermal design of the traction motor is critical in order to produce rated torque and power without exceeding design temperature limit of the motor materials including winding and magnet for standard driving conditions. However, as there is always a demand to build a traction motor with smaller size and volume that can produce high torque and power density, excessive temperature rise becomes a critical factor to limit the rated capacity of the motor. Even with liquid cooling design of the motor there are also limited options to increase the size of the heat exchanger or cooling channel to remove the maximum amount of heat. So, the motor designers will have to consider all these design variables in the design phase. On the other hand, once the motor is built and ready to be used in the vehicle, motor performance including temperature rise and liquid coolant flow

rate must be monitored to keep the operating and loading conditions within the safe limit. These operating conditions require accurate thermal characterization of the motor that generates sufficient thermal information to protect the motor from overheating. Now we need a tool which is efficient and fast enough to determine such thermal characterization efficiently and accurately and regulate required coolant flow through motor cooling channels to remove maximum possible heat. Approximately 35-40% motor failure are related to stator winding insulation and iron core [18]-[20]. Typically, the highest temperature is reached in the stator winding compared to any other motor component once motor thermal limit is exceeded and hence, the insulation breakdown is the common cause of motor failure [21]. "A rule of thumb accepted throughout industry says that there is a 50% reduction in insulation life for each 10^{o}C increase in the temperature [22]. Since the stator insulation degradation is the main cause to motor failure, the National Electrical Manufacturer's Association (NEMA) established the permissible limit of the insulation class as presented in Table 1.4 [23], [24]. Considering the alarming statistics of motor failure, it is critical to monitor the stator winding temperature continuously and accurately to ensure that the permissible thermal limit is not exceeded and prevents a major breakdown or failure of the winding insulation. Many different techniques are used in the modern industries to protect thermal overload conditions. One of the techniques is embedding temperature measuring devices such as RTDs or thermocouples at the stator winding locations and measuring temperatures directly.

TABLE 1.4

TEMPERATURE LIMITS FOR DIFFERENT INSULATION CLASSES

Insulation Class	Ambient Temperature (^{o}C)	Rated Temperature Rise (^{o}C)	Hot Spot Allowance (^{o}C)	Insulation Temperature (^{o}C)
A	40	60	5	105
B	40	80	10	130
F	40	105	10	155
H	40	125	15	180

However, these techniques do not provide enough protection due to the non-uniform heating of the motor components including windings. In addition, these techniques are complex in installation and not cost-effective at all for small to medium scale machines

[22]. Due to higher cost and complexity of installation of these embedded sensors, the conventional approach in the industries is to use thermal overload protection devices to monitor the stator winding temperature [22]. Thermal overload protection devices are operated based on thermal model and in this approach a simplified first order thermal model is developed using nameplate information of the motor. Hence, this method is too simple and heat dynamics in the motor is completely ignored to predict stator winding temperature accurately. As a result, it is critically important to develop a higher order thermal model that explains heat dynamics of the motor efficiently and estimates the temperature accurately. This thesis proposes a higher order LPTN model-based technique for thermal characterization as well as thermal model-based protection of the traction motor. In the development of the higher order LPTN thermal model, this research also identified that determinetaion of convection cofficient in the motor end-winding is a challenging task. In [9]-[14], several researchers have determiend convection coefficient for aluminum rotor induction motor that has a rotor with fins on its rotor end-rings. However, higher efficinecy and thermal tolerance CRIM is an obvious choice for traction motor applications [25], [26]. But CRIM has a rotor that does not have any fins on its rotor endrings due to limitations in its fabrication process. This was still an open problem for the industry to determine convection coefficient for copper rotor induction motor. Moreover, permamnent magnet induction motor has also smooth rotor end like CRIM. Hence, this research work funther investigated both CRIM and IPMSM motor types and proposed thermal model techniques to determine the convection coefficient to be used in the proposed higher LPTN thermal model solution.

1.5 Research Objectives

So, a computationally efficient LPTN modelling is very important for traction motors in EVs to monitor motor performance and thermal status online and send these related status information to the control system that can implement required active cooling to the motor to prevent it from overheating and at the same time this can provide required torque, speed and power to satisfy driving conditions. This overall objective is divided into the following sub-objectives:

1) Understand the performance characteristics of traction motors in terms of torque, efficiency and power density and understand the link between motor performance and thermal design parameters.

2) Understand the needs for LPTN model-based thermal protection technique and comparison with existing simplified thermal model-based technique being used in the industry.

3) Develop a higher order lumped parameter thermal network model based on the needs stated in sub-objectives (1) & (2) to perform transient thermal analysis of electric motors and determine active cooling requirements.

4) Validate a higher order LPTN model through experimentation on a 20-hp copper rotor induction motor CRIM and also, compare 1st order LPTN model temperature results with higher order LPTN model temperature results for CRIM motor.

5) Develop a hybrid technique using LPTN model and computational fluid dynamic CFD model to determine convection coefficient in the end-winding region of the traction motors.

6) Validate an LPTN and CFD hybrid technique through experimentation on a 20 hp CRIM and determine end-winding convection coefficients.

7) Propose and develop a simplified LPTN model and created motor loss model that is used as an input to motor LPTN thermal model dynamically.

8) Both motor loss model and LPTN thermal model in sub-objective (7) are created in MATLAB Simulink that can increase the computational efficiency and can easily be integrated into the motor drive model in EVs to monitor and control motor performance including thermal health.

9) Validate the proposed models in sub-objectives (7) through experimentation on an interior permanent magnet motor (IPMSM) prototyped in CHARGE lab at the University of Windsor.

1.6 Research contribution for LPTN modelling for Thermal Characterization and Protection of Traction Motors in EV applications

First, this research develops a comprehensive LPTN thermal model to conduct thermal analysis of CRIM which is one of the most commonly and commercially used motors used in electric vehicle today. LPTN modelling technique is not a new concept but it is the most efficient and faster technique for thermal analysis of electric motors over FEA modelling technique. So in this research, through the development of LPTN modelling, the author creates a foundational work to predict motor temperature accurately.

Next, this research identifies that rotor geometry in CRIM is different than that in aluminum rotor induction motor. CRIM has smooth rotor ends and do not consist of any fins or blades on its end-rings like aluminum rotor. Hence in LPTN model solution for CRIM, there is no heat transfer formulation proposed or developed by the past researchers to calculate convection coefficient in the end-winding region. But past researchers proposed and developed heat transfer formulation to predict convection coefficient in the end-winding region in aluminum rotor induction motor. So this research proposes and develops a model to calculate convection coefficient in the end-winding of CRIM. Another motor is PMSM commonly used in electric vehicle application and these motors also do not have any fins or blades on their rotor end-rings. Hence, proposed heat transfer formulation developed for CRIM in this work to calculate convection coefficient is also used for PMSM.

This research work further investigates existing technologies for motor thermal protection and finds that none of the existing motor thermal protection devices can predict motor temperature accurately due to their technological limitations and complex installations. Most commonly used motor protection is thermal-model based, however, a 1^{st} order thermal model is used in the technique today and do not provide accurate prediction of the motor temperature. Hence, this research work proposes a higher order LPTN thermal model solution that can predict motor temperature accurately and protect the motor from overheating.

Finally, this research investigates the need for accurate thermal characterization of tractions motors in EV so that the motors can produce required torque and power and keep the

temperature within the safe limit. Currently, there is no such tool in the traction motors that can monitor motor performance and accordingly predict temperature and regulate cooling to bring down the temperature dynamically for various driving conditions. Currently, traction motors use conventional direct temperature measurement techniques to predict stator winding temperature. There is no such mechanism to predict magnet temperature which is very critical to prevent demagnetization due to temperature rise. Ambient temperature has direct impact on the cooling efficiency of the motor heat exchanger as the radiator is the primary component to expel heat to the ambient. Moreover, the needs for power electronics and battery cooling create additional challenges to overall thermal management system in EV. Considering these complexities, it is imperative to monitor motor performance online and adjust cooling requirements accordingly. This research proposes and validates a simplified higher order LPTN model for PMSM that predicts temperature of various motor parts including stator winding and magnet as well as regulate liquid cooling to the motor that helps to maintain the required torque and power generation. Motor thermal model algorithm can easily be integrated into motor drive model in order to monitor and predict thermal health of the motor. The integration of LPTN model into drive model is not covered in this research and in future, CHARGE lab at the University of Windsor is planning to execute this task in order to develop integrated thermal solution package for EV market.

1.7 Organization of the Dissertation Highlighting Research Contributions

The major objectives of this research are to propose a simplified lumped parameter thermal network modelling for thermal characterization and thermal overload protection of commonly used traction motors such as CRIM and PMSM. The proposed LPTN model will be computationally efficient and adaptable to predict thermal parameters under dynamic vehicle operating conditions to maintain the motor performance within the safe operating thermal limit. This dissertation contains 5 (five) chapters excluding introductory chapter that includes all research contribution and novelty conducted in this research in order to meet overall objectives.

Chapter 2 presents a lumped parameter thermal network model for copper rotor induction motor (CRIM). LPTN model considers thermal capacitances to calculate motor

temperatures in transient perspective. LPTN model solution includes motor loss calculations for CRIM and accordingly calculates temperatures to justify cooling design requirements for EV application.

Chapter 3 describes existing motor thermal protection mechanism and the needs for higher order LPTN thermal model that can determine motor temperatures more accurately. This chapter also compares the temperature results for 1st order LPTN model and higher order LPTN model in order to justify the requirements of higher order LPTN model proposed for EV application. This chapter also covers the investigations of end-winding convection coefficient for copper rotor induction motor that has a rotor with no fins on its rotor end-rings. In the experiments, a prototype fan was fabricated and used in the CRIM to mimic aluminum rotor fins to justify the cooling differences in the end-winding region.

Chapter 4 expands the investigation from chapter 3 and presents a hybrid LPTN and CFD solution technique to determine the end-winding convection coefficient for CRIM. First, an LPTN model for end-winding was developed and then through DC tests thermal resistances were calculated in order to determine natural convection coefficient while the rotor is still. Second, analytical solution based on Nusselt number equation was used to determine forced convection coefficient. In forced convection coefficient calculation, air velocity was required. CFD and experimental solution determined air circulation in the end-winding region of copper rotor induction motor.

Chapter 5 finally proposes a simplified higher order LPTN model to determine thermal characterization of an interior permanent magnet motor. LPTN model was tested for both air cooling and liquid cooling designs and justified the cooling requirements for the prototype motor. The proposed model took online electrical parameters determined by the loading torque and power for the drive cycles to generate motor loss model. Motor loss model fed into thermal LPTN model where only selected thermal parameters and motor physical dimensions were used to determine temperature of various motor parts including winding and magnet. This LPTN predicted motor temperature by varying the amount of heat removal from the motor in order to maintain the torque and power.

1.8 References

[1] Accelerating the Deployment of Zero Emission Vehicles: Atlantic Canada and the Prairies [Online]. Available: https://www.nrcan.gc.ca/energy/transportation/alternative-fuels/resources/21312?wbdisable=true

[2] Market Snapshot: Lower costs, better technology, and provincial policies are helping grow Canada's small fleet of electric vehicles [Online]. Available: https://www.cer-rec.gc.ca/nrg/ntgrtd/mrkt/snpsht/2016/08-02lctrcvhcl2016-eng.html

[3] Zero Emission Vehicle Program [Online]. Available: https://ww2.arb.ca.gov/our-work/programs/zero-emission-vehicle-program

[4] N. C. Kar, K. L. V. Iyer, A. Labak, X. Lu, C. Lai, A. Balamurali, B. Esteban and M. Sid-Ahmed, "Courting and Sparking: Wooing Consumers' Interest in the EV Market," *IEEE Electrification Magazine,* vol. 1, no. 1, pp. 21-31, 2013.

[5] M. Zeraoulia, M. E. H. and D. Diallo, "Electric Motor Drive Selection Issues for HEV Propulsion Systems: A Comparative Study," IEEE Transactions on Vehicular Technology, vol. 55, no. 6, pp. 1756-1764, 2006.

[6] F. Ahmed and N. C. Kar, "Analysis of End-winding Thermal Effects in a Totally Enclosed Fan Cooled Induction Motor with Die Cast Copper Rotor," IEEE Transactions on Industry Applications, vol. 53, no. 3, pp. 3098 – 3109, 2017.

[7] L. D. Marlino, Report on Toyota Prius Motor Thermal Management, Oak Ridge National Laboratory, 2005.

[8] T. A. Huynh and M. Hsieh, Performance Analysis of Permanent Magnet Motors for Electric Vehicles (EV) Traction Considering Driving Cycles, Energies 2018, 11, 1385; doi:10.3390/en11061385.

[9] A. Boglietti and A. Cavagnino, "Analysis of the end-winding cooling effects in TEFC induction motors," IEEE Transactions on Industry Applications, volume 43,issue 5, pp. 1214-1222, 2007.

[10] C. Micallef, S. J. Pickering, K. Simmons, and K. Bradley, "Improvements in air flow in the end region of a large totally enclosed fan cooled induction motor," Proc. of IEMDC'05 IEEE International Electric Machines and Drives Conference, San Antonio, May 2005.

[11] A. Boglietti, A. Cavagnino, D. Staton, M. Popescu, C. Cossar, and M.I. McGilp, "End space heat transfer coefficient determination for different induction motor enclosure types", IEEE Trans. on Industry Applications, vol. 45, No. 3, May/June 2009, pp. 929-937

[12] E. Schubert, "Heat Transfer Coefficients at End Windings and Bearing Covers of Enclosed Asynchronous Machines," Elektrie, vol. 22, April 1968. pp160-162. (Translation ERA/IB 2846).

[13] A. Boglietti, A. Cavagnino, D. Staton, and M. Popescu, "Impact of different end region cooling arrangements on endwinding heat transfer coefficients in electric motors," Proc. IEEE Conf. on Industrial Electronics, 978-1-4244-4649-0/09.

[14] C. Micallef, S. J. Pickering, K. A. Simmons, and K. J. Bradley, "An Alternative Cooling Arrangement for the End Region of a Totally Enclosed Fan Cooled (TEFC) Induction Motor," 4th IET Conference on Power Electronics Machines and Drives, pp. 309-309, (2008).

[15] J.P., Holman.''Heat Transfer" 9th ed., McGraw-Hill, 2002, pp. 640-647.

[16] G. Demetriades, H. Zelaya de la Parra, E. Andersson, and H. Olsson, "A Real-Time Thermal Model of a Permanent-Magnet Synchronous Motor."39th Annual Power Electronics Specialists Conference, Rhodes, Greece, June 15–19, 2008.

[17] J. Pyrhonen, T. Jokinen and V. Hrabovcova, "Design of Rotating Electric Machines", 2008 John Wiley & Sons, Ltd. ISBN: 978-0-470-69516-6.

[18] Motor Reliability Working Group, "Report Of Large Motor Reliability Survey Of Industrial And Commercial Installations, Part I". IEEE Trans. Ind. Appl., vol. IA-21, no. 4, pp. 853-864, July/Aug. 1985.

[19] P. O'Donnell, "Report of large motor reliability survey of industrial and commercial installations: Part I," IEEE Trans. Ind. Appl., vol. IA-21, no. 4, pp. 853–864, Jul. 1985.

[20] P. O'Donnell, "Report of large motor reliability survey of industrial and commercial installations: Part II," IEEE Trans. Ind. Appl., vol. IA-21, no. 4, pp. 865–872, Jul. 1985.

[21] P. F. Albrecht, J. C. Appiarius, and D. K. Sharma, "Assessment of reliability of motors in utility applications—Updated," IEEE Trans. Energy Convers., vol. EC-1, no. 1, pp. 39–46, Mar. 1986.

[22] R. M. Tallam, S. B. Lee, G. C. Stone, G. B. Kilman, J. Yoo and T.G. Habetler "A Survey of Methods for Detection of Stator-Related Faults in Induction Machines" IEEE Transactions on Industry Applications, volume 43, no 4, July/August 2007.

[23] P. Zhang, Y. Du and T. G. Habetler, "A Transfer-Function-Based Thermal Model Reduction Study for Induction Machine Thermal Overload Protective Relays" IEEE Transactions on Industry Applications, volume 46, No. 5, 2010.

[24] Information Guide for General Purpose Industrial AC Small and Medium Squirrel-Cage Induction Motor Standards, NEMA Standard MG1-2003, August 2003.

[25] D.T. Peters, J.G. Cowie, E.F. Brush, Jr. and D.J. Van Son, "Copper in the Squirrel Cage for Improved Motor Performance," International Electric Machines and Drives Conference, June, 2003.

[26] E.F. Brush, J.G. Cowie, D.T Peters and D.J. Van Son, "Die-Cast Copper Motor Rotors; Motor Test Results, Copper Compared to Aluminum", Energy Efficiency in Motor Driven Systems, Eds: F. Parasiliti & P. Bertoldi, Published by Springer, 2003, p 136 to 143.

CHAPTER 2

TRANSIENT THERMAL ANALYSIS OF A COPPER ROTOR INDUCTION MOTOR USING A LUMPED PARAMETER TEMPERATURE NETWORK MODEL

2.1 Introduction

Considering the environmental concerns electric propulsion is becoming increasingly the priority for the automotive industry. For the electric vehicle, internal permanent magnet motor is a very common choice by the automotive manufacturers over many years. The biggest disadvantage is that the industry has to depend on rare earth magnet materials which are not sustainable option in terms of manufacturing and supply chain. There has to be an alternative material to be used for electric propulsion. Recent development of the induction motor with die cast copper rotor that has comparable high torque and higher efficiency under normal vehicle operating conditions has attracted automotive industry to a great extent. In [1]-[3], it has identified several advantages over permanent magnet motor such as 20% less costly to manufacture with similar size (weight, volume), rugged and durable design, maintaining the efficiency at higher speed and low torque conditions. On the other hand, the copper die-cast rotor motor has several advantages over aluminum rotor machine such as greater efficiency due to higher electrical conductivity, 23% lighter and 30% smaller than the aluminum rotor machine. All these key performance and economic advantages, copper rotor induction motor has become a great alternative choice for the automotive industry. However, it is critical to determine thermal performance of an electric motor that is used for electric propulsion in order to optimize the cooling technology as well as to protect the motor from overheating that reduces the life of the motor significantly [4]. In this paper, thermal analysis on a 20 hP copper rotor induction motor will be investigated to determine optimal operating temperature of the motor.

On comparing TEFC copper rotor induction motor over aluminum rotor motor, there is a unique difference in their respective rotor geometry. CRIM has smooth rotor ends whereas aluminum rotor ends consist of fins as shown in the Figure 2.1. Such difference in the rotor geometry causes difference in the cooling effects in the motor. The fins on the aluminum rotor ends can create air circulation around end-winding that enhances the cooling performance overall. Due to the absence of rotor fins in CRIM, an increased temperature

rise within the motor is imminent. Several authors have proposed lumped parameter thermal network model for aluminum rotor induction motor considering forced convection heat transfer due to the rotor fins in the end winding region. But this paper proposes a thermal model of copper rotor induction motor where non-existent of forced convection heat transfer due to smooth rotor ends in the end-winding region is considered. In addition, the proposed model calculates temperature rise in transient perspective which will offer greater accuracy of the temperature rise prediction. Finally, calculated temperature rise will be compared with experimental results using RTD sensors and thermal imager to validate the model.

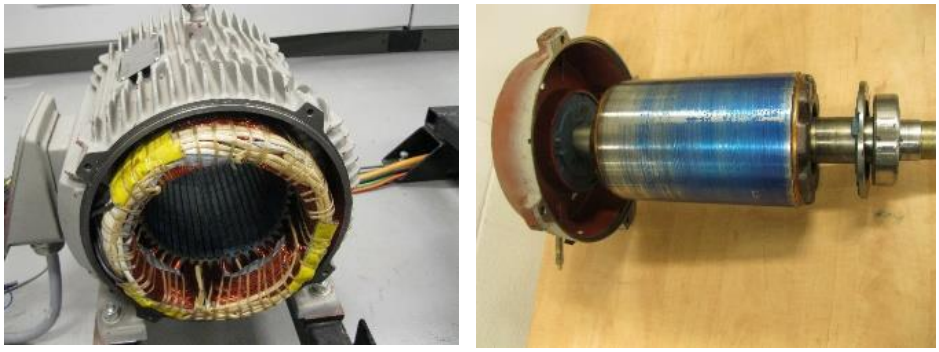

(a) (b)

Figure 2.1. Copper Rotor Induction Motor (a) Stator (b) Rotor.

2.2 Investigation of transient thermal behavior

2.2.1 Motor Loss Approximations

A 20 hp copper rotor induction motor was tested at 1500 rpm with three different loading 30 Nm, 50 Nm and 70 Nm. From different loading experiments current, voltage, input power, power factor was measured and recorded. Using (2.1) - (2.7) and equivalent circuit parameters for the test motor as presented in the Table 2.1 were used to calculate stator and rotor copper losses. In order to calculate stator core loss, no load tests were performed. All these loss components as presented in Table 2.2, except frictional losses were used in the thermal model in the following section.

$$P_{total-loss} = P_{co-stator} + P_{co-rotor} + P_{core} + P_{fric+wndg} \tag{2.1}$$

$$P_{total-loss} = P_{wdg-stator} + 2 \times P_{end-wndg} \tag{2.2}$$

$$P_{co-stator} = 3 \times R_S \times I_{S,rms}^2 \tag{2.3}$$

$$P_{end-wndg} = P_{co-stator} \times \left(L_{end-wndg} \Big/ L_{stator} \right) \tag{2.4}$$

$$P_{wndg} = P_{co-stator} \times \left(L_{wndg} \Big/ L_{stator} \right) \tag{2.5}$$

$$P_{co-rotor} = 3 \times R_r \times I_{R,rms}^2 \tag{2.6}$$

$$P_{core} = P_{input-noload} - P_{co-S-noload} - P_{fric+wndg} \tag{2.7}$$

$P_{total\text{-}loss}$	Total motor loss	$P_{fric+windage}$	Friction-windage losses
$P_{co\text{-}stator}$	Stator copper loss	R_s	Stator resistance
$P_{wndg\text{-}stator}$	Stator winding loss	R_r	Rotor resistance
$P_{end\text{-}wndg}$	End-winding loss	$I_{s,rms}$	Stator current
$P_{rotor\text{-}loss}$	Rotor copper loss	$I_{r,rms}$	Rotor current
$P_{input\text{-}noload}$	No load input power	L_{stator}	Stator winding length
$P_{co\text{-}s\text{-}nolaod}$	No load stator copper loss	$L_{wndg\text{-}stator}$	Winding length under core
$P_{core\ loss}$	Core loss	$L_{end\text{-}wndg}$	End-winding length

TABLE 2.1

COPPER ROTOR INDUCTION TEST MOTOR DATA SHEET

Test Motor Nameplate Data		Equivalent Circuit Parameters	
Parameter	Values	Parameter	Values (ohm)
Rated Power	20hp/14.92 kW	R_s	0.36
Rated Voltage	208/460 V	R_r	0.12
Rated Current	50.0/25 A	X_{ls}	1.71
Rated Speed	1,800 rpm	X_{lr}	1.71
Insulation Class	F	X_m	28.20

TABLE 2.2

MOTOR LOSSES (WATTS) FOR DIFFERENT LOADING AT 1,500 RPM

Losses	Loading (30Nm)	Loading (50Nm)	Loading (70Nm)
$P_{co\text{-}stator}$	263W	476W	622W
$P_{co\text{-}rotor}$	57W	121W	169W
$P_{end\text{-}wdg}$	49.95W	90.39W	118.12W
$P_{wdg\text{-}stator}$	163.11W	295.21W	385.75W
P_{core}	349W	383W	414W
$P_{fric+windage}$	210W		

2.2.2 Lumped Parameter (LPTN) Thermal Network Model

The most efficient procedure to analyze the heat transfer exchange in electric motor is based on lumped parameters, as indicated in many technical literatures of this subject. To estimate the temperature, rise in a copper rotor induction motor, the proposed lumped parameter thermal network model includes heat transfer processes such as convection, conduction and radiation. Figure 2.2 shows a thermal model in which active and significant heat sources in the motor are considered. All these losses in the motor contribute to heat generation which travels through the various components. Table 2.3 lists all the temperature nodes and thermal resistances. Thermal resistances to the heat transfer due to conduction, convection and radiation are defined at different material section of the motor components. Each location is defined as a temperature node where the material for that particular location is assumed to have uniform temperature distribution. Each node also consists of the thermal capacitances as described as C_1 to C_7 in the model which represents internal energy change in the material in transient perspective. At each temperature node, energy balance calculations are done to determine the temperature rise at various locations in the motor components.

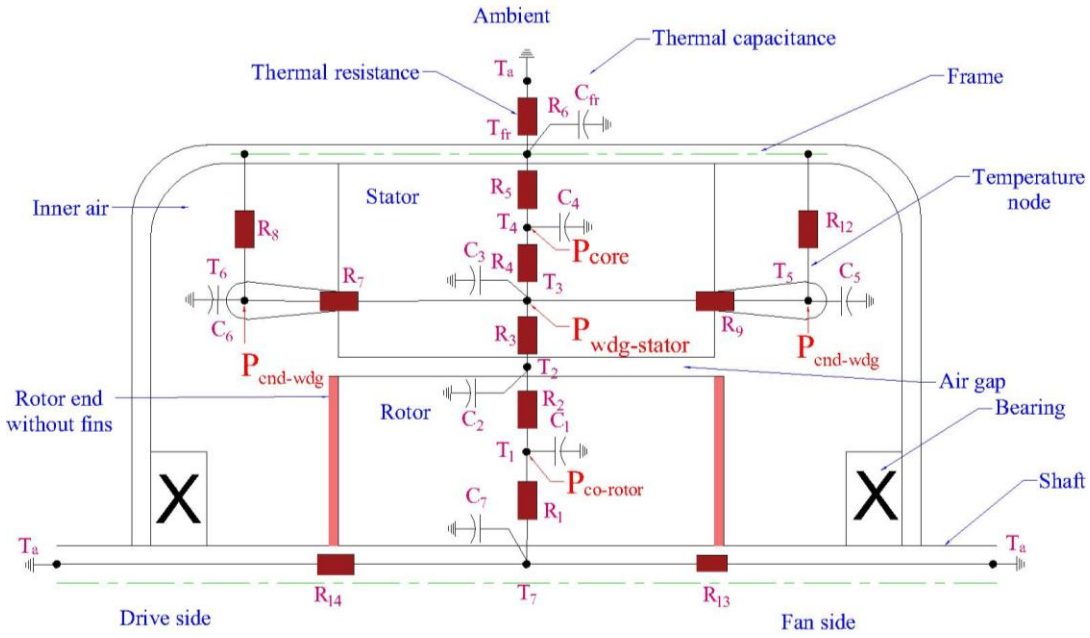

Figure 2.2. Proposed lumped parameter thermal network (LPTN) model for copper rotor induction motor.

In [5], for lumped heat capacity, rate of increase of internal energy equals to heat transfer by conduction plus heat transfer by convection plus heat transfer by radiation plus any active heat source present in the system which is expressed by the following general form of equation:

$$\rho cVdT/dt = \begin{bmatrix} P_{motor-loss} + h_{conv}A_{conv}\left(T_{conv} - T_{ref}\right) + \sigma\varepsilon A_{rad}\left(T_{rad}^4 - T_{ref}^4\right) \\ + \dfrac{\kappa A_{cond}}{\Delta x}\left(T_{cond} - T_{ref}\right) \end{bmatrix} \tag{2.8}$$

Here, h_c, T_{conv}, T_{cond} and T_{rad} are to vary with time and then (2.1) can be written in finite difference form suitable for numerical solution. Designating the temperatures at the start of a time increment with subscript (p) and the temperatures at the end of the time increment $\Delta\tau$ with subscript (p+1). Now, (2.8) becomes:

$$T_{p+1} = T_p + \left[\begin{Bmatrix} P_{motor-loss} + h_{conv}A_{conv}\left(T_{conv} - T_{ref}\right) + \sigma\varepsilon A_{rad}\left(T_{rad}^4 - T_{ref}\right) \\ + \kappa A_{cond}\left(T_{cond} - T_{ref}\right) \end{Bmatrix} \times \left(d\tau/\rho cV\right) \right] \tag{2.9}$$

$$dT_5 = \left[\left\{ P_{end-wdg} + \left\{\left(T_3 - T_5\right)/R_{10}\right\} + \left\{\left(T_3 - T_5\right)/R_{11}\right\} + \left\{\left(T_{fr} - T_5\right)/R_{12}\right\} \times \left(d\tau/C_8\right) \right\} \right] \tag{2.10}$$

In order to see separate heat transfer effects due to convection, conduction and radiation, (2.9) can be written as:

$$T_{p+1} = T_p + dT_{conv} + dT_{rad} + dT_{cond} \tag{2.11}$$

$$dT_{conv} = h_{conv}A_{conv}\left(T_{conv} - T_{ref}\right) \tag{2.12}$$

$$dT_{cond} = k \times A_{cond}\left(T_{cond} - T_{ref}\right) \tag{2.13}$$

$$dT_{rad} = \sigma \times \varepsilon \times A_{rad}\left(T_{rad}^4 - T_{ref}\right) \tag{2.14}$$

where,

ρ	fluid density (m^3/kg)	A_{conv}	convection area (m^2)
σ	Stefan-Boltzman constant	A_{cond}	conduction area (m^2)
κ	thermal conductivity (W/m.^{o}C)	A_{rad}	radiation area (m^2)
ε	Emissivity	T_{conv}	convection temperature (K)
c	specific heat capacity (kJ/kg/^{o}C)	T_{cond}	conduction temperature (K)

V	volume (m^3)	T_{rad}	radiation temperature (K)
h_c	Convection coefficient ($W/m^2.^oC$)	T_{ref}	Reference temperature (K)
$d\tau$	time increment (sec)		

In (2.8) - (2.14), T_{conv}, T_{cond}, T_{rad} and T_{ref} are used in the model using different respective temperature nodes T_1 to T_7 and T_{fr} as described in Table 2.3 and also describes the type of thermal resistances due to specific heat transfer mode either conduction, convection or radiation or combination of them that were used in energy balance equation (2.9) to calculate temperature rise at each node. Motor loss, $P_{motor\text{-}loss}$ in equation (2.9) uses the

TABLE 2.3

THERMAL NETWORK MODEL TEMPERATURE NODES AND THERMAL RESISTANCES

$P_{co\text{-}stator}$	Total Stator Copper losses	R_1	Resistance to conduction heat transfer through the shaft part below rotor core
$P_{end\text{-}wdg}$	End-winding copper losses	R_2	Resistance to conduction heat transfer from rotor copper to rotor surface/air gap
$P_{wdg\text{-}stator}$	Stator winding copper losses	R_3	Resistance to conduction heat transfer from airgap through stator teeth/insulation
$P_{co\text{-}rotor}$	Rotor Copper losses	R_4	Resistance to conduction heat transfer from stator teeth/insulation to stator core
P_{core}	Rotor Copper losses	R_5	Resistance to conduction heat transfer from stator core to motor frame
T_1	Rotor temperature	R_6	Combined resistance to forced convection heat transfer and radiation from motor frame
T_2	Air gap temperature	R_7/R_8	Combined resistance to conduction transfer from stator teeth/slot to end-winding
T_3	Stator winding temperature	R_9	Combined resistance to convection transfer from end-winding to inner air to motor frame
T_4	Stator core temperature	R_{10}/R_{11}	Combined resistance to conduction transfer from stator teeth/slot to end-winding
T_5	Stator end-winding fan side temperature	R_{11}	Combined resistance to convection transfer from end-winding to inner air to motor frame
T_6	Stator end-winding drive side temperature	R_{12}	Resistance to conduction transfer in axial direction through shaft to motor end-cap
T_7	Shaft temperature	R_{13}	Resistance to conduction transfer in axial direction through shaft to motor end-cap
T_{fr}	Motor frame temperature	T_a	Ambient temperature

calculated loss values such as rotor copper loss, stator copper loss and core loss from the Table 2.2 at the temperature nodes of T_1, T_3, T_4, T_5 and T_6 as shown in thermal network model. For example, the energy balance equation at each node will calculate incremental temperature rise for every $d\tau$ time interval and in this case, 5 seconds time increments were used. In this mathematical solution of the model temperature rise results, conduction, convection and radiation heat transfer coefficients were calculated using heat transfer relationships as well as physical dimensions of the test motor components. The thermal and physical parameters of the test motor are presented in Tables 2.4 and 2.5.

Table 2.4

THERMAL PROPERTIES AT ROOM TEMPERATURE CONSIDERED FOR THERMAL RESISTANCE AND CAPACITANCE CALCULATION

Material	Thermal conductivity (W/m^{o}C)	Specific heat capacity (J/kg^{o}C)	Density (m^3/kg)	Emissivity
Copper	386	383	8954	-
Iron	73	452	7897	0.72
Steel	54	465	7833	-
Air	0.02624	1,005	1.205	-

TABLE 2.5

KEY PHYSICAL DIMENSIONS CONSIDERED FOR THERMAL RESISTANCE CALCULATION

Parameter	Dimension	Parameter	Dimension
Rotor length	228 (mm)	Stator outer diameter	215 (mm)
Rotor outer diameter	154 (mm)	Stator inner diameter	150 (mm)
Shaft diameter	52 (mm)	End-winding outer diameter	220 (mm)
Air-gap	3.6 (mm)	End-winding inner diameter	190 (mm)
Effective Motor frame length	315 (mm)	End-winding axial extent	70 (mm)

Considering the novelty of this work, the key focus was to consider the differences in the rotor geometry of a copper rotor induction motor over an aluminum rotor induction motor. In calculating convection heat tranfer coefficients at the node of stator end-winding of T_5 and T_6, considering the effects of smooth rotor ends of this copper rotor test motor is a critical factor that reduces the cooling effects in the end-windings which is the hottest area in the motor coponents during its operation. In [6], the authors demonstrates a general

formula to calculate the convection heat transfer coefficient at the end-winding and this general formula was developed and validated by several authors in the analysis of end-winding thermal analysis for specifically aluminum rotor induction motor. Considering air circulation in the stator end-region a general formula to related convection heat transfer coefficient is given by:

$$h = k_1 \times \left[1 + \left(k_2 \times v\right)^{k_3}\right] \tag{2.15}$$

where, h is the convection heat transfer coefficient and is a function of inner air velocity v (m/s) and proportionality coefficients k_1, k_2 and k_3 that are dependent on turbulent airflow in the end region. As discussed in [7], it is difficult task to determine a representative value of inner air speed due to the end-windings geometry. So, the rotor peripheral speed was used to estimate inner air speed. References [7], [8] explained that while the motor is running, the inner air velocity around the end-windings increases with the increase of rotor speed due to the design of aluminum rotor that consists of fins and tips on the rotor short circuit rings assisting the heat exchange. Therefore, more air is circulated with the motor enclosure. Consequently, the aluminum rotor motors with TEFC design achieve higher cooling effects compared to copper rotor design. In [9], the equation (2.15) was used written to calculate convection coefficient which is expressed as:

$$h_{end-wdg} = 15.5 \times \left[1 + 0.29 \times v_{innerair}\right] \tag{2.16}$$

$$v_{innerair} = r_0 \omega \eta \tag{2.17}$$

where, $v_{innerair}$ is the air speed in the stator end-winding region, ω is the angular speed of the rotor and η is the fan efficiency. Due to smooth rotor geometry, the inner speed is considered to be very less and air circulation does not exist. Hence, convection heat transfer coefficient at the nodes of end-winding, $h_{end\text{-}wndg}$ is 15.5 W/m^2.^{0}C. Based on this value of convection heat transfer coefficient, thermal resistances, R_9 and R_{11} at the end-winding nodes were calculated using the equation which is expressed as:

$$R_{conv} = 1 \big/ h_{conv} A_{conv} \tag{2.18}$$

where, R_{conv} is the thermal resistance due to convection heat transfer, h_{conv} is the convection heat transfer coefficient and A_{conv} is the area of the convective area, in this case, the area of

the end-winding is considered. For thermal resistance due to conduction heat transfer the motor is assumed cylindrical and symmetrical. In radial direction, thermal resistance due to conduction heat transfer was calculated at different node by using the formula which is given by:

$$R_{cond} = \ln\left(\frac{r_o}{r_i}\right) \Big/ 2\pi\kappa L \tag{2.19}$$

where, r_o is the outer diameter, r_i is the inner diameter of the cylinder, κ is the thermal conductivity of the material and L is the length of the cylinder. In axial direction, the following formula was used as given by:

$$R_{cond} = \Delta x / \kappa A \tag{2.20}$$

where, Δx is the length, A is the area for the conduction.

2.3 Experimental Setup

A 20 hp totally enclosed fan cooling (TEFC) copper rotor induction motor was tested using variable frequency drive as shown in the Figure 2.3. In TEFC design the cooling fan is on the rotor shaft blowing the air over the motor surface externally only. For temperature measurements, RTDs (Resistance Temperature Detectors) sensors were embedded in the stator end-windings on the fan side and drive side in the test motor. RTDs are connected to computer through DAQ unit and temperature rise results were recorded. The motor was tested under varying speed and loading conditions to investigate the temperature rise at different state of motor operation. Also, an infrared thermal image camera was used to take thermal images of the motor surface at various state of operation of the test motor.

2.4 Results and Analysis

The motor was tested at speed of 1,500 rpm and different loading of 30 Nm, 50 Nm and 70 Nm. Each experiment was completed for a period of at least 2 hours to capture the trend

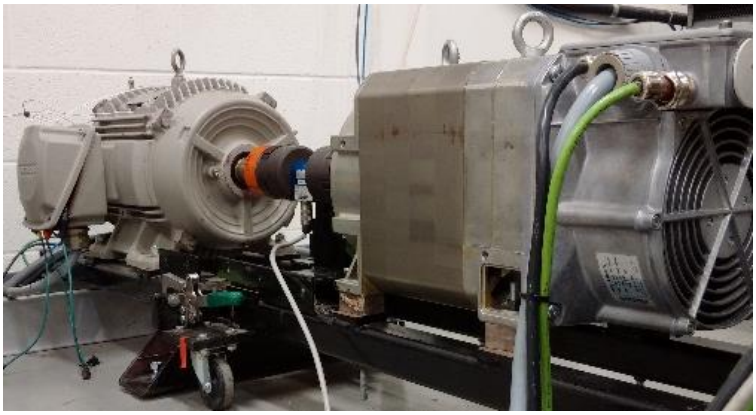

(a) Test Motor.

(b) Torque-Speed Controller

Figure 2.3. Thermal experimental test setup. (a) Test motor with the dyno. (b) Torque and speed monitor.

of the stator end-winding temperature rise approaching steady state conditions. Figure 2.4 demonstrates the temperature rise for three different loading. At higher loading the losses in the motor component is higher which contributes to the heat generation greatly. As a result, the temperature rise increases with the higher losses occurred in the motor. This motor is cooled by using an external fan in the enclosure which blows air around the motor frame. The thermal model is proposed which demonstrates prediction of temperature rise in the motor in a transient perspective. As described in section III, the model calculates all thermal resistances to the heat flow in the motor component due to conduction, convection and radiation. They were calculated using motor physical dimensions and thermal properties of the motor component materials following the heat transfer formulas as

described in the section III as well. The predicted temperature rise results at the stator end winding were compared to the experimental results which are shown in the Figures 2.5, 2.6 and 2.7 for 70 Nm loading, 50 Nm loading and 30 Nm loading respectively. The model takes different loss input for different loading conditions.

In all three conditions, the model predicts the results which are very close to the experimental results. Now the key consideration in the thermal model was to consider smooth rotor end geometry and accordingly heat transfer coefficients were calculated as input into the model. This agreement of temperature rise results demonstrates that due to smooth rotor end geometry lower convection coefficient in the end region is a critical factor for a copper rotor induction motor that enhances temperature rise in the motor thus requiring greater cooling compared to aluminum rotor induction motor. A thermal image camera was also used to take the temperature record on the motor frame as shown in the Figure 2.8 (a), (b) and (c) and both experimental techniques demonstrates the similar results which are useful to determine the operating temperature rise in the copper rotor induction motor.

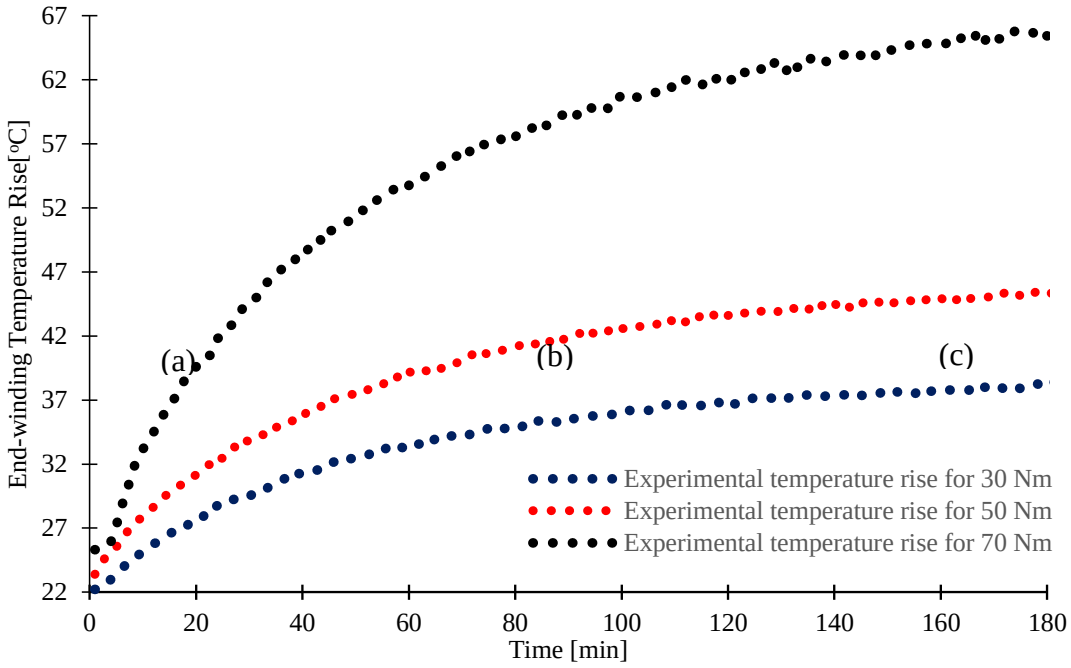

Figure 2.4. Experimental end-winding temperature rise at drive side for 1,500 rpm and loading 30 Nm, 50 Nm and 70 Nm with TEFC fan cooling.

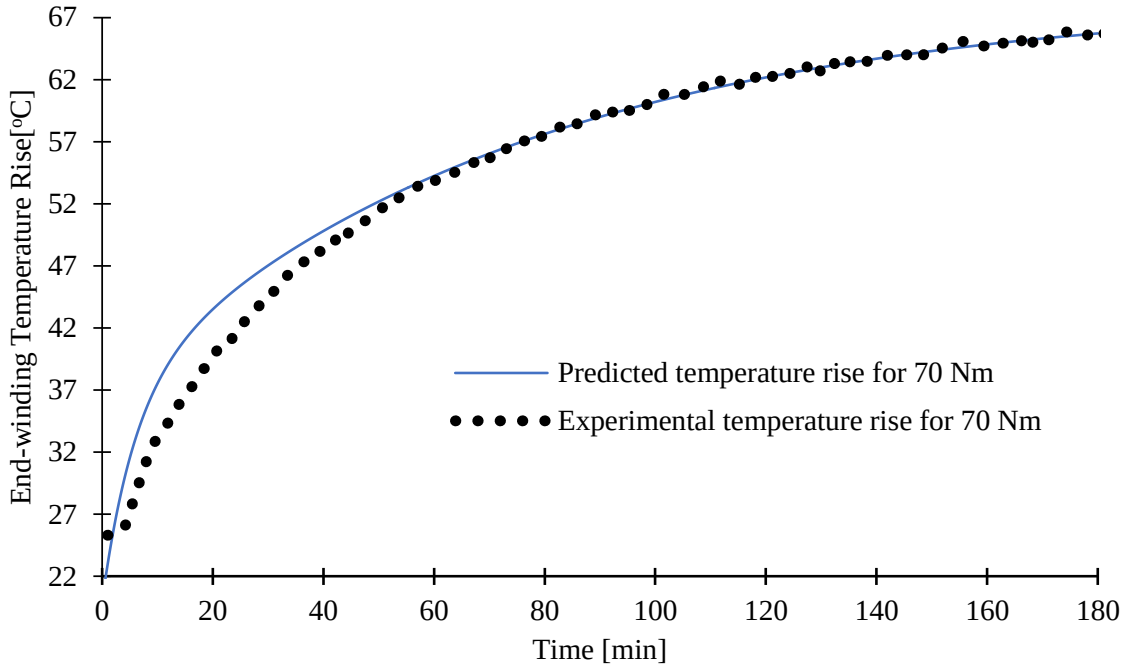

Figure 2.5. Comparison between experimental and predicted end-winding temperature rise at drive side for 1,500 rpm and 70Nm loading torque.

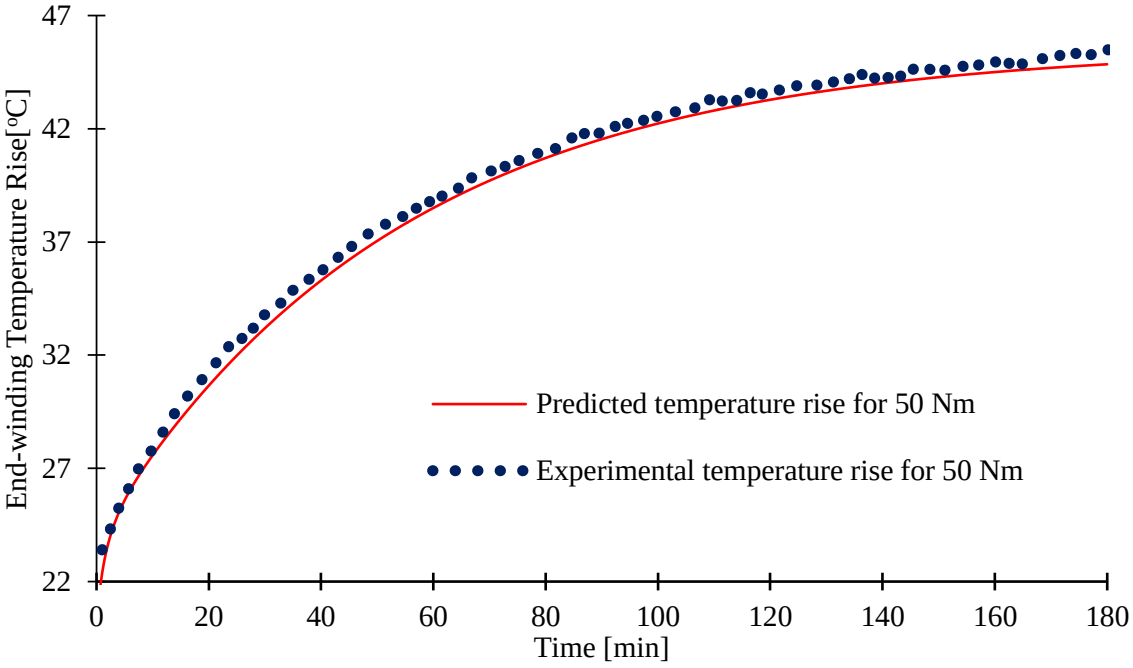

Figure 2.6. Comparison between experimental and predicted end-winding temperature rise at drive side for 1,500 rpm and 50 Nm loading torque.

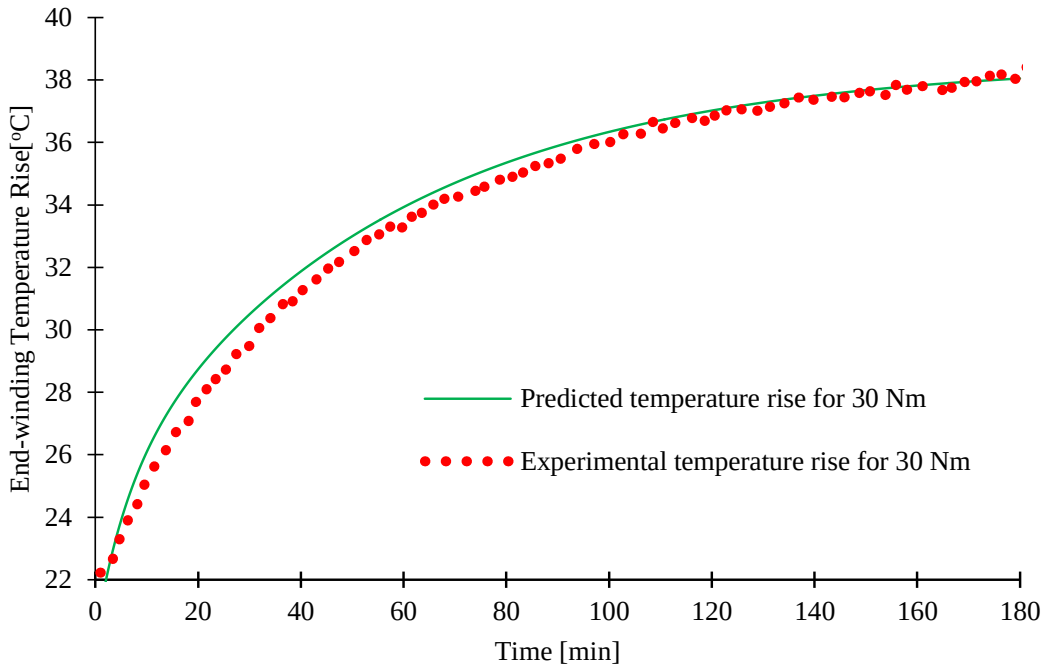

Figure 2.7. Comparison between experimental and predicted end-winding temperature rise at drive side for 1,500 rpm and 30 Nm loading torque.

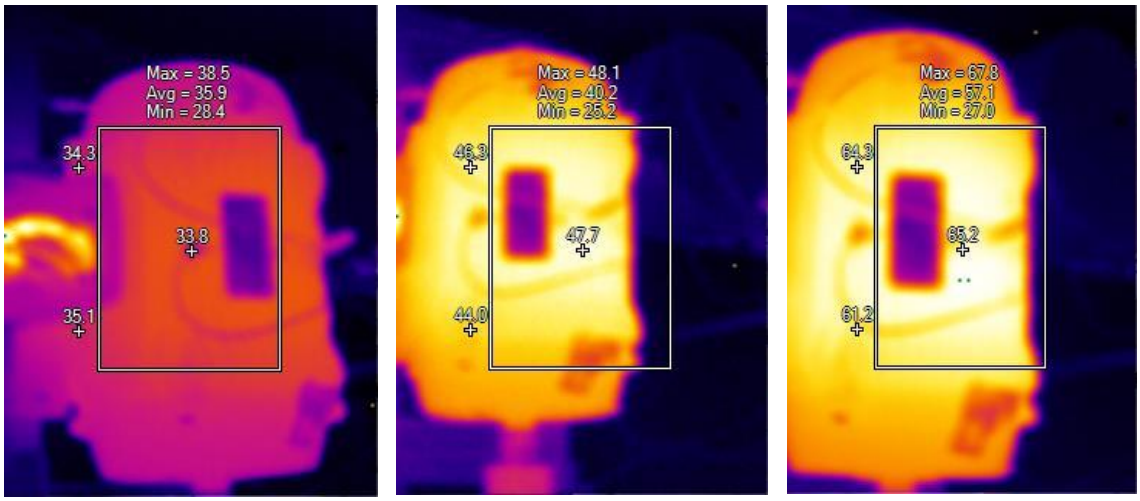

Figure 2.8. End-winding temperature rise at drive side for 1,500 rpm and loading torque. (a) 30 Nm. (b) 50 Nm. (c) 70 Nm with TEFC fan cooling.

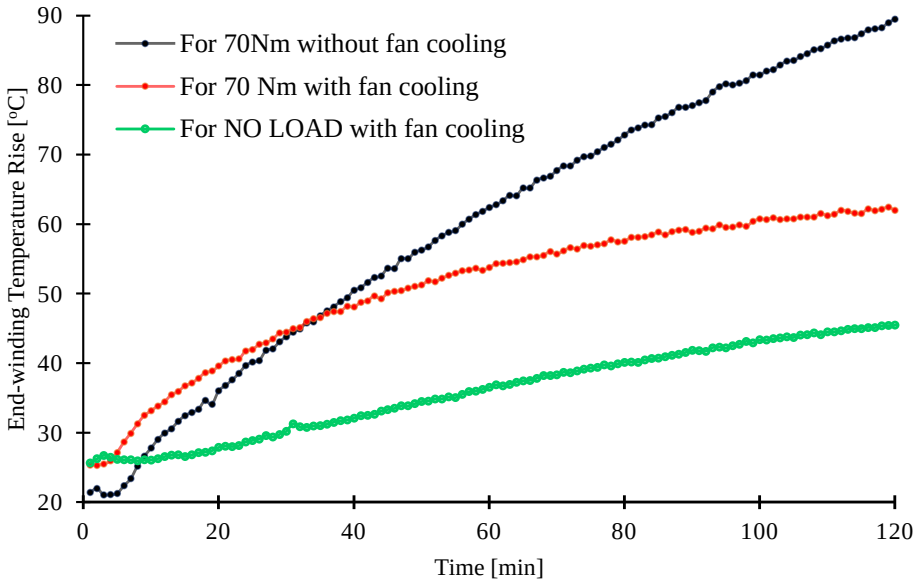

Figure 2.9. Comparison of End-winding temperature rise at drive side for TEFC fan cooling 70 Nm loading torque, without fan cooling and NO Loading torque.

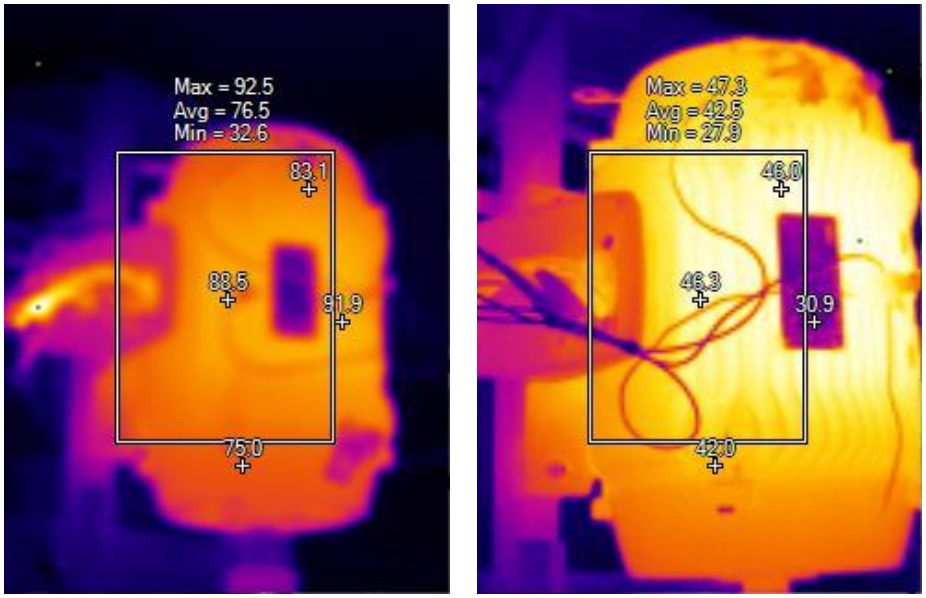

(a) (b)

Figure 2.10. End-winding temperature rise without fan cooling and loading. (a) 70 Nm. (b) 0 Nm. agrees with the temperature rise recorded using infrared camera technique.

In further experiments, without the fan cooling at 70 Nm loading, with fan cooling at 70 Nm loading and No load with fan cooling temperature rise were recorded and compared as

shown in the Figure 2.9 and 2.10. In these comparison, NO load temperature rise with fan cooling demonstrates heat generation in the motor caused by mainly the rotational losses. So, the differences in temperature rise for 70 Nm loading and No-load experiments with fan cooling quantifies the amount of heat generation caused by the copper losses in the stator and rotor. The temperature rise without fan cooling experiment shows the magnitude of the differences of heat generation compared to loading and no loading experiments.

2.5 Conclusion

The proposed lumped parameter thermal network model is validated for copper rotor induction motor where non-existent of forced convection heat transfer in the end-winding region due to smooth copper rotor ends is considered. The predicted results from the model agrees well with experimental results. Hence, the model accurately predicts the temperature rise in a copper rotor induction motor based on the calculated heat transfer coefficients at each node, particularly, convection heat transfer in the stator end region. As copper rotor motor is a competitive choice over permanent magnet motor in electric vehicle applications, this work will be useful in further investigation of thermal analysis on induction motor. The author would like to publish more work on this topic in quantifying the difference in temperature rise due to smooth rotor geometry by design and incorporating fins to create air circulation in the stator end-winding region. This thermal analysis is critical in understanding and determining thermal effects on copper rotor induction motor as well as it is important in designing effective air-cooling design to be implemented in EV/HEV applications.

2.6 References

[1] D. Peters, E. Brush, J. Kirtley, "Die-cast copper rotors as strategy for improving induction motor efficiency," Electrical Insulation Conference and Electrical Manufacturing Expo, Oct. 2007.

[2] E. Brush, “Motors with Copper Rotors Can Cost Less to Produce”, Copper Motor Rotor Update, Copper Development Association Inc., Vol.5, Issue 3, August 2005.

[3] J. Goss, M. Popescu and D. Staton, “Implications of real-world drive cycles on efficiencies and life cycle costs of two solutions for HEV traction: Synchronous PM motor vs Copper Rotor–IM”, Electric Powertrain Technologies Symposium, Germany, 2012.

[4] E. Ghosh; F. Ahmed; M.M.Sangdehi; N.C.Kar, "Temperature influenced online stator resistance estimation using an improved swarm intelligence technique for induction machine," in *IEEE Transportation Electrification Conference and Expo (ITEC),* June 2015.

[5] J.P., Holman.‘‘Heat Transfer” 9th ed., McGraw-Hill, 2002, pp. 640-647.

[6] A. Boglietti and A. Cavagnino, "Analysis of the end-winding cooling effects in TEFC induction motors," IEEE Transactions on Industry Applications, volume 43,issue 5, pp. 1214-1222, 2007.

[7] A. Boglietti, A. Cavagnino, D. Staton, and M. Popescu, “ Impact of different end region cooling arrangements on endwinding heat transfer coefficients in electric motors,” Proc. IEEE Conf. on Industrial Electronics, 978-1-4244-4649-0/09.

[8] A. Boglietti, A. Cavagnino, D. Staton, M. Popescu, C. Cossar, and M.I. McGilp, “End space heat transfer coefficient determination for different induction motor enclosure types”, IEEE Trans. on Industry Applications, vol. 45, No. 3, May/June 2009, pp. 929-937.

[9] A.Boglietti, A. Cavagnino, M. Lazzari, and M. Pastorelli, “A simplified thermal model for variable speed self-cooled industrial induction motor,” IEEE Transactions on Industry Applications, volume.39, No.4, July/August 2003, pp. 945-952.

CHAPTER 3

ANALYSIS OF END-WINDING THERMAL EFFECTS IN A TOTALLY ENCLOSED FAN COOLED INDUCTION MOTOR WITH DIE CAST COPPER ROTOR

3.1. Introduction

Due to the simplicity of construction, ruggedness, cost- effectiveness and low maintenance requirements, induction machines are widely used in the industries [1]. Despite these advantages, motor failure rate is approximately 3-5% per year and can be as high as 12%, specifically in the Pulp and Paper industry [2]. Such motor failure can cost a huge financial loss not only due to the motor repair or replacement but also the downtime of the process lines in the factories. Hence, the reliable motor protection is crucial in the industries to ensure smooth operation and targeted production. The detail causes of the motor failure are identified in the survey by IEEE and EPRI (Electric Power Research institute) and according to the survey, most of the failures are caused by the overheating of the motor components [3]. Approximately 35-40% motor failure are related to stator winding insulation and iron core [4]-[6]. Typically, the highest temperature is reached in the stator winding compared to any other motor component once motor thermal limit is exceeded and hence, the insulation breakdown is the common cause of motor failure [7]. "A rule of thumb accepted throughout industry says that there is a 50% reduction in insulation life for each 10^{o}C increase in the temperature" [8]. Since the stator insulation degradation is the main cause to motor failure, the National Electrical manufacturer's Association (NEMA) established that the permissible limit of the insulation class as presented in Table 3.1 [2], [9]. Considering the alarming statistics of motor failure, it is critical to monitor the stator winding temperature continuously and accurately to ensure that the permissible thermal limit is not exceeded and prevents a major breakdown or failure of the winding insulation. Many different techniques are used in the modern industries to protect thermal overload conditions. One of the techniques is embedding temperature measuring devices such as RTDs or thermocouples at the stator winding locations and measuring temperatures directly.

TABLE 3.1

TEMPERATURE LIMITS FOR DIFFERENT INSULATION CLASSES

Insulation Class	Ambient Temperature (^oC)	Rated Temperature Rise (^oC)	Hot Spot Allowance (^oC)	Insulation Temperature (^oC)
A	40	60	5	105
B	40	80	10	130
F	40	105	10	155
H	40	125	15	180

However, these techniques do not provide enough protection due to the non-uniform heating of the motor components including windings. In addition, these techniques are complex in installation and not cost-effective at all for small to medium scale mains fed induction machines [8]. Due to higher cost and complexity of installation of these embedded sensors, the conventional approach in the industries is to use thermal overload protection devices to monitor the stator winding temperature [8]. Thermal overload protection devices are operated based on thermal model and in this approach a simplified first order thermal model is developed using nameplate information of the motor. Hence, this method is too simple and heat dynamics in the motor is ignored to predict stator winding temperature accurately. As a result, it is critically important to develop a higher order thermal model that explains heat dynamics of the motor efficiently and estimates the temperature accurately. This paper proposes a higher order thermal model to predict stator winding temperature. A comparison of first order and higher order thermal models is presented and their accuracy in predicting winding temperature is investigated. In the development of the higher order thermal model, the paper also considers a unique difference in rotor geometry between a copper rotor induction motor and an aluminum rotor induction motor where the aluminum rotor has the fins on its rotor short circuit ring but the copper rotor does not have any fins. In order to validate predicted results from the proposed model, a 20 hp copper rotor induction motor has been tested under varying load and speed conditions where RTDs are used to measure the temperature at the stator end-windings.

3.2 Thermal Overload Protection Techniques and Thermal Model of Induction Motor

There are three categories of techniques to monitor the temperature of the stator windings such as direct temperature measurement, thermal model based technique and through parameter estimation. Direct measurement techniques involve using RTDs or thermocouples directly into the windings which are not simple and expensive in case of small to medium scale motors as explained in the previous section. Motor parameter based techniques are used as stator resistance changes with the changes of the temperature. However, as stated in [1], such stator resistance estimation is extremely difficult at higher speed operation and they are more susceptible to parametric errors. Thermal-model-based techniques are commonly used in the modern industries to estimate stator winding temperature. These techniques estimate stator winding temperature and then compare with thermal limit curves to ensure thermal overload protection of the motor. Thermal limit curves determine the safe operating point on time versus input current characteristic graph as shown in the Figure 3.1 [10].

Once the estimated temperature from the thermal model exceeds the permissible limit, the protection devices trip the motor. In thermal-model- based approach, both time delay fuses and microprocessor-based overload relays simulate this thermal limit curve. A simplified first order thermal model is commonly adopted in the industries, as shown in Figure 3.2(a). The first order model considers motor body as a uniform object, stator copper loss, $P_{cu\text{-}S}$ as only heat source, a single thermal resistance, R_{th}, a single capacitance C_{th}, stator winding temperature, T_s and ambient temperature, T_{amb}. Here, R_{th} & C_{th} represents the equivalent thermal resistance and equivalent thermal capacitance. The energy balance in the motor causing the temperature rise in the stator winding is expressed by [1]:

$$T_s(t) = I^2 R_s \times R_{th} \times \left(1 - e^{-\frac{t}{\tau}}\right) + T_{amb} \tag{3.1}$$

where, τ ($C_{th}R_{th}$) is the thermal time constant of the motor, R_S is the stator resistance. For a specific motor, the maximum permissible temperature is determined by the stator winding insulation material. The maximum permissible temperature is determined through maximum permissible current through stator winding which is expressed as [1]:

$$I_{\max} = \sqrt{\frac{T_{\max} - T_{amb}}{R_s R_{th}}} \tag{3.2}$$

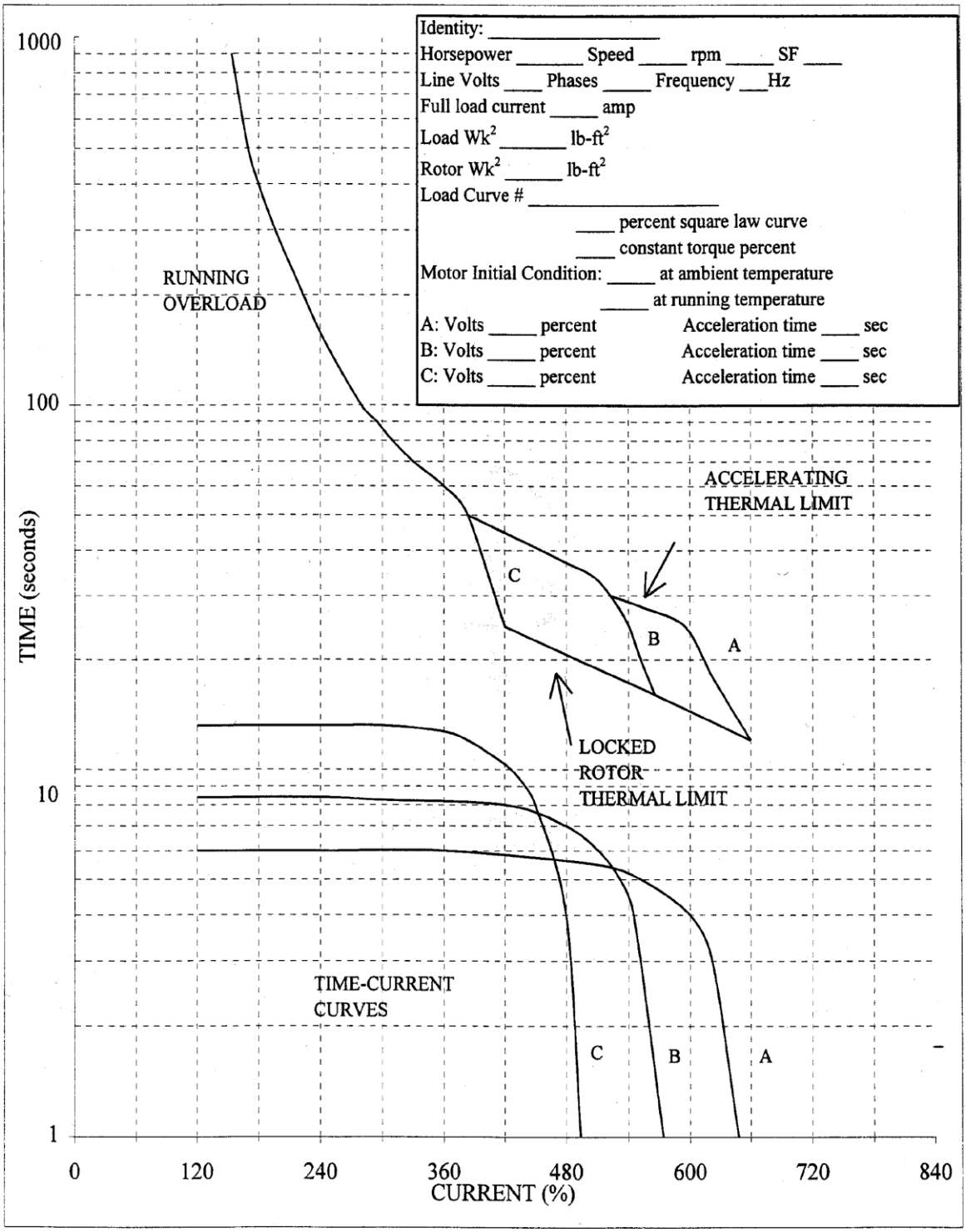

Figure. 3.1. Typical thermal limit curves per IEEE 620-1996 [10].

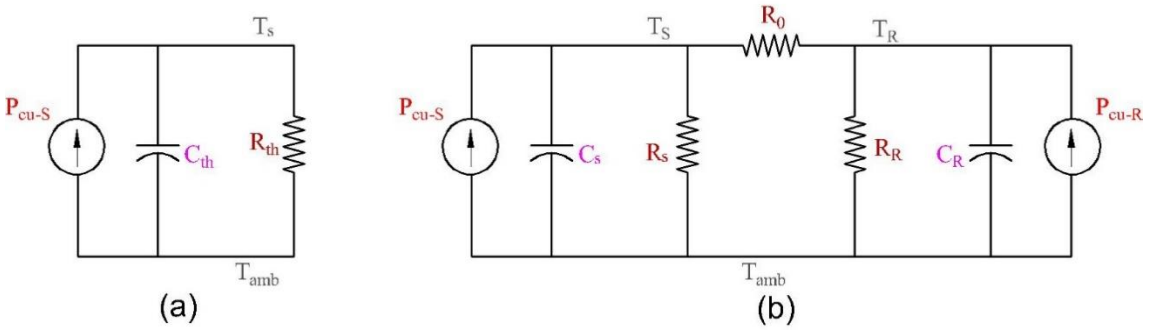

Figure. 3.2. A simplified thermal model. (a) First Order. (b) Second order.

Using (3.2) and service factor, SF of a particular motor, the expression for the time requirement to trip the motor is [1]:

$$t = \tau_{th} \ln\left(\frac{I^2}{I^2 - I_{rated}^2 \times SF}\right) \tag{3.3}$$

where, SF is a ratio of I_{max}/I_{rated}. In the above expression, using current is an alternative approach to calculate the time requirement to trip the motor once the maximum permissible temperature is reached. On the other hand, only consideration of a single thermal resistance and a single capacitance is extremely inadequate to represent the complete heat dynamics in the motor. A second order thermal model, as shown in Figure 2.2 (b) is also used in the industries to estimate the temperature rise where stator and rotor copper losses are considered. Since stator winding temperature rise is an accumulated effect from all different sources of power losses in the motor including copper losses, core losses, friction and windage losses; first order or second order simplified model are never capable of monitoring the stator winding temperature accurately [2]. In addition, all these losses that contribute to the heat generation in the motor components do change under different motor operating conditions and due to the characteristics and efficiency of the motor cooling mechanism. Moreover, the motor cannot be considered as a homogeneous body as assumed in the first order model and the heat distribution is different at the various locations of the motor components. Hence, higher order thermal circuit model based on multi nodal analysis considering physical and thermal characteristics of the motor components are critically important to determine the stator winding temperature accurately for thermal

overload protection. The predicted results from the first order and second order thermal model are compared with the higher order thermal model and experimental results.

3.3 Proposed Higher Order Thermal Model Solution

3.3.1Motor Loss Approximations

The use of copper in place of aluminum in an induction motor can lead to significant benefits such as higher efficiency due to its higher electrical conductivity, lower operating temperature rise due to lower resistive losses, extended life expectancy, reduction of the overall size and weight while maintaining the higher efficiency and low cost due to smaller machine [11],[12]. In comparison for a 50 kW aluminum rotor induction motor, losses were 4% higher and power and torque densities 5% lower than the equivalent copper rotor motor [12]. A 20 hp copper rotor induction motor was tested at 1500 rpm with three different loading 30 Nm, 50 Nm and 70 Nm. Table 3.2 shows equivalent circuit parameters for the test motor that were used to calculate stator and rotor copper losses. In order to calculate stator core loss, no load tests were performed. In estimating the stator end windings copper losses and its impact on generating heat, it is important to know the length of the end windings with respect to the total length of windings for each phase. The joule losses causing end windings heating will be a proportional to the total joule losses caused by the whole length of the windings and is simplified by the following relationship:

$$P_{end-wdg} = P_{cu_S} \times \left(L_{end-wdg} \Big/ L_S \right) \tag{3.4}$$

where, $L_{end\text{-}wdg}$ is the stator end-winding length, L_S is the total stator winding length. Table 3.3 presents all the loss values that are used in thermal model in the following section for calculating predicted temperature rise at various nodes of the different motor components.

TABLE 3.2

COPPER ROTOR INDUCTION TEST MOTOR DATA

Test Motor Nameplate Data		Equivalent Circuit Parameters	
Parameter	Values	Parameter	Values (ohm)
Rated power	14.92 kW	R_s	0.36
Rated voltage	208/460 V	R_R	0.12
Rated current	50.0/25 A	X_{ls}	1.71
Rated speed	1,800 rpm	X_{lr}	1.71
Insulation class	F	X_m	28.20

TABLE 3.3

COPPER ROTOR INDUCTION MOTOR LOSSES AT 1,500 RPM

Loading	$P_{cu\text{-}S}$ (Watt)	$P_{cu\text{-}R}$ (Watt)	$P_{end\text{-}wdg}$ (Watt)	P_{core} (Watt)	P_{f+w} (Watt)
30 Nm	264	57	49.95	349	210
50 Nm	476	121	90.39	383	210
70 Nm	622	169	118.12	414	210

3.3.2 Higher Order Thermal Model

The most efficient procedure to analyze the heat transfer exchange in an electric motor is based on lumped parameters, as indicated in many technical literatures of this subject [13]-[18]. Lumped heat capacity system refers to the system that may be considered uniform in temperature. In lumped-heat-capacity analysis, it considers that the internal resistance of the body is negligible in comparison with the external resistance [19]. As the motor is built from different materials, heat transfer will be different through different motor components. Each motor component is considered as lumped heat capacity element which is considered to be uniform in temperature. A lumped parameter model consists of thermal resistances and capacitances to build a thermal network where heat transfer takes place through several paths in the motor. Each motor component is considered as a temperature node. In steady-state analysis, the net energy transfer into the node is zero, while for the unsteady-state analysis, the net energy transfer into the node must be evidenced as an increase in internal energy of the element. Each node behaves like a small lumped heat capacity and the interaction of the all the nodes determines the thermal behavior of the motor in a transient process. In order to determine the temperature rise at the various components or at each node, it requires only dimensional information and thermal parameters. It is much easier and faster to compute the temperature rise using heat transfer principles and formulas. The motor is considered as a cylindrical structure and symmetrical around the shaft axis. Hence, the model shows the heat transfer in radial direction from the center of the shaft axis towards the frame as shown in the Figure 3.3. As it is considered as cylindrical structure, heat transfer through each of the cylinder is assumed to be uniform in radial direction and the only heat transfer takes place in axial direction through the shaft, then to the endcaps. On the other hand, the end-windings are identified the hottest points

inside a totally enclosed fan-cooled (TEFC) induction motor [15]. Hence, in order to estimate the stator end-winding temperature in a copper rotor induction motor, a modified higher order thermal network model is proposed, as shown in the Figure 3.4. Table 3.4 lists all the active and significant heat sources, temperature nodes and thermal resistances and capacitances. Thermal resistances to the heat transfer due to conduction, convection and radiation are defined at different material section of the motor components. Each location is defined as a temperature node, such as T_1 to T_{10}, T_{fr}, T_{fin} and T_{amb}, where the material for that particular location is assumed to have uniform temperature distribution. Each node also consists of the thermal capacitances such as C_1 to C_{10}, C_{fr} and C_{fin} in the model which represent internal energy change in the material in the transient perspective. At each temperature node, energy balance calculations are performed to determine the temperature rise at various locations in the motor components. The heat sources in the motor are uniformly distributed. In [19], for lumped heat capacity, rate of increase of internal energy equals to heat transfer by conduction plus heat transfer by convection plus heat transfer by radiation plus any active heat source present in the system which is expressed by the following general form of equation:

$$\rho c V dT / dt = \begin{bmatrix} P_{motor-loss} + h_{conv} A_{conv} \left(T_{conv} - T_{ref} \right) \\ + \sigma \varepsilon A_{rad} \left(T_{rad}^4 - T_{ref}^4 \right) + \frac{\kappa A_{cond}}{\Delta x} \left(T_{cond} - T_{ref} \right) \end{bmatrix} \tag{3.5}$$

Here, h_{conv}, T_{conv}, T_{cond} and T_{rad} are to vary with time and then (3.5) can be written in finite difference form suitable for numerical solution. Designating the temperatures at the start of a time increment with subscript (p) and the temperatures at the end of the time increment dt with subscript (p+1), now (3.5) becomes:

$$T_{p+1} = T_p + \left[\left\{ \begin{matrix} P_{motor-loss} + h_{conv} A_{conv} \left(T_{conv} - T_{ref} \right) + \sigma \varepsilon A_{rad} \left(T_{rad}^4 - T_{ref}^4 \right) \\ + \frac{\kappa A_{cond}}{\Delta x} \left(T_{cond} - T_{ref} \right) \end{matrix} \right\} \times \left(dt / \rho c V \right) \right] \tag{3.6}$$

In order to see separate heat transfer effects due to convection, conduction and radiation, (3.6) can be written as:

$$T_{p+1} = T_p + \left[\left\{ P_{motor-loss} \times \left(dt / \rho c V \right) \right\} + dT_{conv} + dT_{rad} + dT_{cond} \right] \tag{3.7}$$

$$T_{p+1} = T_p + \left[\left\{ P_{motor-loss} \times \left(dt / \rho c V \right) \right\} + dT_{conv} + dT_{rad} + dT_{cond} \right] \tag{3.8}$$

$$dT_{conv} = h_{conv} A_{conv} \left(T_{conv} - T_{ref} \right) \times \left(dt / \rho c V \right) \tag{3.9}$$

$$dT_{cond} = \frac{\kappa A_{cond}}{\Delta x} \left(T_{cond} - T_{ref} \right) \times \left(dt / \rho c V \right) \tag{3.10}$$

$$dT_{rad} = \sigma \varepsilon A_{rad} \left(T_{rad}^4 - T_{ref}^4 \right) \times \left(dt / \rho c V \right) \tag{3.11}$$

In (3.5)-(3.10), T_{conv}, T_{cond}, T_{rad} and T_{ref} are used in the model using different respective temperature nodes from T_1 to T_{10}, T_{fr}, T_{fin} and T_{amb}. Motor loss, $P_{motor\text{-}loss}$ in (3.6) uses the calculated loss values such as rotor copper loss, stator copper loss, core loss and friction loss from the Table 3.3 at the temperature nodes of T_1, T_5, T_6, T_8 and T_{10} as shown respectively in thermal network model in Figure 3.4. For example, the energy balance equation at each node will calculate incremental temperature rise for every *dt* time interval and in this case, 5 seconds time increments were used. In the mathematical solution of the model to calculate temperature rise, conduction, convection and radiation heat transfer coefficients were calculated using heat transfer relationships as well as physical dimensions of the test motor components. The thermal and physical parameters of the test motor are presented in Table 3.5 and Table 3.6.

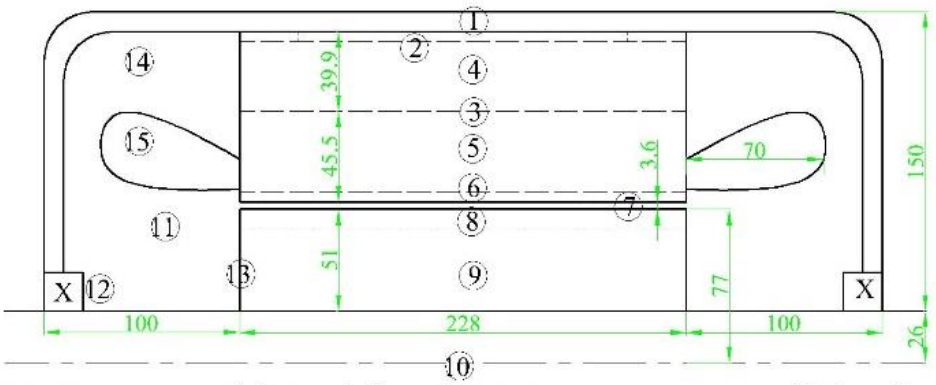

1) Motor Frame
2) Stator yoke upper
3) Stator yoke lower
4) Stator core
5) Stator winding
6) Stator teeth
7) Air-gap
8) Rotor Copper
9) Rotor Iron
10) Shaft axis
11) Air around end-widning
12) Bearing
13) Smooth rotor end
14) Non-ventilated
15) End-winding

Note: All dimensions are in millimeters.

Figure. 3.3. Induction motor construction for the proposed thermal model.

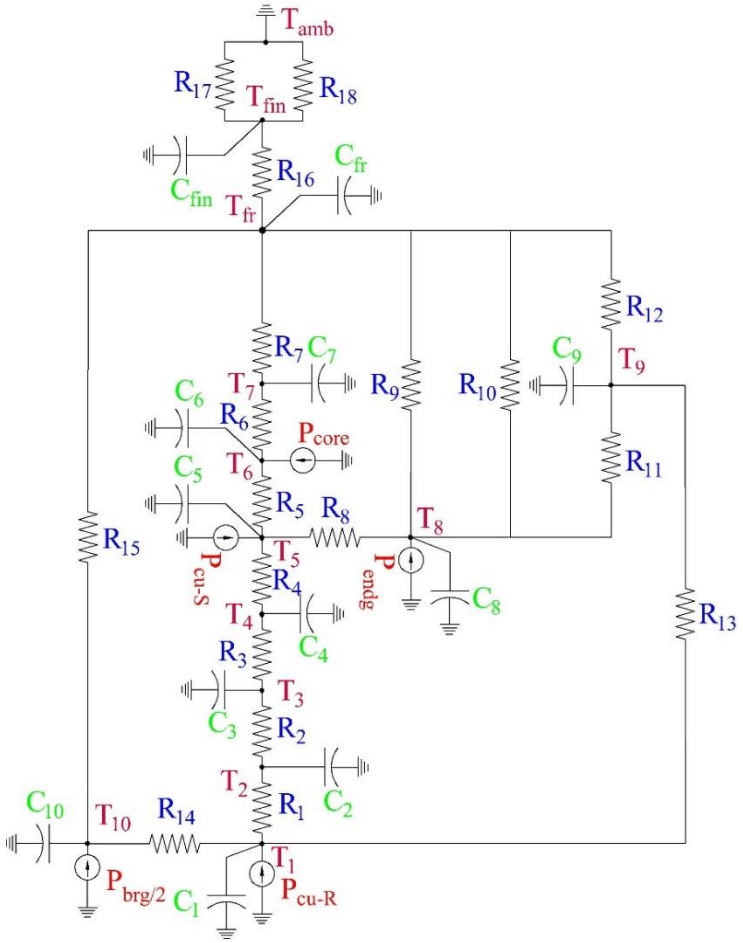

Figure. 3.4. A proposed higher order thermal network model.

TABLE 3.4

LUMPED PARAMETER THERMAL NETWORK MODEL PARAMETER

Thermal Parameter	Description of model parameters	Thermal Parameter	Description of model parameters
$P_{\text{cu-S}}$	Stator copper losses	C_7	Thermal capacitance of stator yoke upper half
$P_{\text{cu-R}}$	Rotor copper losses	R_8	Equivalent resistance due to axial conduction between stator windings and stator end-winding
P_{endg}	Stator end-winding losses	C_8	Thermal capacitance of stator end-windings
P_{core}	Core losses	R_9	Resistance due to conduction between end-winding and frame
$P_{\text{brg/2}}$	Half the friction loss at the bearing	R_{10}	Resistance due to radiation from stator end-winding to the frame
R_1	Resistance due to conduction between rotor copper and rotor	R_{11}	Resistance due to convection from end-winding to inner air
C_1	Thermal capacitance of rotor lamination material	C_9	Thermal capacitance of inner air
R_2	Resistance due to convection between rotor and air gap	R_{12}	Resistance due to convection from inner air to the endcap
C_2	Thermal capacitance of rotor copper material	R_{13}	Resistance due to convection between rotor end and inner air
R_3	Resistance due to convection between air gap and stator teeth	R_{14}	Resistance due to conduction between rotor iron & shaft
C_3	Thermal capacitance of air in the air-gap	R_{15}	Resistance due to conduction between bearing housing & frame
R_4	Resistance due to radial conduction between stator teeth and stator winding	R_{16}	Resistance due to conduction through fins
C_4	Thermal capacitance of stator teeth	R_{17}	Resistance due to radiation heat transfer from frame to ambient
R_5	Resistance due to radial conduction through stator yoke lower half	R_{18}	Resistance due to convection from frame to ambient
C_5	Thermal capacitance of stator winding	C_{10}	Thermal capacitance of the bearing housing
R_6	Resistance due to conduction through stator yoke upper half	C_{fr}	Thermal capacitance of frame
C_6	Thermal capacitance of stator yoke lower half	C_{fin}	Thermal capacitance of fins
R_7	Resistance due to conduction through interface gap between stator core and motor frame		

TABLE 3.5

THERMAL PROPERTIES AT ROOM TEMPERATURE CONSIDERED FOR THERMAL RESISTANCE AND CAPACITANCE CALCULATION

Material	Thermal conductivity (W/m.^{o}C)	Specific heat capacity (J/kg.^{o}C)	Density (kg/m^{3})	Emissivity
Copper	386	383	8954	-
Iron	73	452	7897	0.72
Steel	54	465	7833	-
Air	0.02624	1005	1.205	-

TABLE 3.6

KEY PHYSICAL DIMENSION DATA OF THE TEST MOTOR

Motor components	Values (meter)	Motor components	Values (meter)
Stator outer diameter	0.215	Shaft length (rotor)	0.228
Stator inner diameter	0.150	Shaft length from rotor end to the bearing	0.100
End-winding outer diameter	0.220		
End-winding inner diameter	0.190	Air thickness between rotor and endcap	0.036
End-winding axial length	0.070	Rotor yoke inner radius	0.098
Rotor length	0.228	Rotor yoke outer radius	0.107
Rotor outer diameter	0.154	Frame fin length	0.254
Shaft diameter	0.052	Frame fin width	0.007
Airgap length	0.0036	Rotor lamination thickness	0.0387
Frame length	0.315	Air thickness between rotor and endcap	0.036

3.3.3 Analytical Solution of Temperature rise in LPTN Model

Node 1, T_1: Temperature rise in the Rotor Copper

Rotor copper loss, $P_{cu\text{-}R}$ represent the heat generation at the rotor that travels radially (rotor copper-rotor lamination-air gap-stator-iron core-motor frame-ambient) and axially from rotor end surface-inner air.

$$dT_1 = \frac{dt}{C_1} \times \left[P_{cu-R} + \left\{ \left(T_2 - T_1 \right) / R_1 \right\} + \left\{ \left(T_9 - T_1 \right) / R_{13} \right\} + \left\{ \left(T_{10} - T_1 \right) / R_{14} \right\} \right] \tag{3.12}$$

$$R_1 = \frac{1}{2\pi\, l_{rot} k_{lam}} \ln\left(\frac{r_{rot}}{r_{shaft}}\right) \tag{3.13}$$

where, r_{rot} is outer radius of the rotor and l_{rot} is rotor length, r_{shaft} is rotor shaft radius and k_{lam} heat conductivity of rotor lamination.

$$R_{13} = 1 \Big/ A_{rot-end} h_{r-iair} \tag{3.14}$$

where, $A_{rot\text{-}end}$ is the rotor end area which can be determined using (3.15).

$$A_{rot-end} = \frac{\pi \times \left(r_{rot}^2 - r_{shaft}^2\right)}{2} \tag{3.15}$$

$h_{r\text{-}iair}$ is the combined free and forced convection heat transfer coefficient in the space between the rotor end and inner air under the end-winding. As the flow situation in the end space between the rotor and endcap is complex in nature, $h_{r\text{-}iair}$ has been calculated using Schubert's expression as described in (3.16), which is also used for calculating convection coefficient, $h_{end\text{-}wdg}$ due to free and forced convection from end-winding to inner air.

$$R_{14} = \frac{1}{2\pi \mathrm{k_{ir}} l_{st}} \ln \frac{r_{rot-y-o}}{r_{rot-y-i}} + \frac{1}{4}\left(\frac{0.5 l_{st}}{\mathrm{k_{ir}} \pi r_{rot-y-i}^2}\right) + \frac{1}{2}\left\{\frac{0.5\left(l_{shaft} - l_{st}\right)}{\mathrm{k_{ir}} \pi r_{rot-y-i}^2}\right\} \tag{3.16}$$

where, $r_{rot\text{-}y\text{-}i}$ is the rotor yoke inner radius, $r_{rot\text{-}y\text{-}o}$ is the rotor yoke outer radius, l_{shaft} is the shaft length, $\mathrm{k_{ir}}$ is the thermal conductivity of iron [20].

Node 2, T_2: Temperature rise at the rotor surface

$$dT_2 = \frac{dt}{C_2} \times \left[\left\{\left(T_1 - T_2\right) \Big/ R_1\right\} + \left\{\left(T_3 - T_2\right) \Big/ R_2\right\}\right] \tag{3.17}$$

$$R_2 = 1 \Big/ A_{rot} h_{airgap} \tag{3.18}$$

Where, $A_{rot}=2\pi r_{rot} l_{rot}$, rotor outer surface area; h_{airgap} is the forced convection coefficient of the air gap which depends on the air-gap length, rotation speed of the rotor, the length

of the rotor and the kinematic viscosity of the streaming fluid. The following equation can be used to determine the heat transfer coefficient from the rotor to the air gap:

$$h_{airgap} = {\mathrm{Nu} \times \kappa_{\mathrm{air}}} \Big/ {l_{airgap}} \tag{3.19}$$

Where, Nu is Nusselt number, κ_{air} is thermal conductivity of air and l_{airgap} is the thickness of the air gap.

According to Becker and Kaye [21], Nusselt number is:

$\mathrm{Nu}=2$ for $\mathrm{Ta_m}<1{,}700$ (laminar flow)

$\mathrm{Nu}=0.128\mathrm{Ta_m}^{0.367}$ for $1{,}700< \mathrm{Ta_m} <10^4$

$\mathrm{Nu}=0.409\mathrm{Ta_m}^{0.241}$ for $1{,}700< \mathrm{Ta_m} <10^4$

$\mathrm{T_a}$ is the Taylor number and the following Taylor equation can be used to determine the flow type:

$$\mathrm{T_a} = \frac{\rho^2 \omega^2 r_m \delta^3}{\mu^2} \tag{3.20}$$

where, ω is the angular velocity of the rotor, ρ is the mass density of the fluid, μ is the dynamic viscosity of the fluid and r_m is the average of the rotor and stator radii. The radial air-gap length, δ and the rotor radius are taken into account by a modified Taylor number:

$$\mathrm{T_a}_m = {\mathrm{T_a}} \Big/ {F_g} \tag{3.21}$$

where, F_g is the geometrical factor. In practice, the air-gap length is so small compared with the rotor radius that F_g is close to unity and $\mathrm{Ta}_m \approx \mathrm{Ta}$.

Node 3, T_3: Temperature rise at the air gap

$$dT_3 = \frac{dt}{C_3} \times \left[\left\{ {(T_2 - T_3)} \Big/ {R_2} \right\} + \left\{ {(T_4 - T_3)} \Big/ {R_3} \right\} \right] \tag{3.22}$$

$$R_3 = {1}/{A_{st} h_{airgap}} \tag{3.23}$$

where, $A_{st}=2\pi r_{st} l_{st}$= stator inner surface, r_{st} is the inner radius of the stator, h_{airgap} calculated in (3.17) will be the same in (3.21).

Node 4, T_4: Temperature rise at the stator teeth

$$dT_4 = \frac{dt}{C_4} \times \left[\left\{ {(T_3 - T_4)}/{R_3} \right\} + \left\{ {(T_5 - T_4)}/{R_4} \right\} \right] \tag{3.24}$$

$$R_4 = \frac{1}{2\pi \kappa_{ir} l_{st}} \ln\left(\frac{r_{st-y-i}}{r_{st}} \right) \tag{3.25}$$

where, $r_{st\text{-}y\text{-}i}$ is the stator yoke inner radius.

$$R_8 = {\Delta x_{ins}}/{A_{slot} \kappa_{ins}} \tag{3.26}$$

where, A_{slot} is the slot area, Δx_{ins} is the thickness of insulating material, κ_{ins} is the conductivity of insulating material.

Node 5, T_5: Temperature rise at stator winding

$$dT_5 = \frac{dt}{C_5} \times \left[P_{cu-S} + \left\{ {(T_4 - T_5)}/{R_4} \right\} + \left\{ {(T_6 - T_5)}/{R_5} \right\} + \left\{ {(T_8 - T_5)}/{R_8} \right\} \right] \tag{3.27}$$

$$R_5 = \frac{1}{2\pi \kappa_{ir} l_{st}} \ln\left\{ \frac{{\left(r_{st-y-i} + r_{st-y-o} \right)}/{2}}{r_{st-y-i}} \right\} \tag{3.28}$$

where, $r_{st\text{-}y\text{-}o}$ is the stator yoke outer radius [20].

Node 6, T_6: Temperature rise at the stator yoke (lower)

$$dT_6 = \frac{dt}{C_6} \times \left[P_{core} + \left\{ {(T_5 - T_6)}/{R_5} \right\} + \left\{ {(T_7 - T_6)}/{R_6} \right\} \right] \tag{3.29}$$

$$R_6 = \frac{1}{2\pi\kappa_{\text{ir}} l_{st}} \ln\left\{ \frac{\left(r_{st-y-i} + r_{st-y-o} \right) / 2}{r_{st-y-o}} \right\} \tag{3.30}$$

Node 7, T_7: Temperature rise at the stator yoke (upper)

$$dT_7 = \frac{dt}{C_7} \times \left[\left\{ \left(T_6 - T_7 \right) / R_6 \right\} + \left\{ \left(T_{fr} - T_7 \right) / R_7 \right\} \right] \tag{3.31}$$

$$R_7 = \frac{l_{i-airgap}}{2\pi\kappa_{\text{air}} r_{st-y-o} l_{st}} \tag{3.32}$$

where, $r_{st\text{-}y\text{-}o}$ is the stator yoke outer radius and $l_{i\text{-}airgap}$ is the airgap length between the interfaces. As stated in [21], the equivalent thermal resistance of joint surfaces can be modelled by equivalent air gap conduction. There is small gap between the surfaces due to surface roughness. The equivalent air gap length given for frame to stator core is 0.05 - 0.08 length/mm.

Node 8, T_8: Temperature rise at the stator end-winding

$$dT_8 = \frac{dt}{C_8} \times \left[\begin{array}{l} P_{end-winding} + \left\{ \left(T_5 - T_8 \right) / R_8 \right\} + \left\{ \left(T_{fr} - T_8 \right) / R_9 \right\} + \left\{ \left(T_{fr} - T_8 \right) / R_{10} \right\} \\ + \left\{ \left(T_9 - T_8 \right) / R_{11} \right\} \end{array} \right] \tag{3.33}$$

$$R_9 = \frac{1}{2\pi\kappa_{\text{air}} l_{ew}} \ln\left(\frac{r_{ew-o}}{r_{ew-i}} \right) \tag{3.34}$$

where, l_{ew} is the length of the end-winding, $r_{ew\text{-}o}$ is the outer radius of end-winding, $r_{ew\text{-}i}$ is the inner radius of end-winding and k_{air} is the conductivity of the inner air.

$$R_{10} = \frac{1}{\sigma\varepsilon A_{ew} \left[\left(T_{fr} + T_8 \right) \times \left(T_{fr}^2 + T_8^2 \right) \right]} \tag{3.35}$$

where, A_{ew} is the end-winding area, σ is the Boltzman's constant and ε is the emissivity.

$$R_{11} = 1 \Big/ A_{ew} h_{end-wdg} \tag{3.36}$$

where, $h_{end\text{-}wdg}$ is the combined free and forced convection coefficient between the end-winding and the inner air.

The heat flow analysis in the stator end-winding region is somewhat complex. So, the determination of the convection heat transfer coefficients require careful considerations of the parameters that explain all different heat transfer mechanism likely to take place in the end-region. As stated in [21], the end-winding space of a squirrel cage induction motor can be divided into two parts such as the space between the end-winding and the motor frame and the space between the rotor fins and the end-winding. As described earlier, the aluminum rotor squirrel cage induction motor has the rotor that consists the fins or blades on the short circuit rings as shown in Figure 3.5. These fins or blades cause air circulation in the space between end-winding and the rotor as shown in Figure 3.6. On the other hand, in copper rotor motor, such air circulation is much less dominant due to smooth rotor ends as shown in Figure 3.7. From literature review, the authors consider that in case of copper rotor that has no fins on its end-rings, heat transfer will take place in the end-winding region by combined free and forced convection. As stated in [19], free and forced convection situation arise when a fluid is forced over a heated surface at a rather low velocity. Coupled with forced-flow velocity is a convection velocity that is generated by the buoyancy forces resulting from a reduction in fluid density near the heated surface. The general notion that is applied in combined convection analysis is that the predominance of a heat transfer mode is governed by the fluid velocity associated with the mode. A forced-convection situation involving a fluid velocity of 30 m/s, for example, would be expected to overshadow most free convection effects encountered in ordinary gravitational fields because the velocities of the free convection currents are small in comparison with 30 m/s. On the other hand, a forced flow situation at very low velocities (~0.3 m/s) might be influenced appreciably by free-convection currents. In order to determine equivalent convection heat transfer coefficients in the stator end-winding region, this paper proposes the following considerations.

Since the flow characteristics has been complex in nature in the end-winding region of an aluminum rotor induction motor, several authors in [13]-[17] proposed and validated a general formula to calculate the equivalent convection heat transfer coefficient due to free and forced convection heat transfer which is expressed by:

$$h = k_1 \times \left[1 + \left(k_2 \times v \right) k_3 \right] \tag{3.37}$$

where, h is the convection heat transfer coefficient in the end region and is a function of inner air velocity v (m/s) and proportionality coefficients k_1, k_2 and k_3 that are dependent on turbulent airflow in the end region. As discussed in [13], it is a difficult task to determine a representative value of inner air speed due to the end-windings geometry. So, the rotor peripheral speed was used to estimate inner air speed. Among several models in [13]-[17],

(a) Copper rotor.

(b) Aluminum rotor.

Figure. 3.5. Induction motor. (a) Copper rotor. (b) Aluminum rotor.

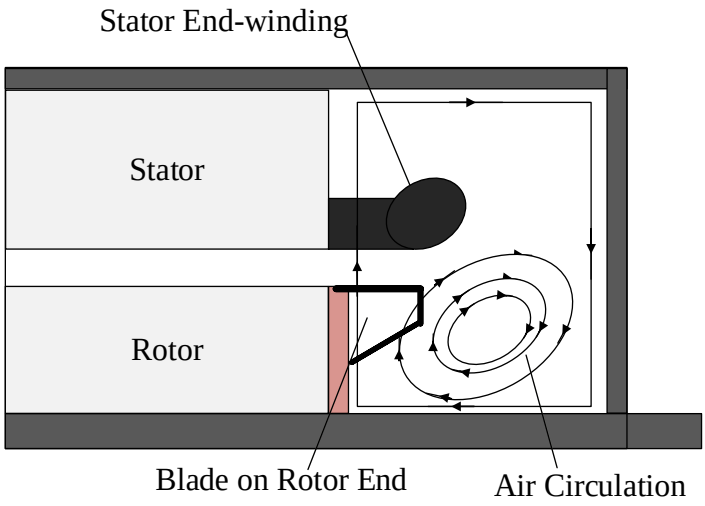

Figure. 3.6. Air circulation in the end region between Stator end-windings/rotor end-rings and endcap in an aluminum rotor induction motor.

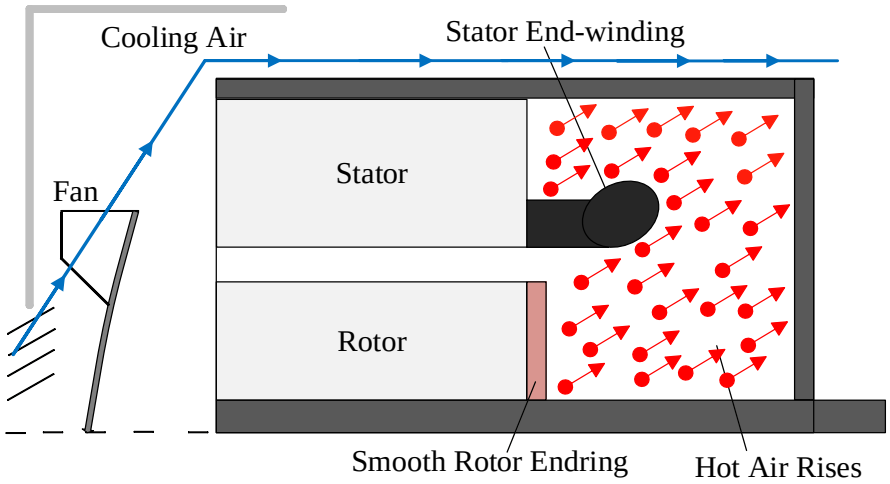

Figure. 3.7. Combined free and forced Convection in the end region between Stator end-windings/rotor end-rings and endcap in a copper rotor induction motor.

Schubert's model [16] was commonly used to calculate equivalent convection heat transfer coefficient. The expression of Schubert's model is:

$$h_{end-wdg} = 15.5 \times \left\{ 1 + \left(0.4 v_{iair} \right) 0.9 \right\} \tag{3.38}$$

$$v_{iair} = r_{rot} \omega \eta \tag{3.39}$$

where, v_{iair} is the air speed in the stator end-winding region, ω is the angular speed of the rotor and η is the end-winding fanning factor which is used to relate the magnitude of rational air velocity in the end-caps to rotor peripheral velocity. The above expression (3.39) has both free and forced convection component. In [15]-[17], the research work determines equivalent end-winding convection coefficients based on Schubert's expression and validated experimentally in case of aluminum rotor with fins. From the findings, it was also concluded that if there is no internal fan and the rotor ends of the rotor are smooth such as copper rotor, the internal air velocity will be much less, and end-winding fanning factor will be closer to zero. Hence, in this paper, due to smooth rotor geometry in a copper rotor induction motor, Schubert's expression is used with the fanning factor of close to zero in order to calculate equivalent heat transfer coefficients in the end-winding region.

Node 9, T_9: Temperature rise in the inner air

$$dT_9 = \frac{dt}{C_9} \times \left[\left\{ \left(T_{fr} - T_9 \right) \Big/ R_{12} \right\} + \left\{ \left(T_8 - T_9 \right) \Big/ R_{11} \right\} + \left\{ \left(T_1 - T_9 \right) \Big/ R_{13} \right\} \right] \tag{3.40}$$

$$R_{12} = 1 \Big/ A_{endcap} h_{inner-air} \tag{3.41}$$

where, $h_{inner\text{-}air}$ is the convection coefficient between the inner air and the motor endcap. The value of convection coefficient is necessarily the same as the value of the convection coefficient of $h_{end\text{-}wdg}$.

Node 10, T_{10}: Temperature rise in the bearing

$$dT_{10} = \frac{dt}{C_{10}} \times \left[\left\{ \left(T_{fr} - T_{10} \right) \Big/ R_{15} \right\} + \left\{ \left(T_1 - T_{10} \right) \Big/ R_{14} \right\} \right] \tag{3.42}$$

$$R_{15} = \frac{1}{2\pi \, \Delta x_{endcap} \times \kappa_{ir}} \ln \left(\frac{r_{endcap}}{r_{shaft}} \right) \tag{3.43}$$

where, Δx_{endcap} is the thickness of the endcap, κ_{ir} is the conductivity of endcap material and r_{endcap} is the radius of endcap.

Node frame, T_{frame}: Temperature rise at the frame

$$dT_{fr} = \frac{dt}{C_{fr}} \times \left[\left\{ \frac{(T_7 - T_{fr})}{R_7} \right\} + \left\{ \frac{(T_8 - T_{fr})}{(R_9)} \right\} + \left\{ \frac{(T_8 - T_{fr})}{(R_{10})} \right\} + \left\{ \frac{(T_{10} - T_{fr})}{R_{15}} \right\} + \left\{ \frac{(T_9 - T_{fr})}{R_{12}} \right\} + \left\{ \frac{(T_{fin} - T_{fr})}{R_{16}} \right\} \right] \tag{3.44}$$

$$R_{16} = \frac{\Delta x_{fins}}{A_{fins} \kappa_{ir}} \tag{3.45}$$

where, A_{fins} is the endcap area, Δx_{fin} is the height of the fins, κ_{ir} is the conductivity of fin material.

Node fin, T_{fin}: Temperature rise at the fins

$$dT_{fin} = \frac{dt}{C_{fin}} \times \left[\left\{ \frac{(T_{fr} - T_7)}{R_{16}} \right\} + \left\{ \frac{(T_{amb} - T_{fin})}{R_{17}} \right\} + \left\{ \frac{(T_{amb} - T_{fin})}{R_{18}} \right\} \right] \tag{3.46}$$

$$R_{17} = \frac{1}{\sigma \varepsilon A_{rad} \times \left\{ (T_{amb} + T_{fin}) \times (T_{amb}^2 + T_{fin}^2) \right\}} \tag{3.47}$$

where, σ is the Boltzman's constant, ε is the emissivity and A_{rad} is the radiation surface area.

$$R_{18} = \frac{1}{A_{fr} h_{fin}} \tag{3.48}$$

where, A_{fr} is motor frame area; h_{fin} is the forced convection coefficient for the motor frame to the ambient. In TEFC induction motor design the axial fins on the housing surface are built to enhance the convection heat transfer from the motor frame to the ambient. "For TEFC enclosures, the fin channels are semi-open and a special formulation can be used to calculate convection heat transfer coefficient" [23].

$$h_{fin} = \frac{\left(\rho c_p D v_{fin} \right)}{\left[4 \times L_{fin} \times \left(1 - e^{-m} \right) \right]} \tag{3.49}$$

$$m = \frac{0.1448 L_{fin}^{0.946}}{D^{1.16} \times \left\{ \kappa_{\text{fin}} / \rho c_p \nu_{fin} \right\}^{0.214}} \tag{3.50}$$

where, L_{fin} is the axial length of the fin, D is hydraulic diameter and v_{fin} is the air velocity in the fin channels [23]. Section 3.4 details the experimental setup while section 3.5 presents the authors' conclusion.

3.4 Experimental Investigation

3.4.1 Experimental Setup

The thermal analysis by using a higher order thermal model was validated through testing a 20 hp copper rotor induction motor whose specifications were identified in Table 1. Figure 8 and 9 show the experimental setup where the test motor was driven by a variable frequency drive and a dynamometer was used as a load. The motor control unit was used to control speed and torque settings on the test motor. A torque sensor was used through the coupling between the test motor and the dynamometer. Two small holes were drilled through frame on the both ends and two four-wire RTD temperature sensors were inserted into the stator end-winding coils to measure the temperature rise at the end-windings. A tape was used to hold the sensors into the coil. DAQ controller unit (model no. iNET400) was used performing RTD temperature recordings. Table 3.7 shows the specification of the RTDs.

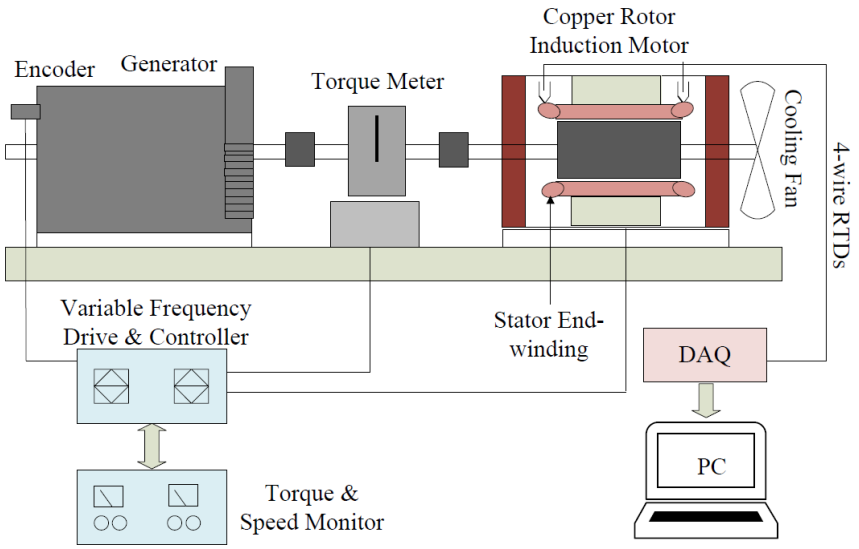

Figure 3.8. Schematic diagram of the experimental setup.

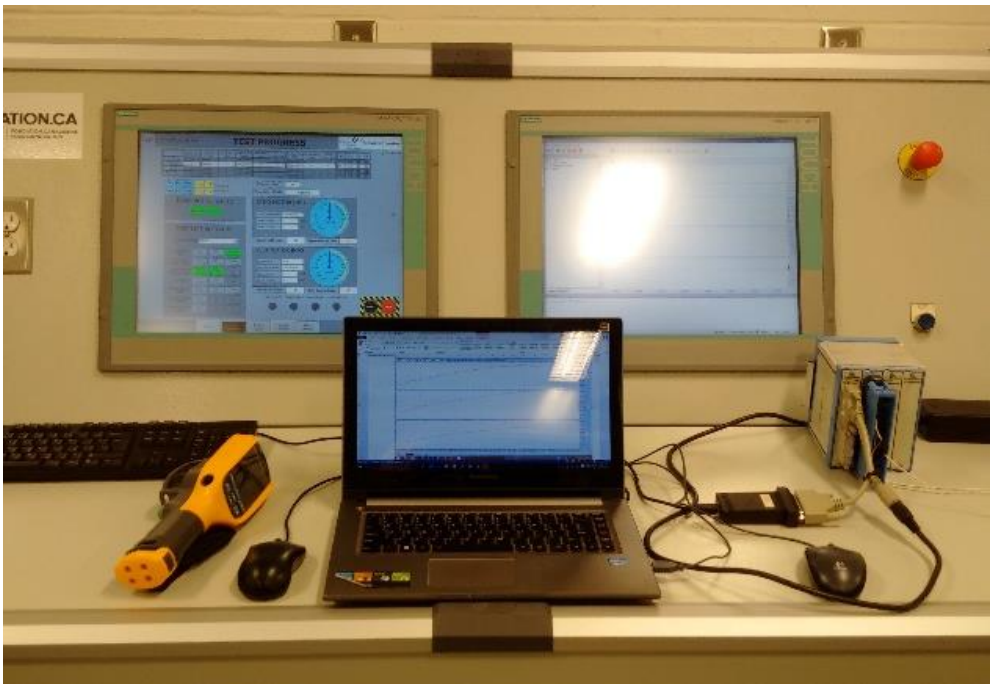

(a) Torque-speed controller.

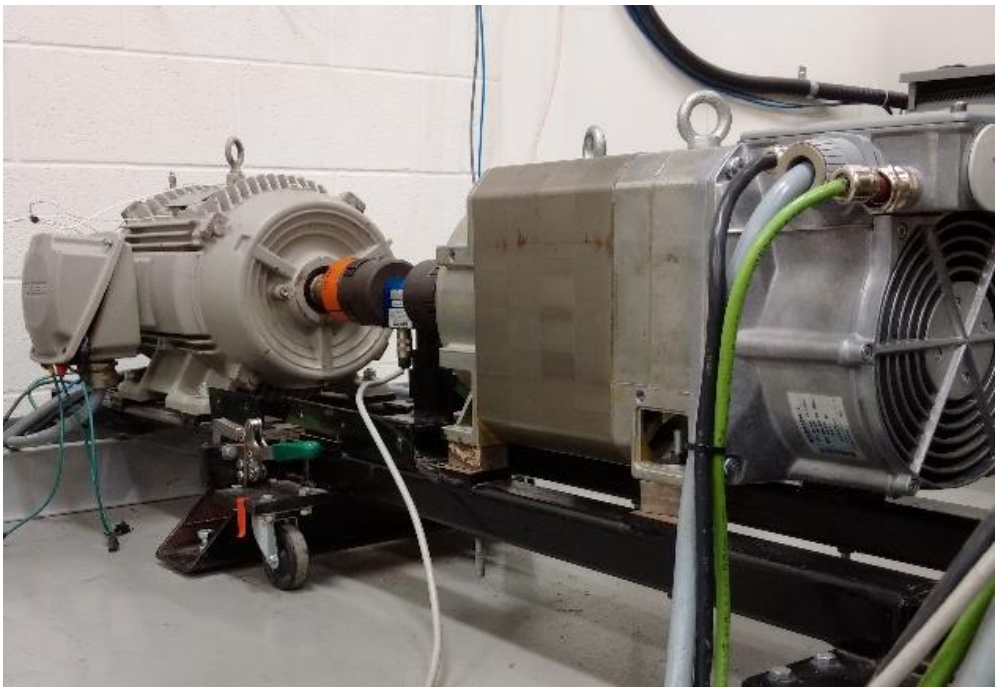

(b) CRIM test motor coupled with dyno.

Figure 3.9. Thermal experimental setup. (a) Torque-speed controller. (b) CRIM test motor.

TABLE 3.7

RESISTANCE TEMPERATURE DETECTORS (RTD) USED IN THE EXPERIMENTAL SETUP

Instrumentation	Model	Specification	Accuracy
RTD	RTD-3-F3105-72-G	Temperature: -30 to 300°C	+/- 0.06Ω at 0° C

3.4.2 Results and Analysis

This section discusses detailed analysis of the predicted stator winding temperature from a proposed higher order thermal and compares with conventionally used 1st order thermal model for overload thermal protection in the industries. The thermal analysis also focuses on cooling effects differences in the end-region due to the non-existent of the rotor fins compared to aluminum rotor which further perfecting the higher thermal model which needs to be included into the model algorithm development for thermal overload protection purposes.

3.4.2.1 The proposed higher order LPTN model predicted temperature estimation and validated with experiments.

Thermal experiments were performed for three different loading of 70 Nm, 50 Nm and 30 Nm which are 88%, 63% and 38 % of full load at 1,500 rpm speed. Figure 10 shows the

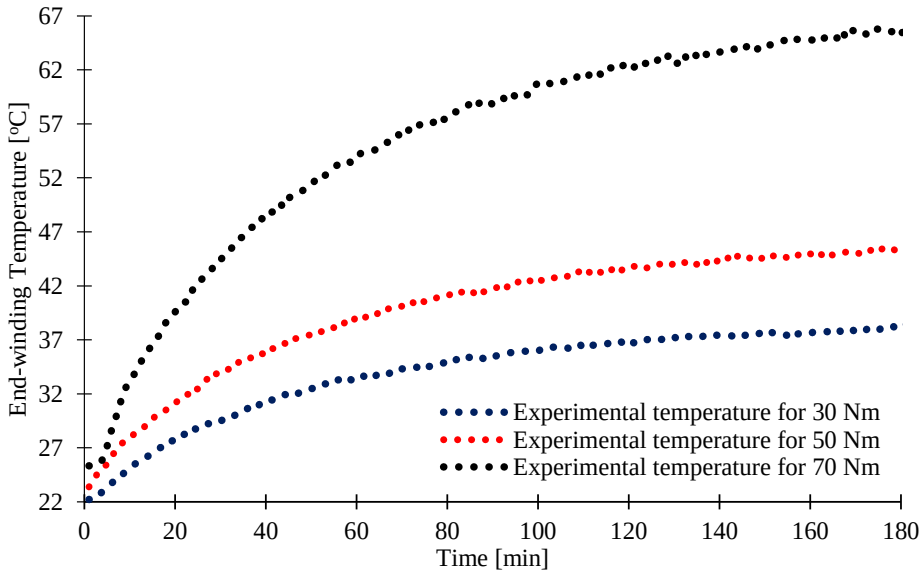

Figure 3.10. Experimental results of stator end-winding temperature rise for different loading at 1,500 rpm speed.

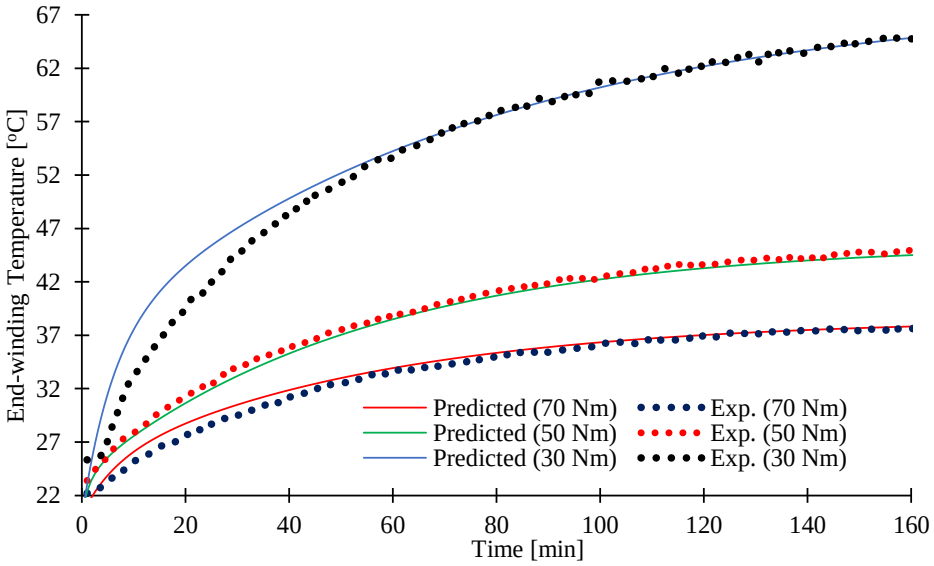

Figure 3.11. Comparison of experimental and predicted results of stator end-winding temperature rise for different loading at 1,500 rpm speed.

stator end-winding temperature for the respective loading experiments with TEFC normal fan cooling design where the fan externally blows the air over the motor frame. The proposed model considers all heat sources that are caused by the losses and through detailed analytical solution in section 3.4, the predicted temperature rise in the motor were investigated. Figure 3.11 compared the model predicted results with experimental results which are well in agreement.

3.4.2.2 Analysis of higher order thermal model results compared to 1st order thermal model in industry applications

As explained in the section III, the industry adopts the simplified 1st order thermal model to monitor stator winding temperature for thermal protection purposes. Hence, in Figure 3.12, 3.13 and 3.14, the predicted results of 1st order model are determined under varying loading conditions and compared with the results of higher order model. The results clearly demonstrate that the proposed model produces greatly accurate temperature prediction over 1st order model. The temperature prediction error in the 1st order model is 25^{0}C for higher loading and 10^{0}C lower loading conditions as shown in Figure 3.14 and 3.15. This error is too high to ensure smooth motor operation in the facilities and will cause the tripping of

the motor more frequently. In addition, as the temperature prediction by the 1st order model is different under varying load conditions, the protection device has to adjust these changes which is problematic in the operation. On the other hand, the higher order model has only 2-3^{0}C error including instrumental error which demonstrates the agreement very well with experimental results. This comparison also demonstrates that thermal behavior of the motor is a combined effect from all different losses, heat transfer from different components, thermodynamic behavior and cooling effects in general. In the 1st order model, the motor was considered as a homogeneous body which is a very impractical assumption as the motor is made up of different materials and they do exhibit different thermal properties. It is critically important to consider actual heat dynamics in the motor as it is considered in the proposed model. Heating in the motor greatly varies with loading conditions caused by higher copper losses, whereas core loss and frictional losses are relatively constant. Hence, the higher order thermal model algorithm based on motor operating information is much suited to thermal overload protection. In addition, there are all different locations in the motor components, specifically the rotor, it is the greatest challenge and expensive to install

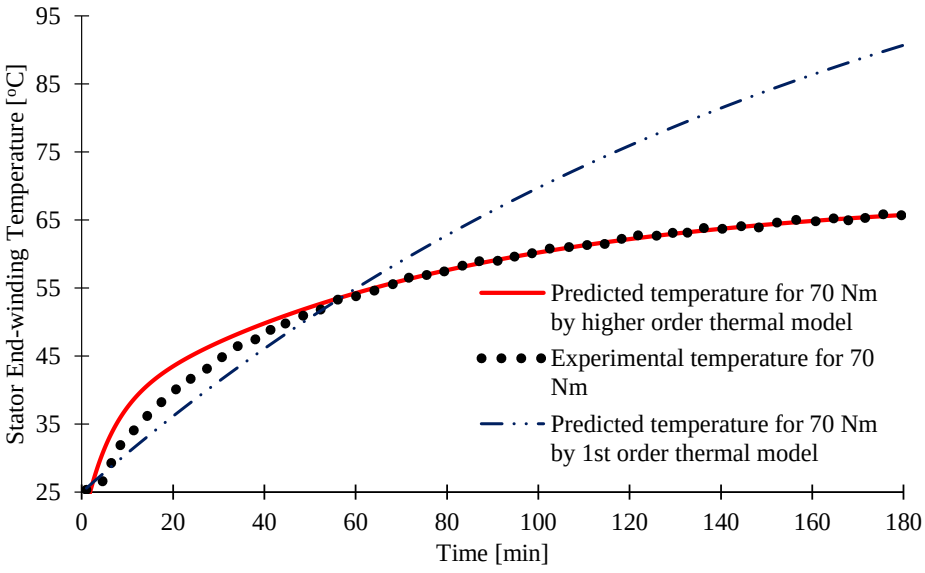

Figure 3.12. Comparison of experimental and predicted results by 1st order model and higher order model for 70 Nm loading at 1,500 rpm speed.

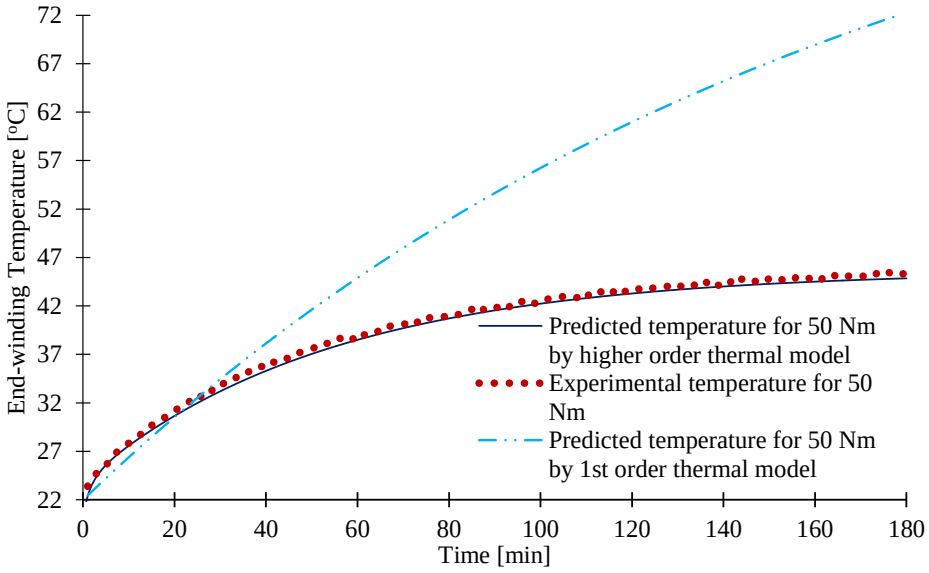

Figure 3.13. Comparison of experimental and predicted results by 1st order model and higher order model for 50 Nm loading at 1,500 rpm speed.

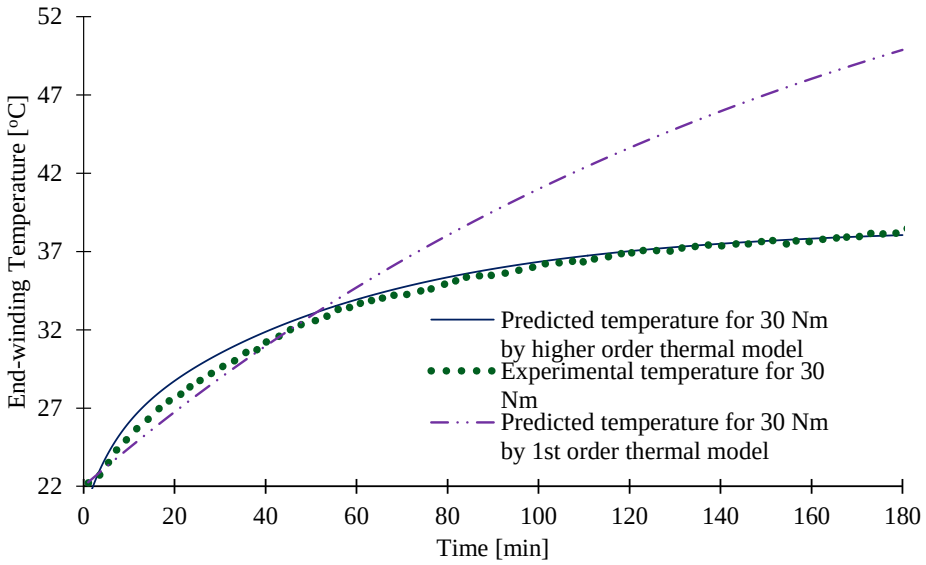

Figure 3.14. Comparison of experimental and predicted results by 1st order model and higher order model for 30 Nm loading at 1,500 rpm speed.

any temperature measuring device to monitor the rotor temperature. The proposed thermal model provides the perfect solution to this by estimating temperature rise at any location in the motor components. Figure 3.15 shows the temperature rise at the rotor, air gap, stator winding, core and the frame which is actual and complete heat dynamics representation from the model and it is only possible from a higher order model that better protects the motor by knowing the temperature at various locations.

3.4.2.3 Heating time constant

From the experimental results, heating time constants are calculated as presented in Table VIII to analyze the thermal behavior for thermal protection purposes. By definition, heating time constant describes the measure of time taken by the motor to reach its final steady state temperature rise. So, the higher heating time constant the longer it takes to reach the steady state temperature. On the other hand, the higher the time constant, it represents the higher heat generation in the machine due to higher losses or poorer ventilation in the machine.

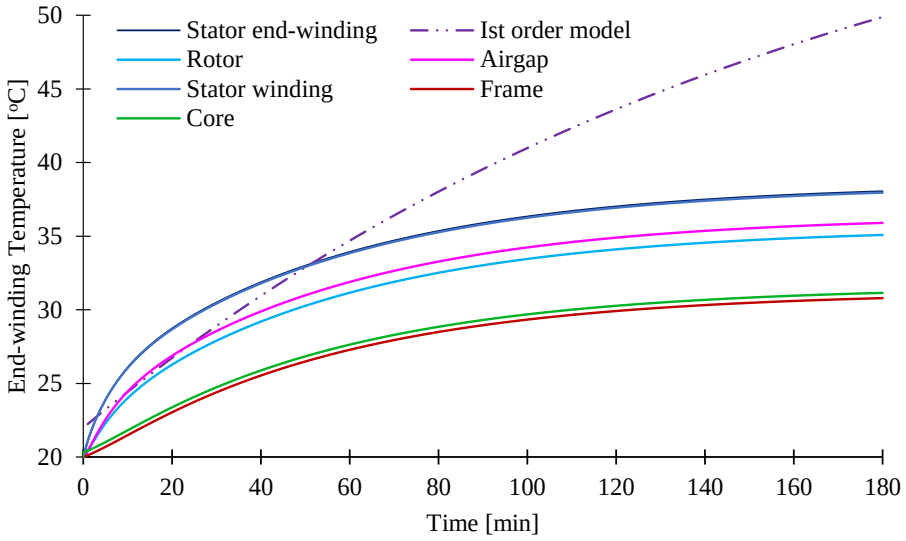

Figure 3.15. Higher order model predicted results at different location for 30 Nm loading at 1,500 rpm speed.

TABLE 3.8

HEATING TIME CONSTANT FOR DIFFERENT LOADING EXPERIMENTS

Loading conditions	38%	63%	88%
Time constants	0.45	0.46	0.53
Variable speed	300 rpm	900 rpm	1,500 rpm
Time constants	0.80	0.60	0.53

Figure 3.16 shows the thermal time constant for different loading conditions. This demonstrates that compared to the time constant at lower loading to that at higher loading, the rotational losses has relatively less effect on it and the changes are due to primarily higher copper losses in the motor which can be calculated by monitoring the phase currents

thus this can be adjusted by monitoring the loading conditions of the motor. Figure 3.17 shows higher heating time constant at lower rpm which explains that with TEFC design, the motor will suffer from proper ventilation because lower rpm makes the fan on the shaft in the cowling less efficient to remove the heat from the motor. Hence, cooling status can be monitored by knowing the rpm of the motor in any application to protect the motor from overheating as well. Figure 3.18 shows the temperature rise difference in the stator end-windings due to lower TEFC fan efficiency at different shaft speed.

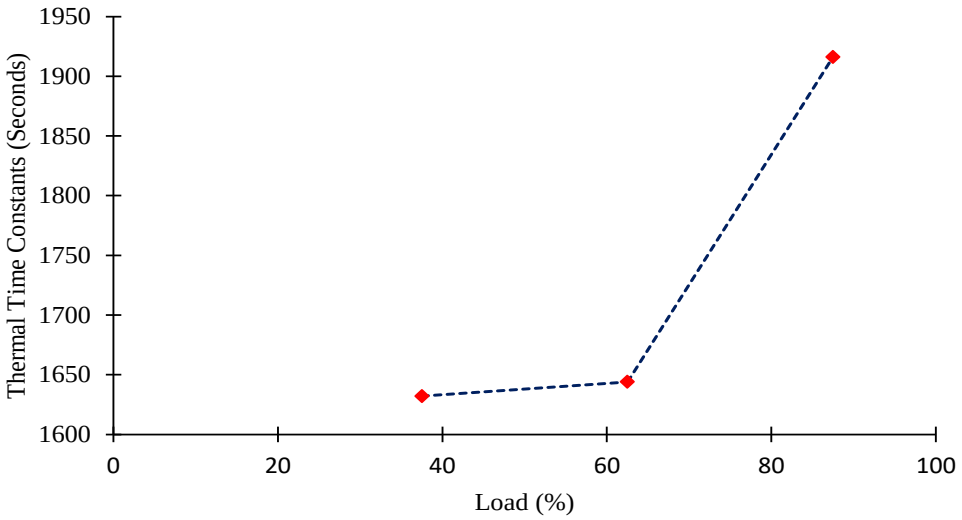

Figure 3.16. Thermal heating constants for different loading of 30 Nm (38%), 50 Nm (63%) and 70 Nm (88%).

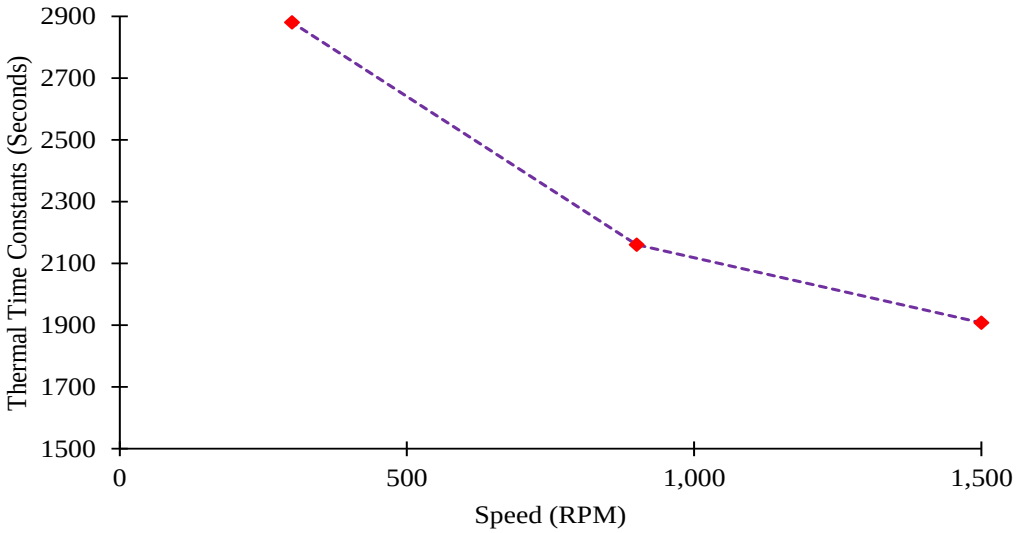

Figure 3.17. Thermal heating constants at different speed.

3.4.2.4 Analysis of cooling effects of stator end-winding on fan side and drive side

Another objective in the paper is to determine the differences in cooling effects in the end region of the stator winding due to smooth rotor geometry of the copper rotor induction motor compared to aluminum rotor motor as explained earlier. In order to quantify such cooling differences, a small fan was fabricated and installed on the shaft (fan side) inside the motor that mimics the aluminum rotor fins.

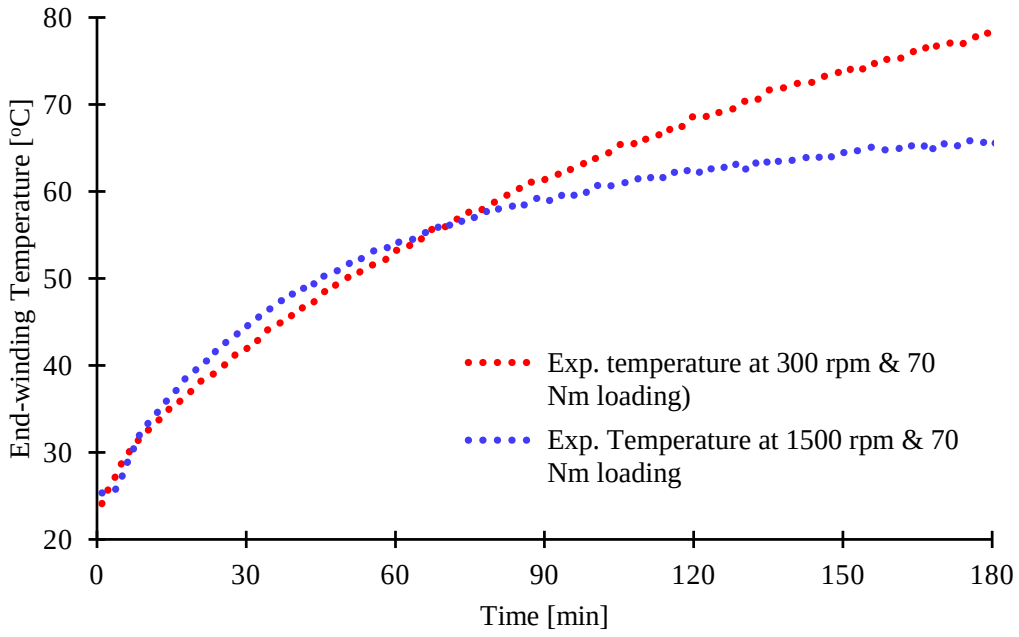

Figure 3.18. Stator end-winding temperature for different speed.

Thermal experiments were performed for 70 Nm loading at 1,500 rpm and temperature rise with small fan inside motor is compared with the temperature rise on the drive side. During this experiment, the original TEFC fan was removed to determine accurately the difference between the temperature rises on fan side and drive side as shown in the Figure 3.19. This comparison clearly demonstrates that after 2-hour of operation with 70 Nm loading, the temperature rise difference between fan side and drive side is around 10^0C. This difference is significant and hence, cooling effects due to smooth rotor geometry is a critical factor in accurately estimating the temperature rise at the stator end-winding to ensure thermal protection from overheating of a copper rotor induction motor which has not been researched in any previous work. This result ensures proper heat dynamics in the end region in estimating stator winding temperature accurately.

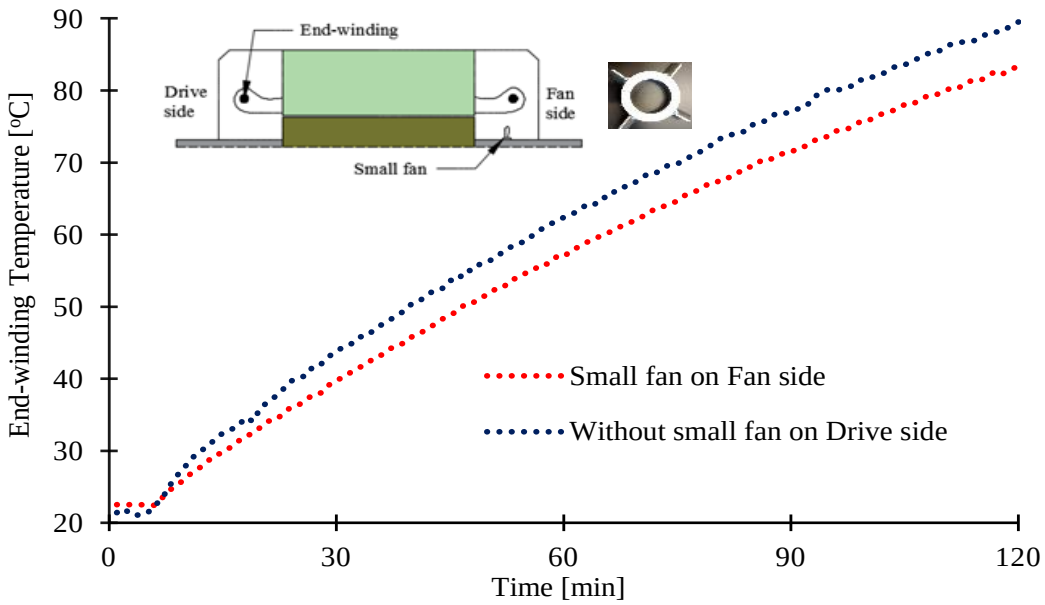

Figure. 3.19. Comparison of stator end-winding temperature rise for 70 Nm loading at 1,500 rpm speed with and without small fan.

3.5 Conclusion

In this paper, a higher order thermal network model has been proposed based on the detailed heat and thermodynamic considerations which are critical to accurately predict stator winding temperature to ensure proper overload thermal protection in any industry application. The analytical solution and thermal parameter considerations are useful to develop the thermal model algorithm to be used for thermal protection purposes in the industries. The proposed thermal model has been validated from the experiments using a 20 hp copper rotor induction motor under varying load conditions. The key objectives that are met in this work are: (1) proposed higher order thermal model and predicted stator winding temperature accurately with only 2-3^{o}C error which is critical for thermal overload protection. (2) Demonstrated a commonly used 1st order thermal model stator winding temperature estimation that has as high as 25^{0}C error. (3) Solved higher order thermal model for induction motor with die cast copper rotor with non-existent of the fins on its short circuit rings to predict stator winding temperature accurately. (4) Validated model results through experimentation.

3.6 References

[1] Z. Gao, "Sensorless Stator Winding Temperature Estimation for Induction Machines," in School of Electrical and Computer Engineering. PhD dissertation, Georgia Institute of Technology, Atlanta, 2006.

[2] B.Venkataraman, B.Godsey, W. Premerlani, E.Shulman, M.Thakur, R.Midence, "Fundamentals of a Motor Thermal Model and its Applications in Motor Protection", *58th Annual Conference for Protective Relay Engineers*, 2005.

[3] Motor Reliability Working Group, "Report Of Large Motor Reliability Survey Of Industrial And Commercial Installations, Part I". IEEE Trans. Ind. Appl., vol. IA-21, no. 4, pp. 853-864, July/Aug. 1985.

[4] P. O'Donnell, "Report of large motor reliability survey of industrial and commercial installations: Part I," IEEE Trans. Ind. Appl., vol. IA-21, no. 4, pp. 853–864, Jul. 1985.

[5] P. O'Donnell, "Report of large motor reliability survey of industrial and commercial installations: Part II," IEEE Trans. Ind. Appl., vol. IA-21, no. 4, pp. 865–872, Jul. 1985.

[6] P. F. Albrecht, J. C. Appiarius, and D. K. Sharma, "Assessment of reliability of motors in utility applications—Updated," IEEE Trans. Energy Convers., vol. EC-1, no. 1, pp. 39–46, Mar. 1986.

[7] R. M. Tallam, S. B. Lee, G. C. Stone, G. B. Kilman, J. Yoo and T.G. Habetler "A Survey of Methods for Detection of Stator-Related Faults in Induction Machines" IEEE Transactions on Industry Applications, volume 43, no 4, July/August 2007.

[8] P. Zhang, Y. Du and T. G. Habetler, "A Transfer-Function-Based Thermal Model Reduction Study for Induction Machine Thermal Overload Protective Relays" *IEEE Transactions on Industry Applications,* volume 46, No. 5, 2010.

[9] Information Guide for General Purpose Industrial AC Small and Medium Squirrel-Cage Induction Motor Standards, NEMA Standard MG1-2003, August 2003.

[10] "IEEE Guide for the Presentation of Thermal Limit Curves for Squirrel Cage Induction Machines", *Electric Machinery Committee of the IEEE Power Engineering Society*, 2008.

[11] D.T. Peters, J.G. Cowie, E.F. Brush, Jr. and D.J. Van Son, "Copper in the Squirrel Cage for Improved Motor Performance," International Electric Machines and Drives Conference, June, 2003.

[12] E.F. Brush, J.G. Cowie, D.T Peters and D.J. Van Son, "Die-Cast Copper Motor Rotors; Motor Test Results, Copper Compared to Aluminum", Energy Efficiency in Motor Driven Systems, Eds: F. Parasiliti & P. Bertoldi, Published by Springer, 2003, p 136 to 143.

[13] A. Boglietti and A. Cavagnino, "Analysis of the end-winding cooling effects in TEFC induction motors," *IEEE Transactions on Industry Applications*, volume 43,issue 5, pp. 1214-1222, 2007.

[14] C. Micallef, S. J. Pickering, K. Simmons, and K. Bradley, "Improvements in air flow in the end region of a large totally enclosed fan cooled induction motor," *Proc. of IEMDC'05 IEEE International Electric Machines and Drives Conference*, San Antonio, May 2005.

[15] A. Boglietti, A. Cavagnino, D. Staton, M. Popescu, C. Cossar, and M.I. McGilp, "End space heat transfer coefficient determination for different induction motor enclosure types", *IEEE Trans. on Industry Applications*, vol. 45, No. 3, May/June 2009, pp. 929-937

[16] E. Schubert, "Heat Transfer Coefficients at End Windings and Bearing Covers of Enclosed Asynchronous Machines," *Elektrie*, vol. 22, April 1968. pp160-162. (Translation ERA/IB 2846).

[17] A. Boglietti, A. Cavagnino, D. Staton, and M. Popescu, " Impact of different end region cooling arrangements on endwinding heat transfer coefficients in electric motors," *Proc. IEEE Conf. on Industrial Electronics*, 978-1-4244-4649-0/09.

[18] C. Micallef, S. J. Pickering, K. A. Simmons, and K. J. Bradley, "An Alternative Cooling Arrangement for the End Region of a Totally Enclosed Fan Cooled (TEFC) Induction Motor,*" 4th IET Conference on Power Electronics Machines and Drives*, pp. 309-309, (2008).

[19] J.P., Holman.''Heat Transfer" 9th ed., McGraw-Hill, 2002, pp. 640-647.

[20] A.Boglietti, A. Cavagnino, M. Lazzari, and M. Pastorelli, "A simplified thermal model for variable speed self cooled industrial induction motor," IEEE Transactions on Industry Applications, volume.39, No.4, July/August 2003, pp. 945-952.

[21] J. Pyrhonen, T. Jokinen and V. Hrabovcova, "Design of Rotating Electric Machines", 2008 John Wiley & Sons, Ltd. ISBN: 978-0-470-69516-6.

[22] F. Ahmed, E. Ghosh, and N.C.Kar, " Transient Thermal Analysis of a Copper Rotor Induction Motor using a Lumped Parameter Temperature Network Model," in IEEE Transportation Electrification Conference and Expo (ITEC), June 2016.

[23] D. A. Staton and A. Cavagnino, "Convection Heat Transfer and Flow Calculations Suitable for Electric Machines Thermal Models, Member, IEEE Transactions on Industrial Electronics, vol. 55, no. 10, October 2008.

CHAPTER 4

CFD AND LPTN HYBRID TECHNIQUE TO DETERMINE CONVECTION COEFFICIENT IN END-WINDING OF TEFC INDUCTION MOTOR WITH COPPER ROTOR

4.1 Introduction

The stator windings generally reach the highest temperature compared to any other parts in an electric motor while it is in operation [1]. Consequently, 35-40% motor failure are related to stator winding insulation breakdown due to overheating of the winding [2]. Considering such alarming statistics of motor failure, it is critical to monitor the stator winding temperature continuously and accurately to ensure that the permissible thermal limit is not exceeded and prevents a major breakdown or failure of the winding insulation. Many different techniques are used in the modern industries to protect thermal overload conditions. One of the techniques is embedding temperature measuring devices such as RTDs (Resistance Temperature Detectors) or thermocouples at the stator winding locations and measuring temperature directly to determine thermal cut-off limit of the motor. However, these techniques do not provide enough protection due to the non-uniform heating of the motor components including windings. In addition, these techniques are complex in installation and not cost-effective at all for small to medium scale mains fed induction machines [3]. Due to higher cost and complexity of installation of these embedded sensors, the conventional approach in the industries today is to use thermal overload protection devices to monitor the stator winding temperature [3]. These thermal overload protection devices are generally operated based on thermal models and in this approach a simplified first order thermal model is developed using nameplate information of the motor. Hence, this method is too simple and heat dynamics in the motor is ignored to predict stator winding temperature accurately. On the other hand, two different thermal modelling techniques that are used today to determine stator winding temperature are analytical LPTN and numerical modelling. LPTN is widely and commonly used in the industry to calculate winding temperature as it is much faster and involves only use of heat transfer empirical relationships. The numerical methods are very effective when complex

modelling of heat and air flow conditions exist. However, numerical technique is less attractive over LPTN due to its longer computational time and related costs.

While LPTN modelling is becoming an increasingly reliable technique to predict stator winding temperature accurately, complex nature of heat and air flow in the end-winding region makes the LPTN solution task quite challenging. Such heat and air circulation characteristics in the end- region vary due to several factors such as shape and length of stator end-winding, rotor geometry and end space clearance. These factors are also directly related to a critical thermal parameter in LPTN model which is convection heat transfer coefficient around end-winding. In the past, research has been done to determine convection coefficient in the end-winding region for a Totally Enclosed Fan-cooled (TEFC) induction motor with aluminum rotor that has fins and blades on its end-rings as shown in Figure 4.1 and the fins enhance cooling effects due to air circulation around end-winding. Several authors in [4]-[11] proposed and validated a general formula to calculate the equivaalent convection heat

(a) (b) (c)

Figure 4.1. TEFC induction motor. (a) Stator. (b) Copper rotor. (c) Aluminum rotor.

transfer coefficient due to free and forced convection heat transfer in the end-region which is expressed as:

$$h = k_1 \times \left[1 + \left(k_2 v\right)^{k_3}\right] \tag{4.1}$$

where, h is the convection heat transfer coefficient in the end region and is a function of inner air velocity v (m/s) and proportionality coefficients k_1, k_2 and k_3 that are dependent on turbulent airflow in the end-region. The above expression has both natural and forced convection coefficient components and varies as a function of inner air velocity. As

discussed in [4], it is a challenging task to determine a representative value of inner air speed due to the end-windings shape and geometry. So, the authors in the past used rotor peripheral speed to estimate inner air speed which is expressed as:

$$v_{iair} = r_{rot}\omega\eta \tag{4.2}$$

where, v_{iair} is the air speed in the stator end-winding region, ω is the angular speed of the rotor and η is the end-winding fanning factor which is used to relate the magnitude of rotational air velocity in the end-region to rotor peripheral velocity. Figure 4.2 shows the published correlations for the equivalent convection heat transfer coefficients as a function of rotor peripheral speed. Equivalent convection coefficient consists of natural and forced convection coefficients. In Figure 4.2 the values of complete natural convection coefficients lie on the y-axis at the rotor velocity of zero and equivalent convection coefficient varies with the increase of rotor velocity. First, all these models developed by the authors in [4]-[11] are related to induction motor with aluminum rotor that has fins on its end-rings. However, in this study the chosen electric motor that has smooth rotor ends such as CRIM will experience different pattern of air circulation in the end-region and this will result the differences in convection heat transfer between end-winding and inner air and then to the motor casing. Second, due to the differences in rotor geometry air velocity estimation in the end-winding using (2) will not be applicable for CRIM. Hence, determination of convection coefficient for CRIM as well as any other motor type that has smooth rotor ends is still a problem that compromises accurate prediction of stator winding temperature in LPTN thermal modelling.

This paper proposes a CFD technique along-with a simplified LPTN modelling to determine convection heat transfer coefficient in the end-winding. First, a simplified LPTN model and DC thermal tests will determine natural convection coefficient for end-winding while rotor is still. Second, CFD technique will determine air flow characteristics in the end-winding region at different speeds. Third, based on air flow pattern, a correlation for forced and natural convection coefficients will be determined using empirical heat transfer equations. Finally, calculated natural and forced convection coefficients will be compared

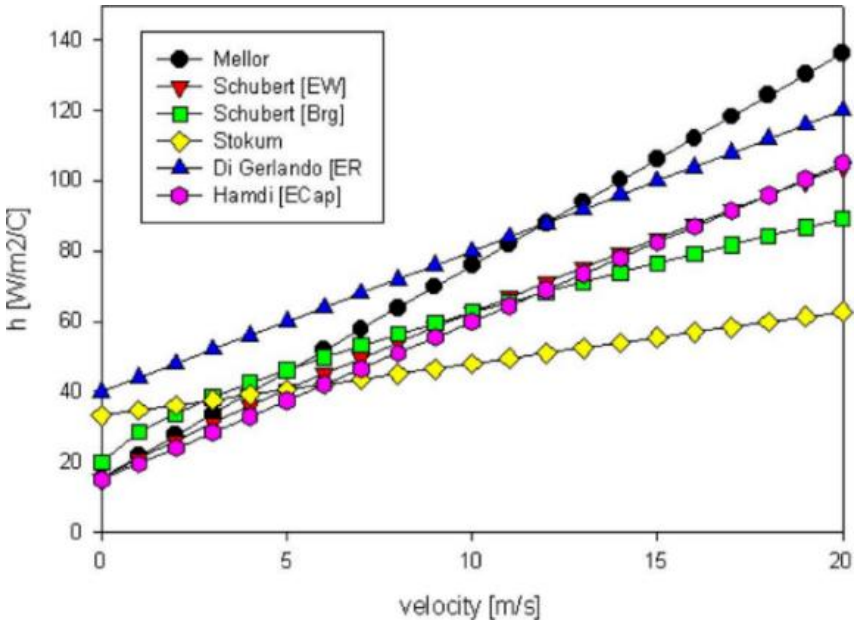

Figure. 4.2. Published correlations for the equivalent heat-exchange coefficients in the end-regions for TEFC induction motors [4]-[11].

with the published results for induction motor as shown in Figure 4.2 and will discuss the importance of these findings for the Copper Rotor Induction Motor (CRIM) or any other type of motor that has rotor geometry with smooth rotor ends.

4.2 Advances in copper rotor technology and End-winding cooling challenges

The use of copper in place of aluminum in an induction motor can lead to significant benefits [12] such as higher efficiency, its higher electrical conductivity, lower operating temperature rise due to lower resistive losses, extended life expectancy, reduction of the overall size and weight while maintaining the higher efficiency and low cost due to smaller machine. In comparison for a 50-kW aluminum rotor induction motor, losses were 4% higher and power-torque densities 5% lower than the equivalent copper rotor motor [12]. Considering the advancement of the copper rotor die casting technology as well as performance advantage, around 2 million copper die-cast units are already in use worldwide [13]. The benefits of better efficiency, compact and smaller machine at reduced cost have made copper rotor motor also a suitable choice over permanent magnet motor in traction motor applications.

Despite these advantages and mass production of copper rotor motor, they cannot have fins or blades due to manufacturing limitations. As a result, non-existent of the fins or blades in a TEFC design, the overall cooling is affected and consequently higher cooling is required to limit the temperature rise at the stator end-winding that does not exceed insulation breakdown temperature [14]. On the other hand, accurate prediction of stator winding temperature using LPTN thermal model requires accurate calculation of convection coefficient in the end-winding region.

4.3 Determination of Heat Transfer Coefficients

4.3.1 Natural Convection Coefficients from End-winding

A simplified LPTN model in Figure 4.3 shows how the heat transfer takes place from the end-winding region to the motor casing. Radiation heat transfer from the end-winding takes place through thermal resistance R_2, natural convection heat transfer takes place through thermal resistance R_3 and forced convection heat transfer takes place though thermal resistance from end-winding to the inner air, R_4 and then through resistance from inner air to the motor casing, R_5. In order to simplify the thermal resistance calculations, DC thermal tests have been carried out by supplying DC currents through the stator windings only.

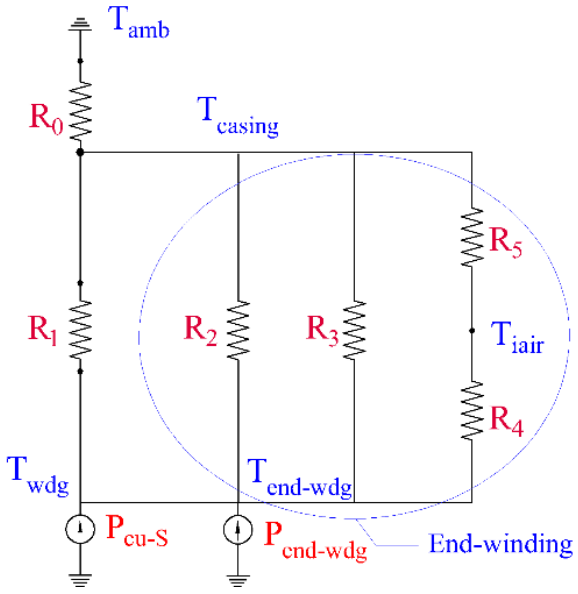

Figure. 4.3. A simplified Lumped Parameter model for end-winding.

TABLE 4.1

SIMPLIFIED LUMPED PARAMETER THERMAL NETWORK (LPTN) MODEL PARAMETER

Thermal Parameter	Description of Model Parameters
$P_{cu\text{-}S}$	Stator copper losses (conductors in the slots)
$P_{end\text{-}wdg}$	Stator end-winding losses
R_0	Thermal resistance due to natural convection and radiation between casing and ambient
R_1	Equivalent thermal resistance due to conduction between stator winding in the slots and the motor casing
R_2	Thermal resistance due to radiation from end-winding to motor casing
R_3	Thermal resistance due to natural convection between end-winding to motor casing
R_4	Thermal resistance due to forced convection between end-winding and inner air
R_5	Thermal resistance due to forced convection between inner air to motor casing

In DC thermal tests, only copper losses at the stator exists which simplifies the calculation. As the rotor is still and does not have any rotation, thermal resistances, R_4 and R_5 for forced convection between the end-winding and the casing are cancelled out. During DC thermal tests, temperatures at stator winding, inner air in the end-region and casing were measured using RTDs thermal sensors and these temperature readings are used in solving this LPTN to determine natural convection coefficients in the end-region of the motor. This natural convection takes place in the end-winding region only due to non-existent of air circultion during DC tests. Figure 4.4 shows the temperature of the end-winding and inner air. The following sections describe the equations to calculate different thermal resistances from this simplified thermal model.

Thermal resistance, R_0 represents the resistance due to both natural convection and radiation between the casing and ambient which can be calculated from the following expression:

$$R_0 = {}^{\Delta T_{ca}\sin g}\Big/\left(P_{cu-S} + P_{end-wdg}\right) \tag{4.3}$$

Thermal resistance, R_1 represnts the resistance due to conduction between stator winding and the casing which can be calculated from the following expression:

$$R_1 = \left(T_{winding} - T_{ca}\sin g\right) \Big/ P_{cu-S} \tag{4.4}$$

Thermal resistance, R_2 represnts the resistance due to radiation heat trasnfer between stator end-winding and the casing. Thermal resistance, R_3 represnts the resistance due to natural convection between stator end-winding and the casing. Both resitances are connected in parallel and this can be calculated from the following expressions:

$$1 \Big/ \left(1/R_1 + 1/R_2\right) = \left(T_{winding} - T_{ca}\sin g\right) \Big/ P_{end-wdg} \tag{4.5}$$

$$1/R_2 = \sigma\varepsilon A_{end-wdg} \times \left(T_{end-wdg} + T_{ca}\sin g\right) \times \left(T^2_{end-wdg} + T^2_{ca}\sin g\right) \tag{4.6}$$

In order to calculate convection coefficient due to natural convection from the end-winding (7) can be used:

$$R_3 = 1 \Big/ h_{end-wdg} A_{end-wdg} \tag{4.7}$$

where, $h_{end\text{-}wdg}$ is the convection heat transfer coefficient and $A_{end\text{-}wdg}$ is the endcap area.

Table 4.2 shows equivalent circuit parameters for the test motor. Table 4.3 shows all the physical dimensions of the motor that are used in thermal resistance calculations. In estimating the stator end-winding copper losses and its impact on generating heat, it is important to know the length of the end windings with respect to the total length of

windings for each phase. The joule losses causing end winding heating will be proportional

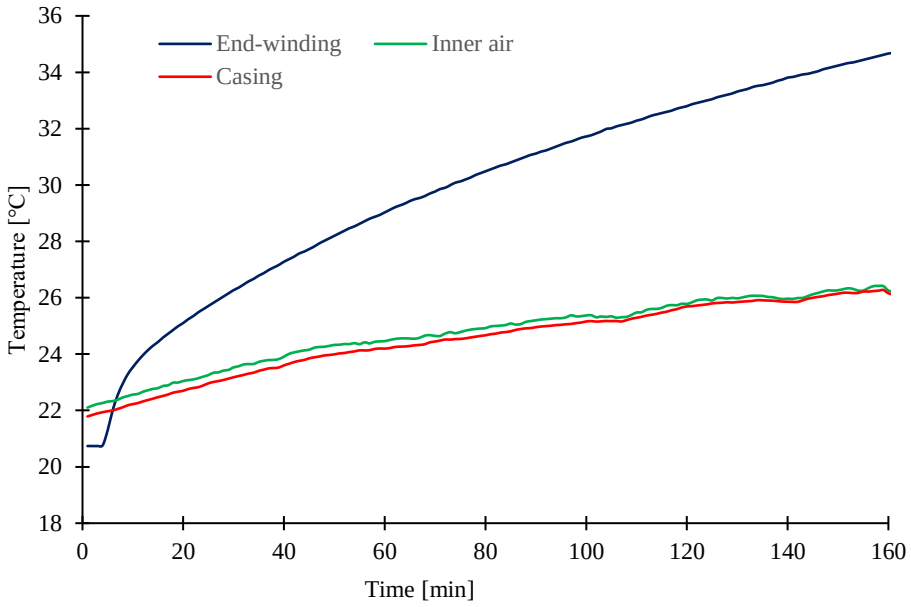

Figure 4.4. Measured temperatures for end-winding and inner air in the end-region.

to the total joule losses caused by the whole length of the windings and is simplified as:

$$P_{end-wdg} = P_{cu-total} \times \left(L_{end-wdg} / L_S \right) \tag{4.8}$$

where, $L_{end\text{-}wdg}$ is the stator end-winding length, L_S is the total stator winding length.

Table 4.4 shows all the calculated winding losses from DC tests and Table 4.5 shows calculated results of the thermal resistances from the LPTN model. From these thermal resistances natural convection coefficient in the end-winding region was calculated using (7) which is the only convection coefficient as the rotor is not rotating during DC thermal tests.

The following sections will determine the forced convection coefficients while the motor is driven at different speed conditions. First, CFD technique will be used to determine air flow characteristics and air velocity. Based on air flow pattern, empirical relationships will be used to calculate forced convection coefficients.

TABLE 4.2

COPPER ROTOR INDUCTION TEST MOTOR DATA

Test Motor Nameplate Data		Equivalent Circuit Parameters	
Parameter	Values	Parameter	Values (ohm)
Rated power	14.92 kW	R_s	0.36
Rated voltage	208/460 V	R_R	0.12
Rated current	50.0/25 A	X_{ls}	1.71
Rated speed	1,800 rpm	X_{lr}	1.71
Insulation class	F	X_m	28.20

TABLE 4.3

KEY PHYSICAL DIMENSION DATA OF THE TEST MOTOR

Motor components	Values (meter)	Motor components	Values (meter)
Stator outer diameter	0.215	Shaft length (rotor)	0.228
Stator inner diameter	0.150	Shaft length from rotor end to the bearing	0.100
End-winding outer diameter	0.220		
End-winding inner diameter	0.190	Air thickness between rotor and endcap	0.036
End-winding axial length	0.070	Rotor yoke inner radius	0.098
Rotor length	0.228	Rotor yoke outer radius	0.107
Rotor outer diameter	0.154	Frame fin length	0.254
Shaft diameter	0.052	Frame fin width	0.007
Airgap length	0.0036	Rotor lamination thickness	0.0387
Frame length	0.315	Air thickness between rotor and endcap	0.036

TABLE 4.4

NO LOAD TEST RESULTS FOR CRIM

Loading	$P_{cu\text{-}total}$ (Watt)	$L_{end\text{-}wdg}$ (m)	L_S (m)	$P_{cu\text{-}S}$ (Watt)	$P_{end\text{-}wdg}$ (Watt)
No load	127	0.07	0.298	97	30

TABLE 4. 5

NO LOAD TEST RESULTS FOR CRIM

R_0 (°C/W)	R_1 (°C/W)	R_2 (°C/W)	R_3 (°C/W)	Equivalent of R_2 and R_3 (°C/W)	Natural Convection coefficient h (W/m^2°C)
0.041	0.036	5.74	0.116	0.118	15.08

4.3.2 Determination of Air Flow Characteristics in the Stator End-winding Region using Computational Fluid Dynamic (CFD) technique

CFD is used to determine air flow characteristics and it is a tool (i,e. ANSYS Fluent) that solves numerically complete Navier-Stokes equations along-with turbulence equations. For the CFD investigation, standard k-ϵ turbulence model is used. In the electric motor, two different domains are created in this exercise, one is rotating and the other is stationary. Multiple (rotating) Reference Frame technique in steady state analysis is used. The CRIM construction in Figure 5 shows all the major motor parts including end-winding which is considered in this study. The rotor geometry shows smooth rotor ends and no fins and blades on its end-rings. Figure 6 shows two CFD models, one with completely smooth rotor ends and one with a small fin extension to demonstrate air circulations in the end-region. Due to symmetry around the shaft axis of the motor, 2D model of the end-winding is primarily considered for this study. In both models, stator winding is created as solid body cross section with 0% porosity. Rotor and shaft axis is identified as rotational axis and stator core, stator end-widning, casing and endcap are considered as stationary walls. Fluid domain in different color represents a separate body from the winding, rotor, stator shaft and casing walls.

Figure 4.6. CFD models for simulation with (a) smooth rotor end (b) small fin extensions

In the boundary condition, shaft axis and rotor axis were set as rotational reference at the speed of 1,200, 600 and 200 rpm and stator and casing wall were set as stationary wall. Steady state analysis was performed and from the simulation results, Figure 4.7, 4.8, and 4.9 show the air circulation in the end-winding region. In Figure 7 the air flow at 1,200 rpm rotor speed spreaded more outward towards the motor endcap compared to that in Figure 4.9 at 600 and 200 rpm. There are two circulation loops produced in the region

where the loop closer to the stator core has greater air circulation compared to the one close

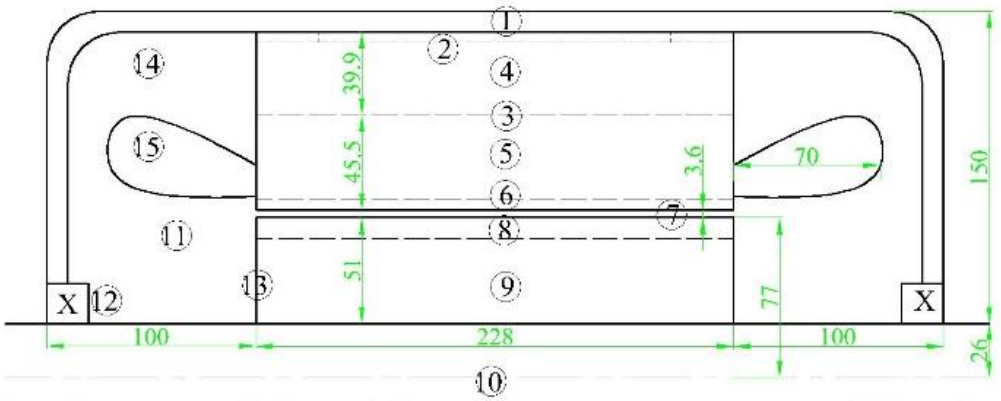

1) Motor Frame
2) Stator yoke upper
3) Stator yoke lower
4) Stator core
5) Stator winding
6) Stator teeth
7) Air-gap
8) Rotor Copper
9) Rotor Iron
10) Shaft axis
11) Air around end-widning
12) Bearing
13) Smooth rotor end
14) Non-ventilated
15) End-winding

Note: All dimensions are in millimeters.

Figure. 4.5. CRIM sectional view for the proposed study.

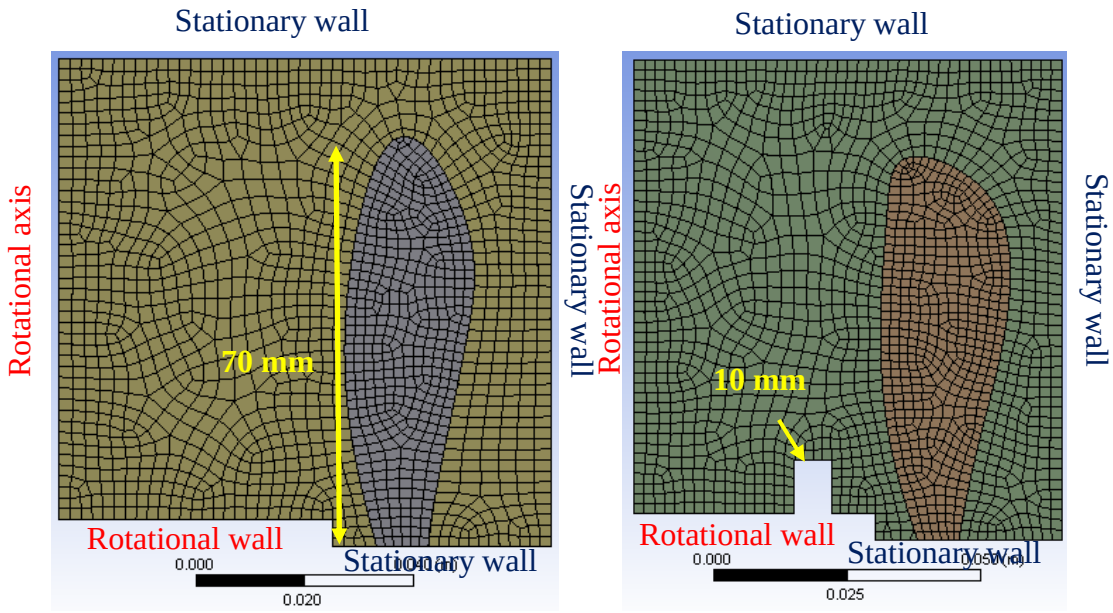

(a) (b)

Figure 4.6. CFD models (a) with rotor fins (b) with rotor fins.

to the motor endcap. Velocity vector was used to better represent air circulation results for different speed settings. Considering physics, higher speed is creating stronger circulation compared to lower speed. Overall though, the air velocity magnitude is within the ranges

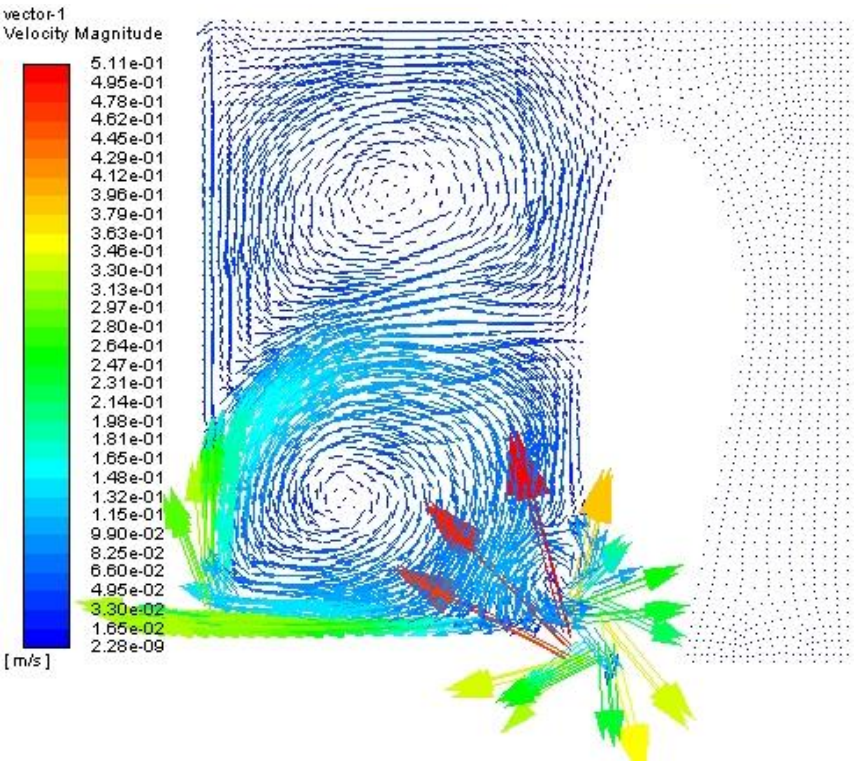

Figure 4.7. Air flow pattern at rotor speed 1,200 rpm.

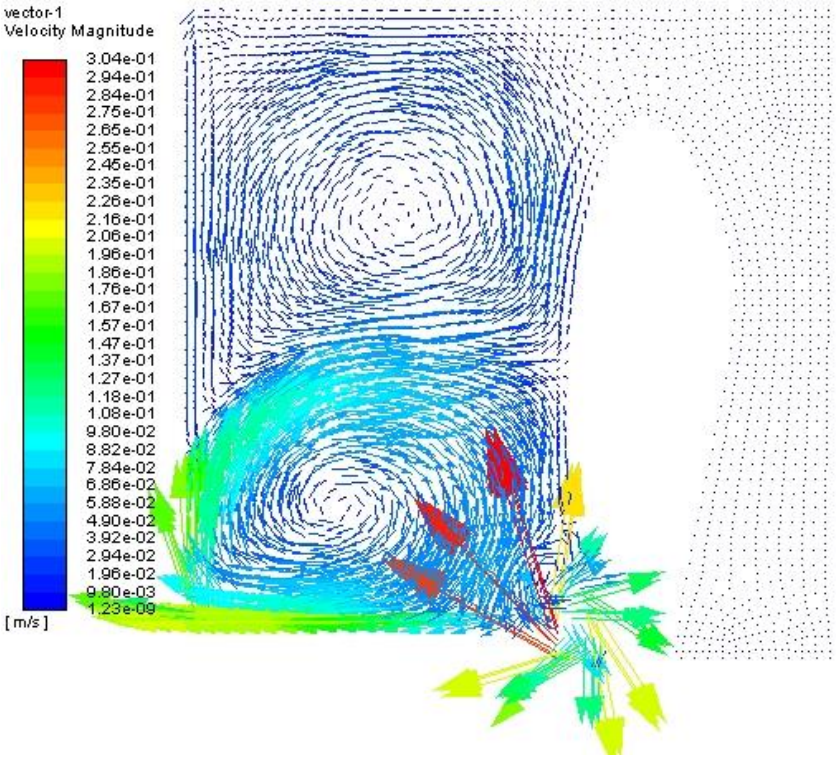

Figure 4.8. Air flow pattern at rotor speed 600 rpm.

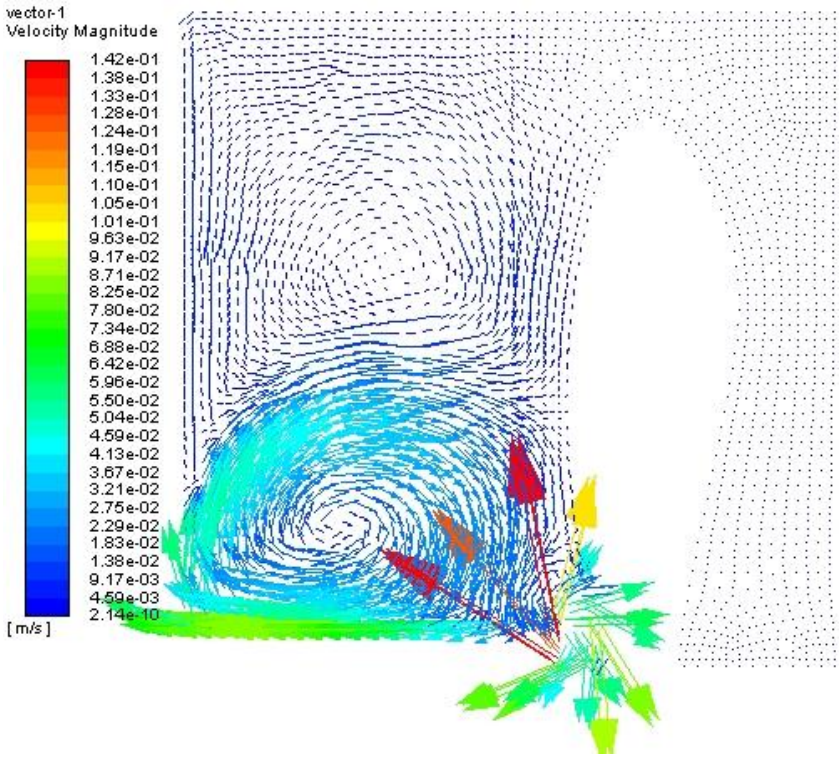

Figure 4.9. Air flow pattern at rotor speed 200 rpm.

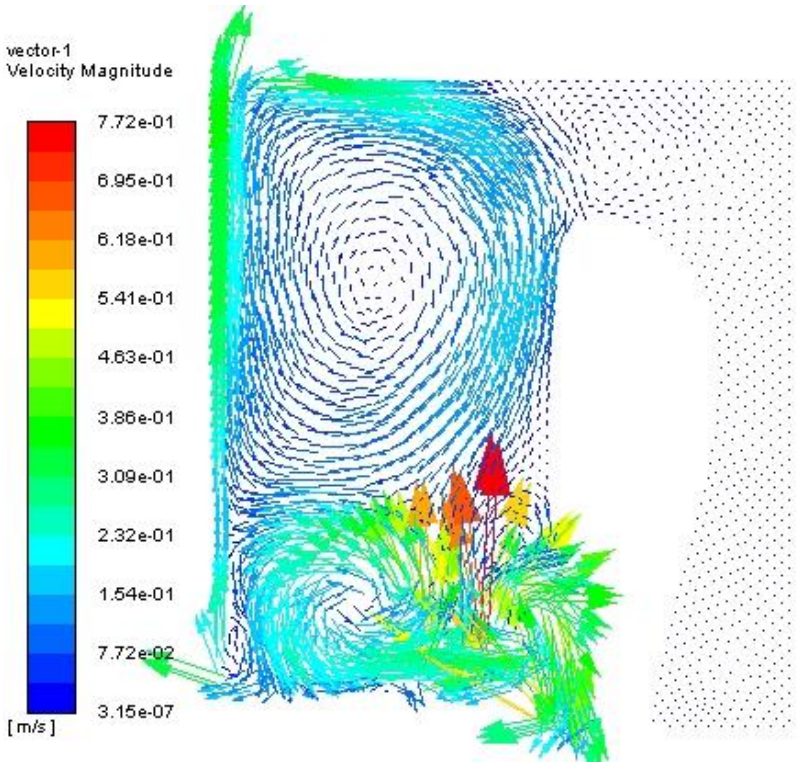

Figure 4.10. Air flow pattern at rotor speed 1,200 rpm with a small fin.

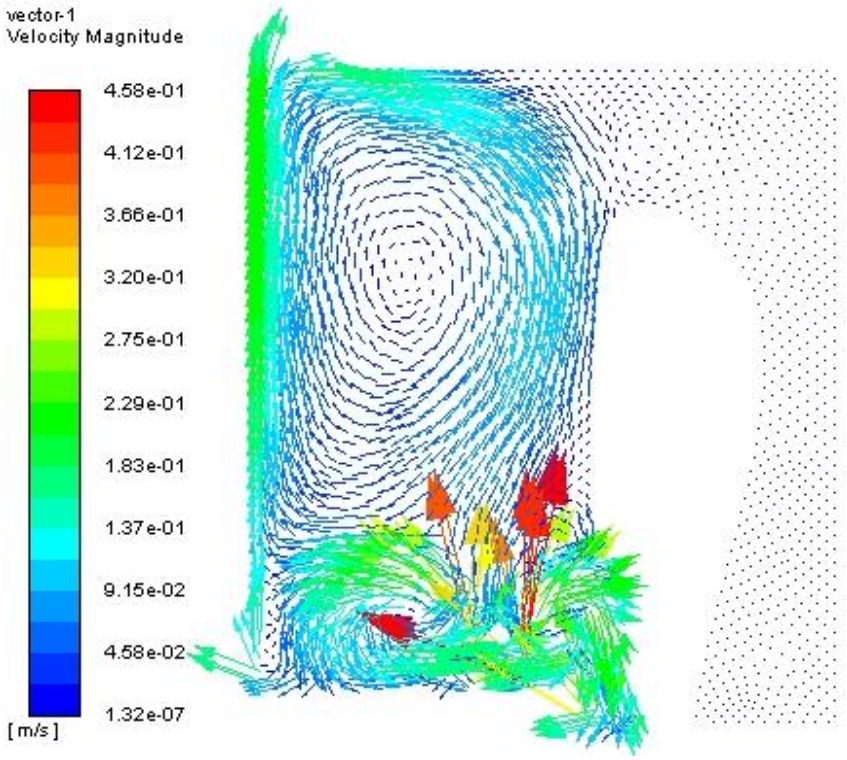

Figure 4.11. Air flow pattern at rotor speed 600 rpm with a small fin.

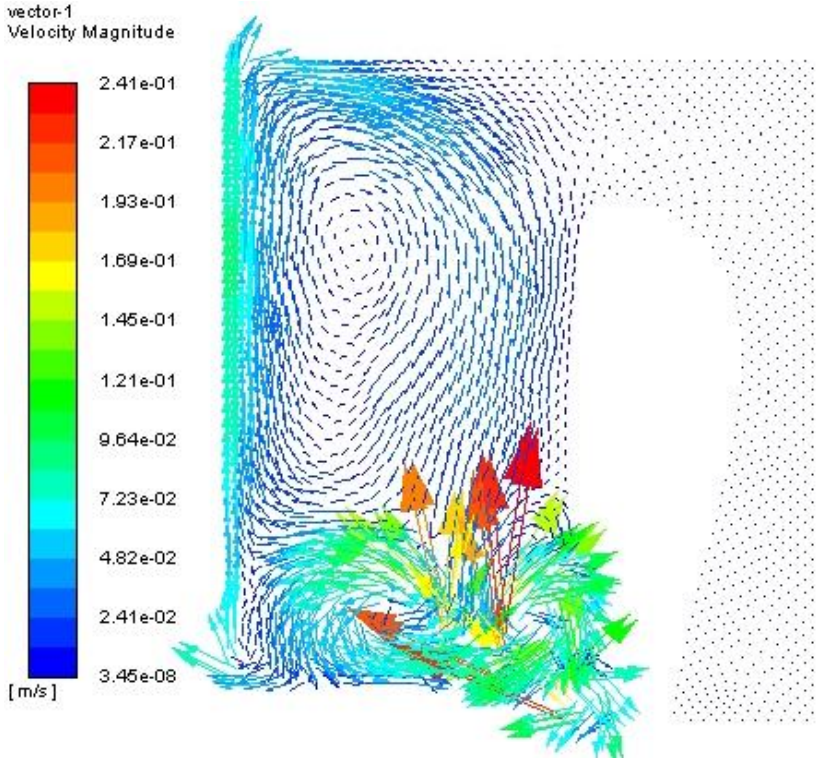

Figure 4.12. Air flow pattern at rotor speed 200 RPM with a small fin.

from around 0.1 m/s to 0.5 m/s which is not significant. This clearly demonstrates non-existent of rotor fins of blades like copper rotor creates weaker air velocity in the end-region. The CFD model with a small fin extension that generates comperatively stronger air circulation as shown in Figure 4.10, 4.11, and 4.12 that helps quicker heat dissipation through the endcap and casing. The results for the model with fin demonstrate similar air circulation pattern but with greater mangitude at 1,200, 600 and 200 rpm.

4.3.2 Validation of Air Flow Characteristics in the End-winding Region through Experiments

In order to validate air flow characteristics in the end-region from CFD simulation study, experimentally air velocity was measured in the end-region. Figure 4.13 shows the experimental setup measuring air velocity while the test motor is driven at a speed of 1,200 rpm, 600 rpm and 200 rpm. A hot wire anemometer was used to measure the velocity and the results are shown in Figure 4.14 and 4.15. The results show that air velocity is higher close to rotational axes of the rotor and the shaft. The velocity gets weaker as it moves towards the motor endcap.

4.3.4 Forced Convection Coefficients from End-winding

Convection heat transfer takes place when the fluid is in motion. The general equation to determine convection coefficient is expressed as [15]:

$$h_{combined} = {}^{\mathrm{Nu} \times \kappa_{air}}\!\!\diagup_{d} \tag{4.9}$$

where, $h_{combined}$ is the combination of natural and forced convection coefficients, Nu is the Nusselt number, d is the diameter of the cylinder and κ_{air} is the thermal conductivity. It is important to note that convection heat transfer coefficient is greatly influenced by the air velocity as well as flow characteristics whether it is laminar or turbulent [16]. From CFD analysis, it has been determined that flow pattern in the end-region of an electric even with smooth rotor ends such as CRIM is turbulent in nature. Such air circulations indicate that the heat transfer in the end-winding region takes place due to forced convection. On the other hand, for smooth rotor geometry the circulation is not strong enough and air velocity

ranges for the CRIM motor from 0.1 m/s to 0.5 m/s depending on the rotor speed ranges from 200 rpm to 1,200 rpm. Hence, convection heat transfer will consist of both free convection and forced convection in the end-winding region.

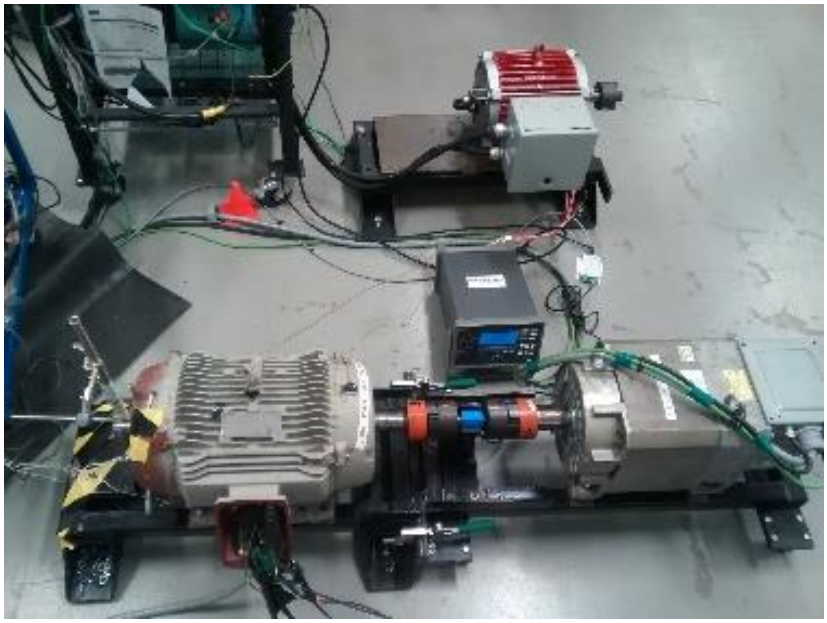

(a) DC thermal test setup.

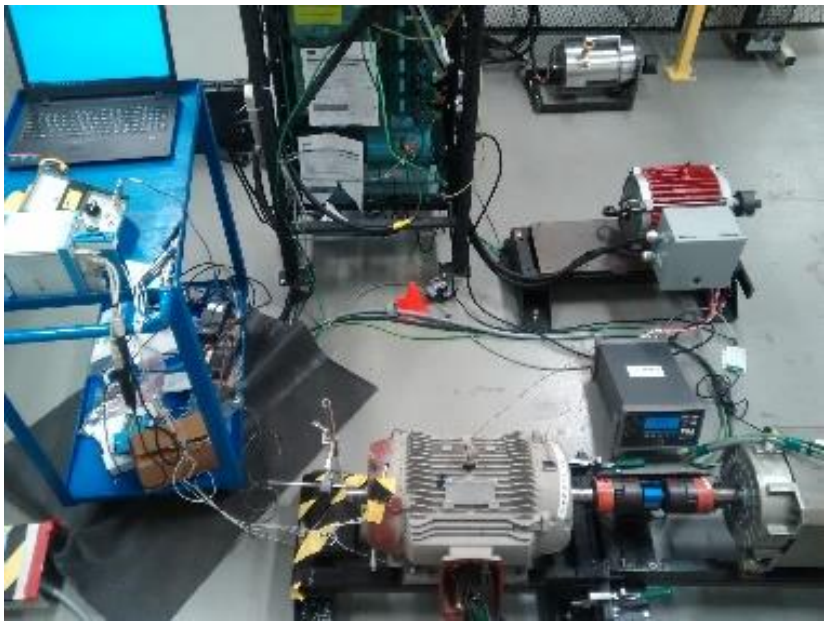

(b) Air velocity measurement test

Figure 4.13. Experimental Set-up (a) DC thermal test (b) air velocity measurement test on a 20-hp IM with copper rotor.

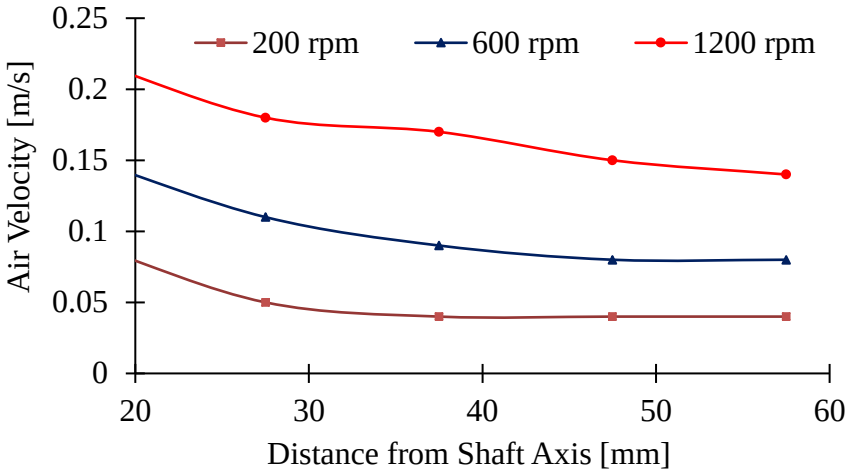

Figure 4.14. Measured air velocity in the vertical axis to the end-winding plane.

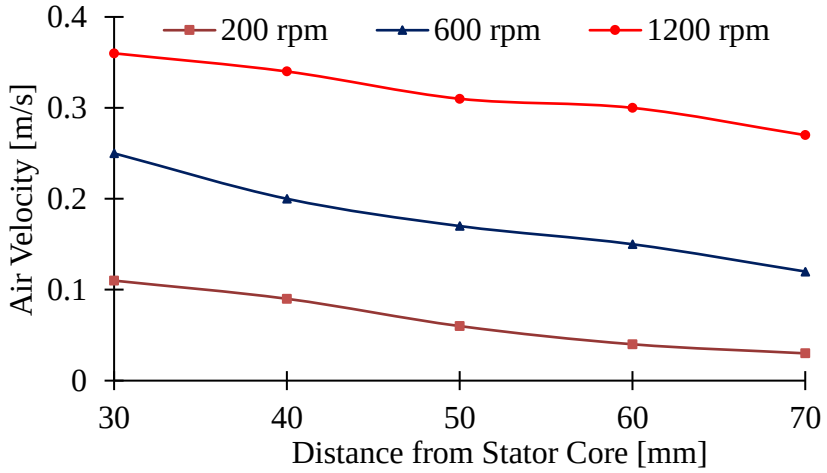

Figure 4.15. Measured air velocity in the horizontal axis to the end-winding plane.

As stated in [15], natural and forced convection situation arises when a fluid is forced over a heated surface at a rather low velocity. Coupled with forced-flow velocity is a convection velocity that is generated by the buoyancy forces resulting from a reduction in fluid density near the heated surface. The general notion that is applied in combined convection analysis is that the predominance of a heat transfer mode is governed by the fluid velocity with that mode [15]. A complete forced convection situation involving a fluid velocity of 30 m/s, for example, would be expected to overshadow most free convection effects encountered in ordinary gravitational fields because the velocities of free convection currents are small in

comparison with 30 m/s [15]. On the other hand, a forced flow situation at very low velocities (~0.3 m/s) might be influenced appreciably by free-convection currents [15]. The free convection boundary layer equation will indicate the general criterion for determining whether free convection effects dominate. The criterion for free convection dominance is expressed as [19]:

$$\mathrm{Gr}/\mathrm{Re}^{2} > 10 \tag{4.10}$$

From CFD analysis in Figure 4.7, 4.8, 4.9, and 4.10, comparatively stronger air circulation exists primarily close to the stator core end. This space can be assumed as a cylinder that contains the circulation. As it is evident that combined convection takes place in the end-winding region as well as the flow is turbulent in nature, the following empirical equation for mixed convection for turbulent flow can be used to calculate the Nusselt number which is the key parameter to calculate combined convection coefficient [15].

$$\mathrm{Nu} = 4.69 \times \mathrm{Re}^{0.27} \times \mathrm{Pr}^{0.21} \times \mathrm{Gr}^{0.07} \times \left(d/L\right)^{0.36} \tag{4.11}$$

where, Nu is the Nusselt number, Re is the Reynolds number, Pr is the Prandlt number, Gr is the Grashof number, d is the average diameter of stator end-winding and L is the axial length of end-winding.

$$\mathrm{Re} = \left(\rho \times v_{air} \times d \Big/ \mu \right) \tag{4.12}$$

where ρ is the density of air, v_{iair} is the air velocity and μ is the dynamic viscosity of air.

$$\mathrm{Pr} = \left(\mu \times c_p\right) \Big/ \kappa \tag{4.13}$$

where c_p is the specific heat capacity of air and κ is the thermal conductivity of air.

$$\mathrm{Gr} = \frac{\rho^2 \times g \times \beta \times \left(T_{end-wdg} - T_{iair}\right) \times d^3}{\mu^2} \tag{4.14}$$

where g is the gravity, β is the reciprocal of inner air temperature T_{iair} and $T_{end\text{-}wdg}$ is the end-winding temperature.

The air properties will be changing with change in temperature and the following expressions can be used to calculate temperature specific air properties.

$$\kappa_{air}=0.0000795T+0.00246\left[W/(m^{0}C)\right] \tag{4.15}$$

$$\kappa_{air}=0.0000795T+0.00246\left[W/(m^{0}C)\right] \tag{4.16}$$

$$\rho_{air}=0.00475T+2.5725\left[W/(m^{0}C)\right] \tag{4.17}$$

$$c_{p}=0.0325T+996.725\left[J/(kgK)\right] \tag{4.18}$$

$$\mu_{air}=5\times10^{-8}T\times310\times10^{-8}\left[kg/Pa.S\right] \tag{4.19}$$

From the mathematical solution using (4.11) – (4.19), Nusselt number was calculated and combined convection coefficient was calculated from (4.9). Steady state temperatures T_{iair} and $T_{end\text{-}wdg}$ were measured from no load experiments on the CRIM test motor. Table 4.6 shows calculated results of Nusselt number and convection coefficients for different air velocities. The value of Gr/Re^2 is also tabulated in the Table 4.6, which is the indication of the existence of natural convection and forced heat transfer in the end-winding region of the CRIM test motor. Combined convection coefficient results are plotted related to rotor speed and rotor peripheral speed as shown in Figure 4.16 and 4.17.

TABLE 4.6

COMBINED NATURAL AND FORCED CONVECTION HEAT TRANSFER COEFFICIENTS AT DIFFERENT ROTOR RPM

Rotor RPM	Inner air velocity, V_{iair} (m/s)	Nusselt Number (Nu)	Combined Convection coefficient ($W/m^2.^oC$)	Gr/Re^2
200	0.1	123.56	14.97	0.040
600	0.2	147.26	17.49	0.13
1200	0.4	178.68	21.48	0.79

The equations for graphs are displayed. If the line in the graph is extended towards left, it will intersect the y-axis ($h_{combined}$) at a value of 13.633 W/m^2.^{o}C and the rotor speed or peripheral rotor speed is zero. This clearly determines that the combined convection coefficient is:

$$h_{combined} = 0.407 r_p + 13.633 \tag{4.20}$$

where, $h_{combined}$ is the combined convection coefficient, complete natural convection coefficient is 13.633 W/m^2.^{o}C and forced convection coefficient is 0.4072r_p. Forced convection coefficient is a function of rotor peripheral speed of r_p.

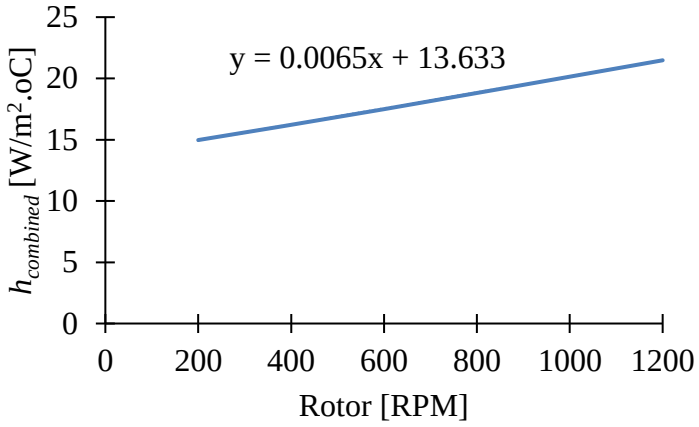

Figure 4.16. Combined convection coefficient varies with rotor speed rpm.

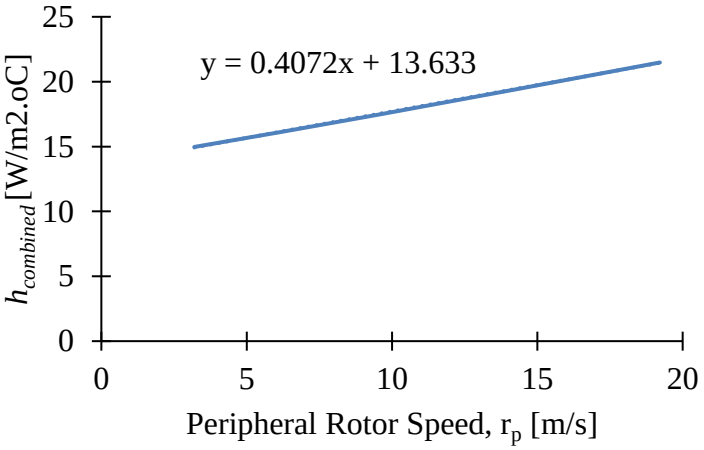

Figure 4.17. Combined convection coefficient with rotor peripheral speed (m/s).

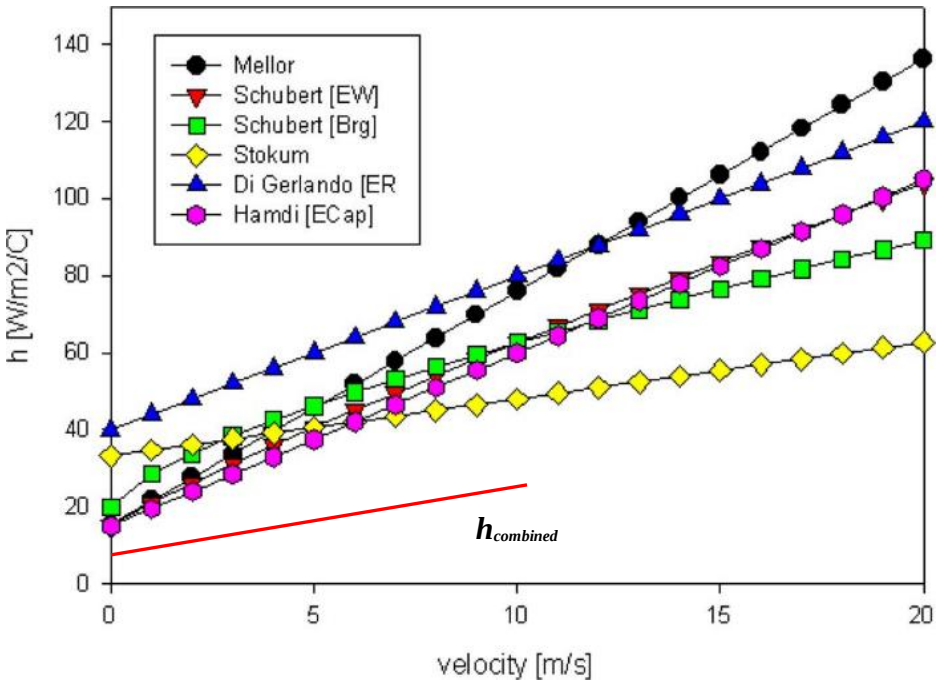

Figure 4.18. Comparison of proposed correlation for convection coefficient with the published ones by other models

This combined convection coefficient is compared with the findings from the past researchers which is shown in Fig. 4.16. The comparison in Figure 4.16 clearly determines the differences in the values of natural and forced convection coefficients between the published and the one calculated in this work. This difference is caused due to the rotor geometry with or without fins or blades on its end-rings. In Figure 4.18, all the published ones are convection coefficients for induction motor with aluminum rotor that has fins on its rotor end rings and $h_{combined}$ found in this paper for CRIM that has smooth rotor ends. It is critical to note that both natural and forced convection coefficients for CRIM have the lower values compared to aluminum rotor induction motor as expected.

It is also important to note that the natural convection coefficient component from (4.20) which is 13.633 W/m^2.^{o}C compares very close to the value of natural convection coefficient of 15.08 W/m^2.^{o}C in Table III that was determined from LPTN model solution technique. This comparison further confirms that the combined convection coefficient $h_{combined}$ found for CRIM in this work is valid. However, this relationship for convection coefficient will be different for different size of the motor. Hence, varying rotor diameter and axial length

of the end-winding are considered in calculation to further develop the relationship for convection coefficient. Figure 4.19 shows the convection coefficient for different motor sizes where d is the diameter of the rotor and L is the axial length of the end-winding and combine coefficient. The prototype motor in this research work has an axial length of the end-winding of 70 mm and rotor diameter of 220 mm. So, the ratio of axial length to diameter is 3.14 that has a convection coefficient of 22 $W/m^{2o}C$ at 1,200 rpm and 17 $W/m^{2o}C$ at 600 rpm.

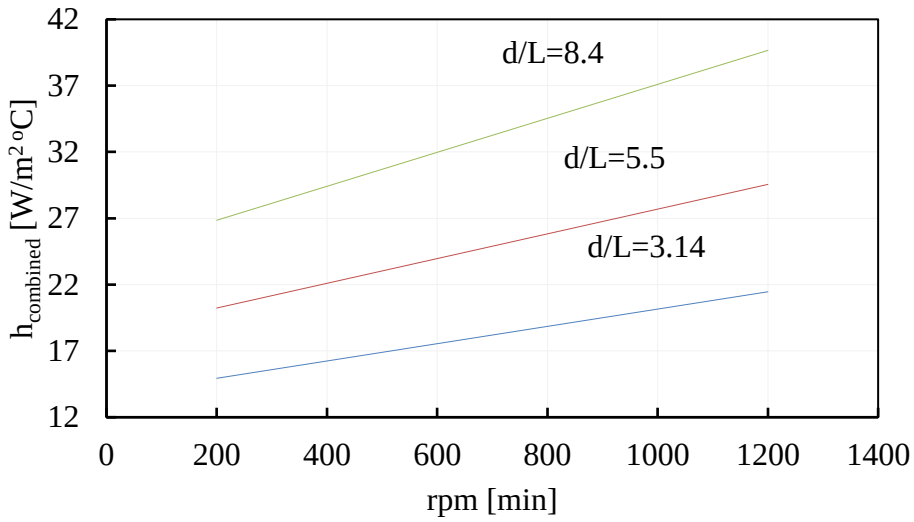

Figure 4.19. Convection coefficient in the end-winding of the motor that has no fins on its rotor end-rings.

4.4 Conclusion

In this paper, a simplified LPTN and CFD hybrid technique has been proposed to determine end-winding convection coefficient which is a critical thermal parameter to accurately predict stator winding temperature to ensure proper overload thermal protection for an electric motor that has smooth rotor geometry such as CRIM. This analytical solution and thermal parameter considerations are useful to develop the thermal model algorithm to be used for thermal protection purposes in the industries. A 20 hp CRIM was used as a test motor to find the convection coefficient. The key objectives that are met in this work are: (1) natural convection coefficient was determined using a simplified Lumped Parameter Thermal Network (LPTN) model and DC thermal tests (2) computational Fluid Dynamic (CFD) analysis was carried out for the determination of air flow characteristics in the end-winding region (3) analytical solution using empirical heat transfer equations and air flow

characteristics from Computational Fluid Dynamic (CFD) solution were used to determine natural and forced convection coefficients (4) compared the convection coefficients found by the researchers in the past with the results from this work (5) a generalized relationship for convection coefficient has been developed for different sizes of the motor.

4.5 References

[1] F. Ahmed and N. C. Kar, "Analysis of End-winding Thermal Effects in a Totally Enclosed Fan Cooled Induction Motor with Die Cast Copper Rotor," *IEEE Transactions on Industry* Applications, vol. 53, no. 3, pp. 3098 – 3109, 2017.

[2] R. M. Tallam, S. B. Lee, G. C. Stone, G. B. Kilman, J. Yoo and T.G. Habetler "A Survey of Methods for Detection of Stator-Related Faults in Induction Machines" IEEE Transactions on Industry Applications, volume 43, no 4, July/August 2007.

[3] P. Zhang, Y. Du and T. G. Habetler, "A Transfer-Function-Based Thermal Model Reduction Study for Induction Machine Thermal Overload Protective Relays" IEEE Transactions on Industry Applications, volume 46, No. 5, 2010.

[4] A. Boglietti and A. Cavagnino, "Analysis of the end-winding cooling effects in TEFC induction motors," IEEE Transactions on Industry Applications, volume 43, issue 5, pp. 1214-1222, 2007.

[5] C. Micallef, S. J. Pickering, K. Simmons, and K. Bradley, "Improvements in air flow in the end region of a large totally enclosed fan cooled induction motor," Proc. of IEMDC'05 IEEE International Electric Machines and Drives Conference, San Antonio, May 2005.

[6] A. Boglietti, A. Cavagnino, D. Staton, M. Popescu, C. Cossar, and M.I. McGilp, "End space heat transfer coefficient determination for different induction motor enclosure types", IEEE Trans. on Industry Applications, vol. 45, No. 3, May/June 2009, pp. 929-937

[7] E. Schubert, "Heat Transfer Coefficients at End Windings and Bearing Covers of Enclosed Asynchronous Machines," Elektrie, vol. 22, April 1968. pp160-162. (Translation ERA/IB 2846).

[8] A. Boglietti, A. Cavagnino, D. Staton, and M. Popescu, "Impact of different end region cooling arrangements on endwinding heat transfer coefficients in electric motors," Proc. IEEE Conf. on Industrial Electronics, 978-1-4244-4649-0/09.

[9] A. Boglietti, A. Cavagnino, M. Lazzari, and M. Pastorelli, "A simplified thermal model for variable speed self cooled industrial induction motor," IEEE Transactions on Industry Applications, volume.39, No.4, July/August 2003, pp. 945-952.

[10] D. A. Staton and A. Cavagnino, "Convection Heat Transfer and Flow Calculations Suitable for Electric Machines Thermal Models, Member, IEEE Transactions on Industrial Electronics, vol. 55, no. 10, October 2008.

[11] C. Micallef, S. J. Pickering, K. A. Simmons, and K. J. Bradley, "An Alternative Cooling Arrangement for the End Region of a Totally Enclosed Fan Cooled (TEFC) Induction Motor," 4th IET Conference on Power Electronics Machines and Drives, pp. 309-309, (2008).

[12] D.T. Peters, J.G. Cowie, E.F. Brush, Jr. and D.J. Van Son, "Copper in the Squirrel Cage for Improved Motor Performance," International Electric Machines and Drives Conference, June, 2003.

[13] E.F. Brush, J.G. Cowie, D.T Peters and D.J. Van Son, "Die-Cast Copper Motor Rotors; Motor Test Results, Copper Compared to Aluminum", Energy Efficiency in Motor Driven Systems, Eds: F. Parasiliti & P. Bertoldi, Published by Springer, 2003, p 136 to 143.

[14] F. Ahmed, E. Ghosh, and N.C.Kar, " Transient Thermal Analysis of a Copper Rotor Induction Motor using a Lumped Parameter Temperature Network Model," in IEEE Transportation Electrification Conference and Expo (ITEC), June 2016.

[15] J.P., Holman.‘‘Heat Transfer” 9th ed., McGraw-Hill, 2002, pp. 640-647.

[16] J. Pyrhonen, T. Jokinen and V. Hrabovcova, “Design of Rotating Electric Machines”, 2008 John Wiley & Sons, Ltd. ISBN: 978-0-470-69516-6.

[17] E. Ghosh, F. Ahmed, A. Mollaeian, and N. C. Kar, “Online Parameter Estimation and Loss Calculation using Duplex Neural-Lumped Parameter Thermal Network for Faulty Induction Motor,” in Proc. of the IEEE Conference on Electromagnetic Field Computation, Florida, 2016.

[18] F. Ahmed, E. Ghosh, and N. C. Kar, “Transient Thermal Analysis of a Copper Rotor Induction Motor using a Lumped Parameter Temperature Network Model,”in Proc. of the IEEE Transportation Electrification Conference, Michigan, USA, 2016.

[19] E. Ghosh, F. Ahmed, N. C. Kar, “Temperature Influenced Online Stator Resistance Estimation Using an Improved Swarm Intelligence Technique for Induction Machine,” in proc. of IEEE Transportation Electrification Conference and Expo, 2015.

[20] K. Hafiz, G. Nanda and N.C. Kar, “Comparative Performance Analysis of Aluminum Rotor and Copper Rotor SEIG Considering Skin Effect,” Proc. of the IEEE International Conference on Electric Machines, Portugal, September, 2008.

CHAPTER 5

LPTN MODELLING FOR THERMAL CHARACTERIZATION AND PROTECTION OF AN INTERIOR PERMANENT MAGNET SYNCHRONOUS MOTOR (IPMSM) FOR ELECTRIC VEHICLE APPLICATION

5.1 Introduction

In the past, thermal design of electric machines has received less attention compared to electromagnetic design of the machines [1]. The motor designers used to thrive to improve the electromagnetic design of the motor whereas thermal aspects were dealt superficially. However, as the industry demands high torque and power density from the electric motor specifically, for electric vehicle application, thermal analysis has gotten more and more attention from the researchers in order to provide improved motor efficiency and power density. High torque density requirement means increasing current and consequently, higher temperature rise in the motor. The permanent magnet synchronous motor (PMSM) is the most commercially viable traction motor in which temperature of stator winding and permanent magnet have direct effects on the torque and power generation. In order to maintain the designed peak and rated torque and power capability of the motor determined by the drive cycles, it is critical to maintain the operating temperature within the safe limit. If this temperature of the winding and permanent magnet exceeds permissible thermal limit frequently due to lack of proper understanding and managing of the thermal conditions of the motor, it will not only reduce the motor performance as well as it will have detrimental effects on the life of insulation material and consequently, it will cause permanent insulation breakdown. On the other hand, demagnetization due to higher temperature will cause a permanent damage to the motor. Hence, it is critical to understand thermal characterization of the motor to provide required toque and power as well as to generate sufficient thermal information to develop a thermal model-based motor protection in electric vehicle applications. There are three different techniques that are used at present to estimate stator winding temperature for motor protection. First, direct measurement techniques where resistance temperature detectors (RTDs) and thermocouples are used to measure the winding temperature. It is extremely difficult to install these temperature

sensors and replace them if they are damaged. Second, motor parameter-based technique involves estimation of stator resistance as the temperature has direct relationship with the changes in resistances, but it is extremely difficult to estimate resistance at high speed conditions and they are susceptible to parametric errors. Third, thermal model-based technique involves estimation of stator winding temperature and then compares with the thermal limit curves to determine thermal overload protection of the motor. Once the estimated temperature exceeds the thermal overload limit, it will trip the motor. In this approach, both time delay fuses and overload relays simulate the thermal limit curve and a simple thermal model is used where trip time is calculated based on name plate rating of the motor. Such thermal model is too simple to predict accurate temperature of stator winding and also, the motor is considered as a homogeneous body in this technique which is absolutely impossible as the motor is made of all different materials with different thermal properties [1]-[3]. Furthermore, heat is an accumulated effect in the motor from all different motor power losses that contribute to heating of the motor. It is never possible to predict motor temperature accurately without a proper and adequate thermal model [1]. Hence, this paper proposes a computationally efficient integrated LPTN model that will consider all major power losses in the motor including stator copper losses, lamination and magnet losses as well as active cooling requirements. This model can easily be integrated into the drive model of the electric vehicle that will not only determine thermal characterization of the motor as well as it will ensure motor thermal protection LPTN model has been used for thermal analysis of electric motors in the past but LPTN model based thermal protection in the electric vehicle is unique and new application. The proposed integrated model will consist of motor loss model and thermal network model where the motor loss model dynamically takes input of electrical parameters to determine the motor losses to be used as input for the thermal model. A detailed but simplified enough thermal model will provide all thermodynamic equations and material thermal properties to determine temperature in the motor. In this case, numerical technique involving Finite Element Analysis (FEA) and CFD analysis can never predict temperature faster than LPTN modelling approach and satisfy the needs for motor thermal protection in electric vehicle in dynamic driving conditions. This research uses a 4.3 kW interior permanent magnet synchronous motor (IPMSM) prototype that has been designed and built at the Center for

Hybrid Automotive Research and Green Energy laboratory at the University of Windsor, one of the leading research laboratories in electrified transportation systems.

5.2 Integrated Lumped Parameter Thermal Network Model (LPTN)

The most efficient procedure to analyze the heat transfer in an electric motor is based on lumped parameters, as indicated in many technical literatures of this subject [1]-[12]. In order to determine temperature at the various components or at each node, it requires only dimensional information and thermal parameters. At each temperature node, energy balance calculations are performed to determine the temperature rise at various locations in the motor components. The heat sources in the motor are uniformly distributed. In [13], for lumped heat capacity, rate of increase of internal energy equals to heat transfer by conduction plus heat transfer by convection plus heat transfer by radiation plus any active heat source present in the system which is expressed by the following general form of equation:

$$\rho c V dT/dt = \begin{bmatrix} P_{motor-loss} + h_{conv} A_{conv}\left(T_{conv} - T_{ref}\right) \\ + \sigma \varepsilon A_{rad}\left(T_{rad}^4 - T_{ref}^4\right) + \dfrac{\kappa A_{cond}}{\Delta x}\left(T_{cond} - T_{ref}\right) \end{bmatrix} \tag{5.1}$$

Here, h_{conv}, T_{conv}, T_{cond} and T_{rad} are to vary with time and then (5.1) can be written in finite difference form suitable for numerical solution. Designating the temperatures at the start of a time increment with subscript *(p)* and the temperatures at the end of the time increment dt with subscript (p+1), now (1) becomes:

$$T_{p+1} = T_p + \left[\begin{Bmatrix} P_{motor-loss} + h_{conv} A_{conv}\left(T_{conv} - T_{ref}\right) + \sigma \varepsilon A_{rad}\left(T_{rad}^4 - T_{ref}^4\right) \\ + \dfrac{\kappa A_{cond}}{\Delta x}\left(T_{cond} - T_{ref}\right) \end{Bmatrix} \times \left(dt/\rho c V\right) \right] \tag{5.2}$$

5.2.1 Loss Model Setup for the Integrated Thermal Model

The motor losses generate depending on the loading torque and speed conditions of the traction motor which are determined by the drive cycles in electric vehicle. An example of torque-speed profile of an IPMSM is shown in Figure 5.1 for two standard drive cycles, Urban Dynamometer Driving Schedule (UDDS) and Highway Fuel Economy Driving Schedule (HWFET) where it has been identified that the loading torque follows the driving

conditions [14]. The loss profile of the motor will exactly be following the loading torque and speed conditions of the motor.

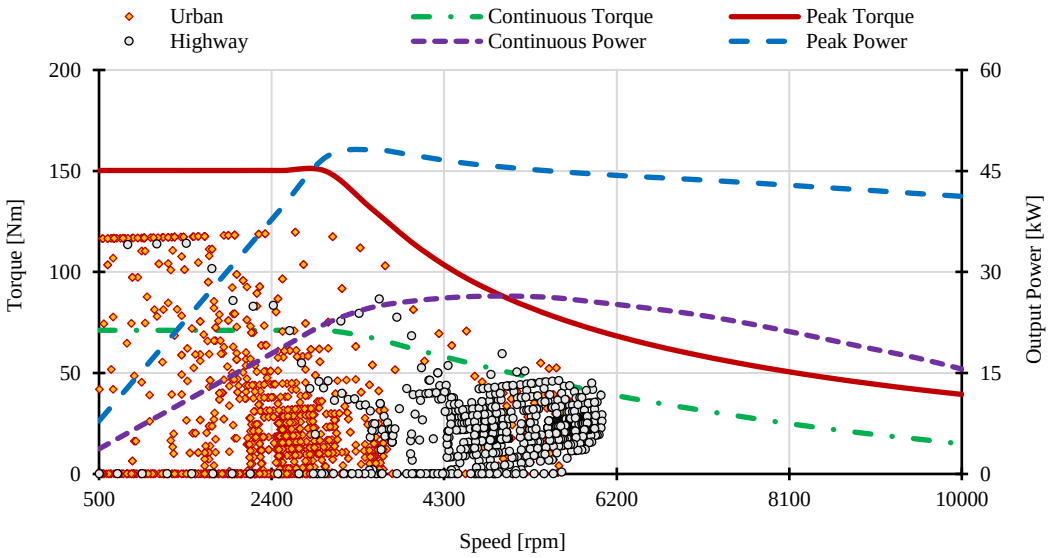

Figure 5.1. Motor speed and torque for UDDS and HWFET [14].

These losses can be calculated using motor loss equations, however, in this research work, the proposed integrated thermal model uses a constant loading torque and speed conditions to validate the model. The prototype test motor used in this work is in Figure 5.2 and Table 5.1 describes the specification of the test motor. The model considers power losses in the motor that are converted into active heat and are determined from electromagnetic simulation for the prototype IPMSM. Table 5.2 shows the different loss values for three different loading torque conditions of 70 Nm (rated), 58 Nm and 40 Nm at 575 rated rpm and these losses are used in the proposed thermal model developed in MATLAB Simulink.

(a) (b)

Figure 5.2. Parts of IPMSM. (a) rotor with shaft and bearings. (b) Assembled motor.

TABLE 5.1

TECHNICAL SPECIFICATIONS AND PHYSICAL DIMENSIONS OF IPMSM

Parameters	Values	Parameters	Values
Rated output power	4.25 kW	Length of rotor core	136 mm
Rated voltage	275 V	Thickness of magnet	3.81mm
Rated torque	70 Nm	Width of magnet	25.4 mm
Rated speed	575 RPM	Shaft radius	42.5 mm
Maximum speed	1,750 RPM	Type of steel	M19_29G
Continuous phase current	11 A rms	Type of magnet	NDFEB35@100
Inner diameter of stator	135 mm	Weight of copper	3.76 kg
Outer diameter of stator	220 mm	Weight of stator core	19.6 kg
Stator stack length	136 mm	Weight of rotor core	7.12 kg
Airgap	0.5 mm	Weight of magnet	0.615 kg
Outer rotor diameter	134 mm		

TABLE 5.2

LOSS DATA FROM ELECTROMAGNETIC SIMULATION OF IPMSM

Loss Parameters	Loading Torque (Nm)		
	70 Nm	58 Nm	40 Nm
$P_{cu\text{-}S}$	230 W	155 W	71 W
$P_{cu\text{-}eddy}$	4.27 W	3.77 W	2.87 W
P_{mag}	1.88 W	2.371 W	3.144 W
P_{lam}	19.98 W	17.52 W	13.49 W

5.2.2 Proposed LPTN Model Setup for the Proposed IPMSM Motor

The simplified LPTN models are proposed in Figure 5.3. In the LPTN model development, the motor is considered symmetrical around the shaft axis and the heat generated at the stator winding, magnet, rotor and stator core travels radially towards the casing through each node and finally to the ambient. Each node represents the different material component of the motor such as rotor core, magnet, air gap, stator winding and stator teeth, stator lamination and motor casing. Both models are identical except thermal resistances for active cooling requirements in the models. In thermal model as shown in Figure 5.4(a), air cooling is considered where a fan is used to blow the air over the fins on the casing. If the fan is not used, the prototype motor casing is cooled by natural convection only to the ambient. Ambient temperature is a critical and limiting factor in air cooling system to perform with higher efficiency in case of electric vehicle application. Hence, the authors propose here to test the model first using a fan cooling to justify the cooling requirements for the prototype motor. Second, in Fig. 5.3 (b) a liquid cooling is investigated by including

a negative heat source, $P_{coolant}$ in the LPTN model. As the heat from the motor reaches the stator outer surface, water-glycol mixture which is generally used as a coolant removes the heat from the motor. Table 5.3 describes all the model thermal parameters. In order to increase computational efficiency, both models are created in MATLAB Simulink software which are shown in Figure 5.4 and 5.5. The MATLAB files for the losses are created as input to the thermal model.

Section C describes all LPTN model equations to calculate motor temperature. All the equations are created in MATLAB Simulink to determine conduction and convection parameters from the LPTN model. Figure 5.5 includes a liquid cooling block that removes the heat as a percentage of the total heat loss in the motor. The cooling channel or heat exchanger design is not a part of the investigation in this paper. The focus was given to the LPTN model setup that can easily be adopted for any motor to calculate stator winding and magnet temperature quickly and regulate the liquid cooling in the motor to keep the operating temperature within a safe limit.

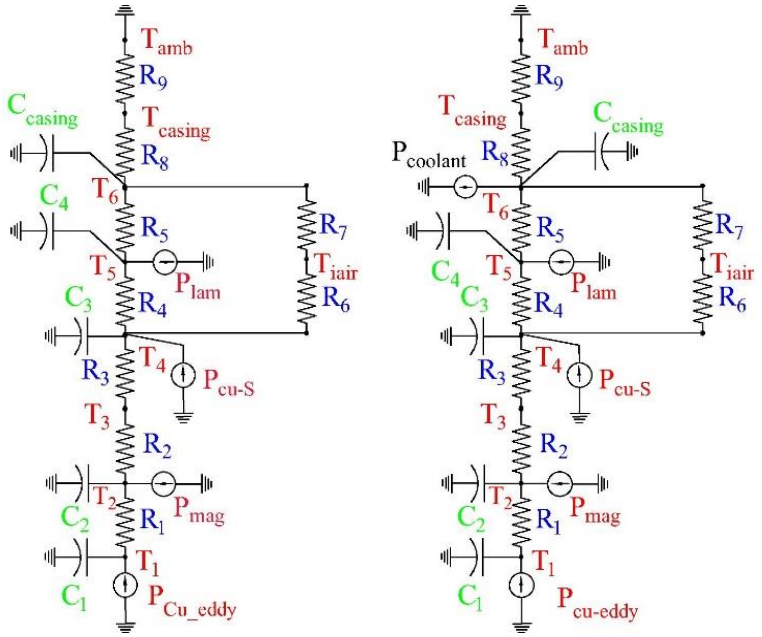

Figure 5.3. Proposed simplified Lumped Parameter Thermal Network Model for IPMSM (a) fan cooling (b) liquid cooling.

TABLE 5.3

LUMPED PARAMETER THERMAL NETWORK MODEL PARAMETER

Item	Description of model parameters	Item	Description of model parameters
$P_{cu\text{-}S}$	Stator copper loss	C_3	Thermal capacitance for stator teeth
$P_{cu\text{-}eddy}$	Rotor core loss	R_4	Thermal resistance for conduction through stator teeth/winding
P_{mag}	Magnet loss	C_4	Thermal capacitance of stator core
P_{lam}	Stator core loss	R_5	Thermal resistance for conduction through stator core
$P_{coolant}$	Heat removal by Water-glycol coolant	C_5	Thermal capacitance of stator winding
R_1	Thermal resistance for conduction through rotor core	C_{casing}	Thermal capacitance for casing material
C_1	Thermal capacitance of rotor lamination material	R_6	Thermal resistance for convection from end-winding
R_2	Thermal resistance for conduction through magnet	R_7	Thermal resistance for convection from inner air
C_2	Thermal capacitance of magnet material	R_8	Thermal resistance for conduction through casing
R_3	Thermal resistance for convection through airgap	R_9	Thermal resistance for convection from casing

5.2.3 Heat Transfer and Proposed Analytical Solution

Table 5.4 describes thermal properties that are used in calculating thermal resistances and capacitances. The thermal resistances are expressed by the heat transfer equations such as thermal resistance due to forced convection heat transfer from motor frame to the ambient (5.3), thermal resistance for convection through airgap between stator and rotor (5.6), thermal resistance for conduction through rotor core (5.10), thermal resistance due to conduction through magnet (5.11), thermal resistance for conduction through stator winding and teeth (12), resistance due to radial conduction through stator iron (5.13), thermal resistance through convection at stator end-winding from Figure 5.7.

$$R_{18} = {}^{1}\!\!\diagup\!\!{}_{A_{fr} h_{fin}} \tag{5.3}$$

TABLE 5.4

MATERIAL THERMAL PROPERTIES OF IPMSM MOTOR

Material	Properties		
	Density (kg/m^3)	Specific Heat (J/kg-K)	Thermal Conductivity (W/m-K)
Steel	7850	475	50
Magnet	7550	460	8.95
Copper	8930	385	379
Air	1.009	1009	0.02624
Lamination	7850	500	25

where, A_{fr} is motor frame area; h_{fin} is the forced convection coefficient for the motor frame to the ambient. The fin channels are semi-open and a special formulation can be used to calculate convection heat transfer coefficient" [10].

$$h_{fin} = \left(\rho c_p D v_{fin}\right) \Big/ \left[4 \times L_{fin} \times \left(1 - e^{-m}\right)\right] \tag{5.4}$$

$$m = \frac{0.1448 L_{fin}^{0.946}}{D^{1.16} \times \left\{k_{fin} / \rho c_p v_{fin}\right\}^{0.214}} \tag{5.5}$$

where, L_{fin} is the axial length of the fin, D is hydraulic diameter and v_{fin} is the air velocity in the fin channels [10].

$$R_2 = 1 \Big/ A_{rot} h_{airgap} \tag{5.6}$$

$$h_{airgap} = \mathrm{Nu} \times \kappa_{air} \Big/ l_{airgap} \tag{5.7}$$

According to Becker and Kaye [10]

Nu=2 for Ta_m<1,700 (laminar flow)

$Nu=0.128Ta_m^{0.367}$ for $1{,}700< Ta_m <10^4$

$Nu=0.409Ta_m^{0.241}$ for $10^4< Ta_m <10^7$

T_a is the Taylor number and the following Taylor equation can be used to determine the flow type:

$$T_a = \frac{\rho^2 \omega^2 r_m \delta^3}{\mu^2} \tag{5.8}$$

where, ω is the angular velocity of the rotor, ρ is the mass density of the fluid, μ is the dynamic viscosity of the fluid and r_m is the average of the rotor and stator radii. The radial air-gap length, δ and the rotor radius are taken into account by a modified Taylor number:

$$T_{a_m} = T_a / F_g \tag{5.9}$$

where, F_g is the geometrical factor. In practice, the air-gap length is so small compared with the rotor radius that F_g is close to unity and $Ta_m \approx Ta$ [10].

$$R = \frac{1}{2\pi \kappa_{rot} l_{rot}} \ln\left(\frac{r_{rot}}{r_{rot-o}}\right) \tag{5.10}$$

where, κ_{rot} thermal conductivity of rotor, l_{rot} axial length of rotor core, $r_{rot\text{-}o}$ outer radius of rotor.

$$R = \frac{1}{n\theta \kappa_{mag} l_{mag}} \ln\left(\frac{r_{mag}}{r_{rot}}\right) \tag{5.11}$$

where, r_{mag} inner rotor radius, r_{rot} is rotor core radius, n is number of poles, θ is radian of one pole, κ_{mag} is thermal conductivity of magnet l_{mag} is axial length of magnet.

$$R = \frac{1}{2\pi k_{iron} l_{st} p} \ln\left(\frac{r_{slot}}{r_{st-i}}\right) \tag{5.12}$$

where, κ_{iron} is thermal conductivity of iron, l_{st} is axial length of stator core, r_{slot} is inner radius of stator slot, $r_{st\text{-}i}$ is outer radius of stator, p is percentage of teeth section with respect to the total teeth plus all slots section.

$$R = \frac{1}{2\pi k_{\text{iron}} l_{st}} \ln\left(\frac{r_{st-yoke-o}}{r_{st-yoke-i}}\right) \tag{5.13}$$

where, κ_{iron} is thermal conductivity of iron, l_{st} is axial length of stator core, $r_{st\text{-}yoke\text{-}o}$ is outer radius of stator yoke, $r_{st\text{-}yoke\text{-}i}$ is inner radius of stator yoke. Since the flow characterstics have been complex in nature in the end-winding region of an electric motor, the author proposed the following relationship for combined convection coefficient in the end region for the prototype motor [15]. Figure 5.6 shows the convection coefficient for different motor sizes where d is the diameter of the rotor and L is the axial length of the end-winding. The prototype motor in this research work has an axial length of the end-winding of 45 mm and rotor diameter of 1354 mm. So, the ratio of axial length of the end-winding to rotor diameter is 3 that has a convection coefficient of 20 W/m^{2o}C at 575 rpm.

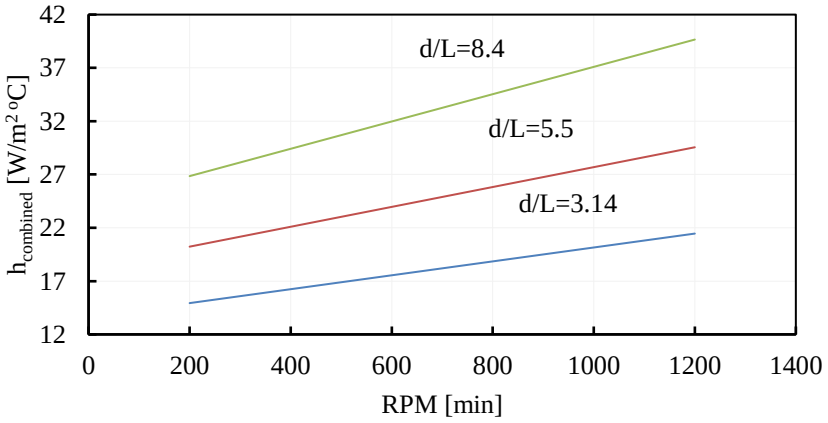

Figure 5.6. Convection coefficient in the end-winding in the motor.

5.4 Experimental Setup

A 4.3 kW motor prototype is shown in Figure 5.7. For the prototype, no active forced cooling from a fan was used. All the heat generated inside the motor dissipates through the fins on the motor casing by natural convection. For temperature measurements, Resistance Temperature Detectors (RTDs) were embedded in the stator end-windings of the prototype. RTDs were connected to computer through DAQ unit and temperature rise results were recorded. The motor was tested under different loading conditions and rated speed to investigate the temperature rise at different state of motor operation.

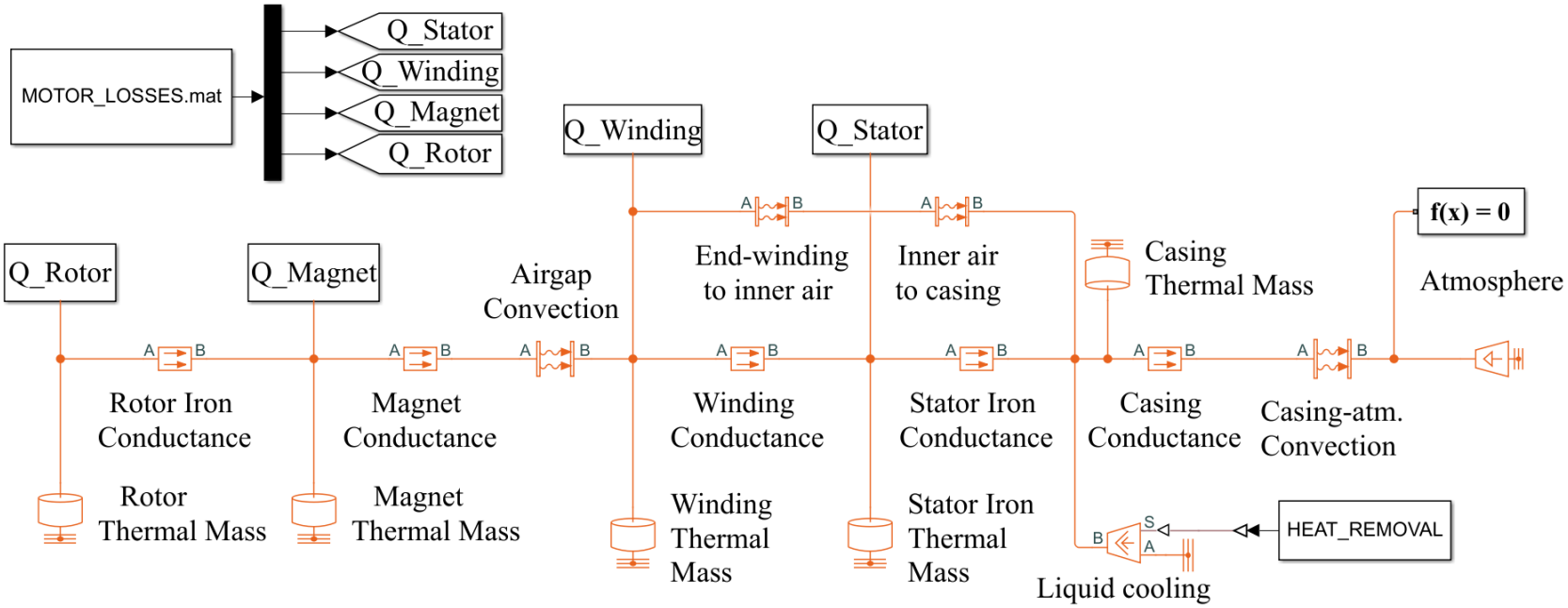

Figure 5.4. Proposed simplified LPTN model with liquid cooling.

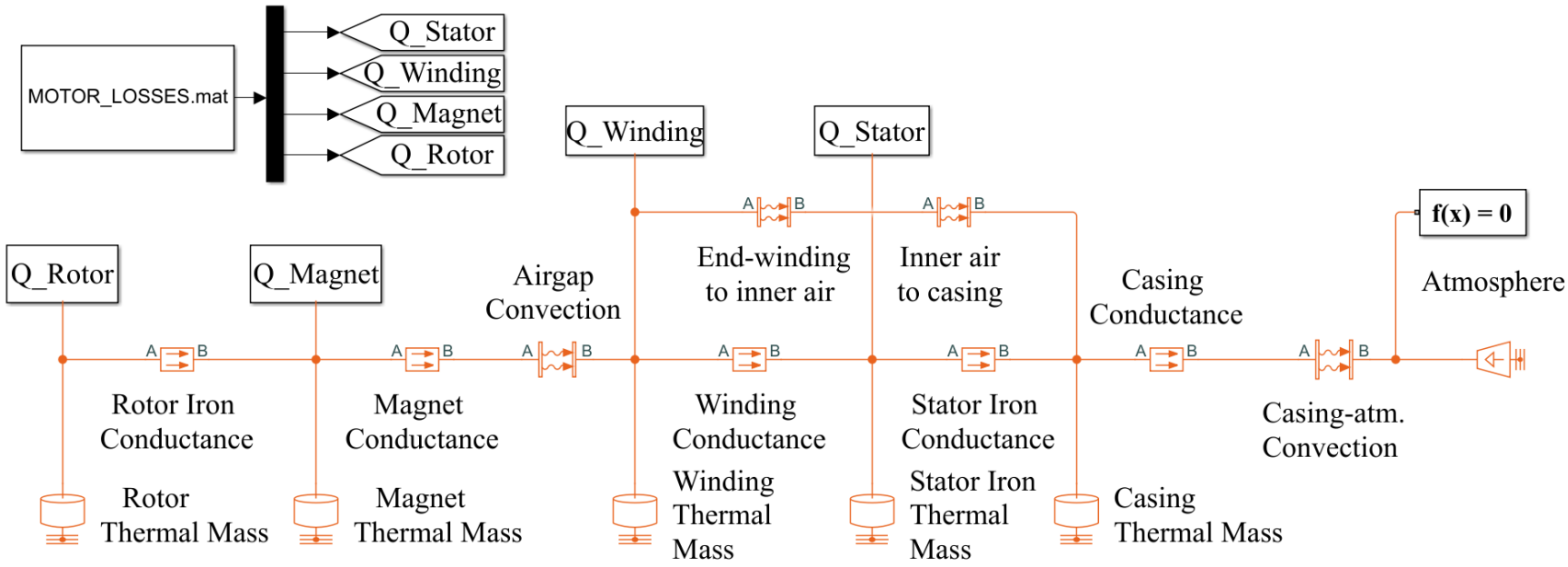

Figure 5.5. Proposed simplified LPTN model with air cooling.

Figure 5.7. Thermal Test Setup for 4.3 kW IPMSM.

5.5 Results and Discussion

LPTN model calculates temperature with and without fan cooling. In actual experiments, no active forced fan cooling was used and motor was cooled through natural convection to the ambient. LPTN model calculated results are compared with experimental results in section A. LPTN model also simulates liquid cooling for the test motor and calculates winding temperature for liquid cooling which is discussed in section B.

5.5.1 Comparison of LPTN and Experimental Results - Air Cooling

The test motor was driven by a torque-controlled dyno for loading conditions of 70 Nm, 58 Nm and 40 Nm. With the increase in loading torque the motor requires higher current. As a result, temperature rises in various parts of the motor. For different load settings, various losses are used as input in LPTN model and the model predicts the temperature of the motor components which are shown in Figure 5.8. Winding temperature reaches around 80^0C with simulated forced convection cooling which is much higher compared to any other parts of the motor. In LPTN model, forced convection was achieved by setting an air velocity of 8 m/s in the calculation.

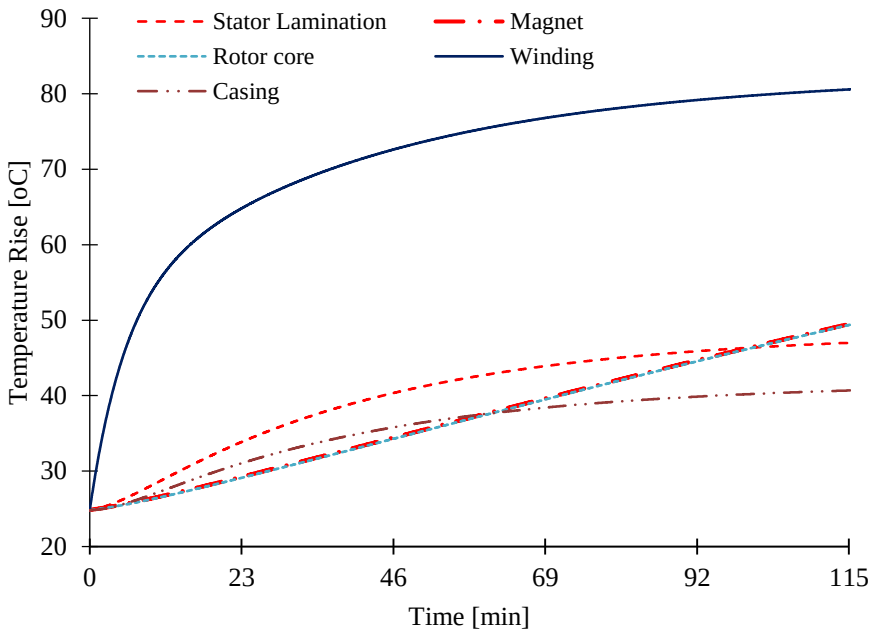

Figure 5.8. LPTN predicted temperature for motor parts.

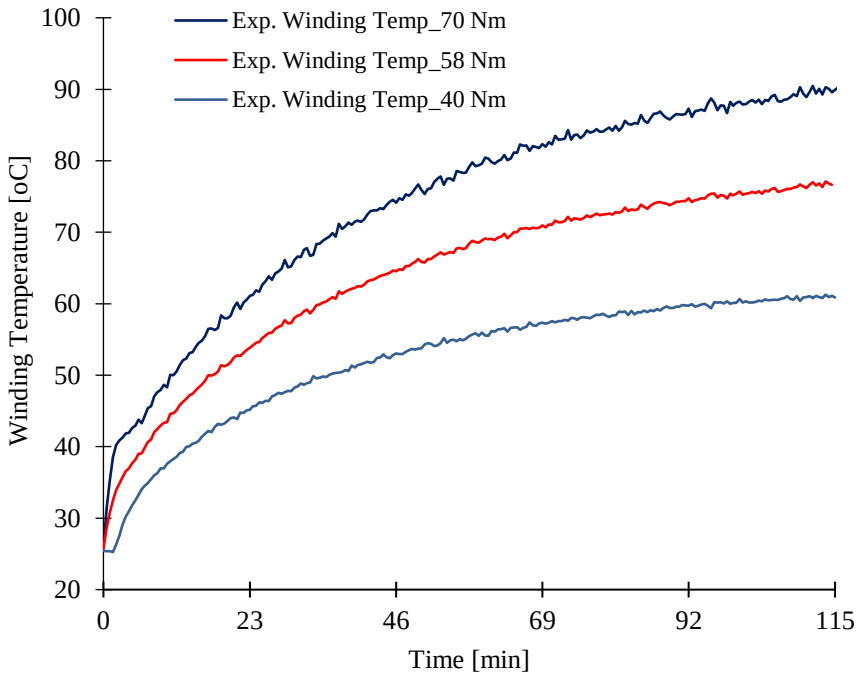

Figure 5.9. Winding temperature for different loading conditions.

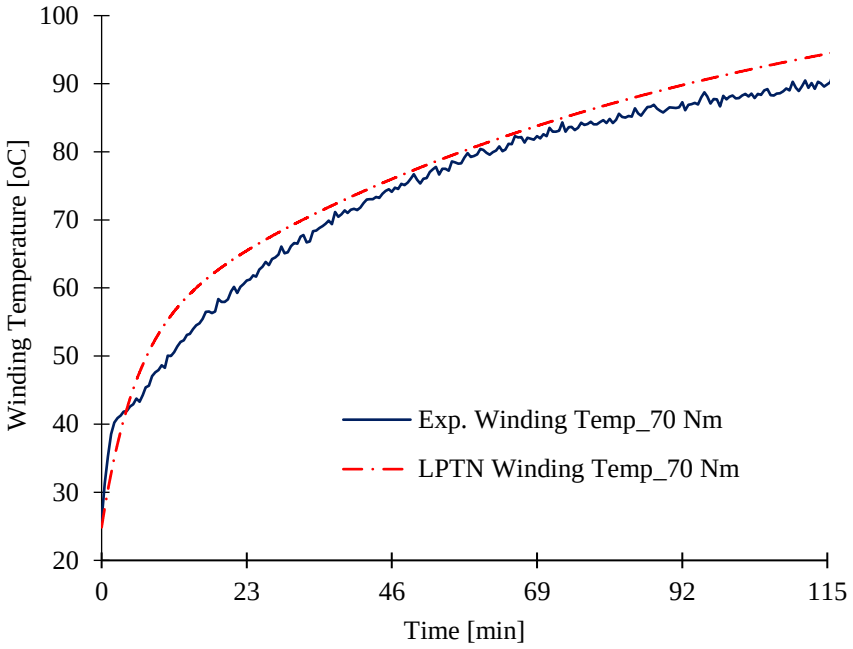

Figure 5.10. Winding temperature for 70 Nm loading torque.

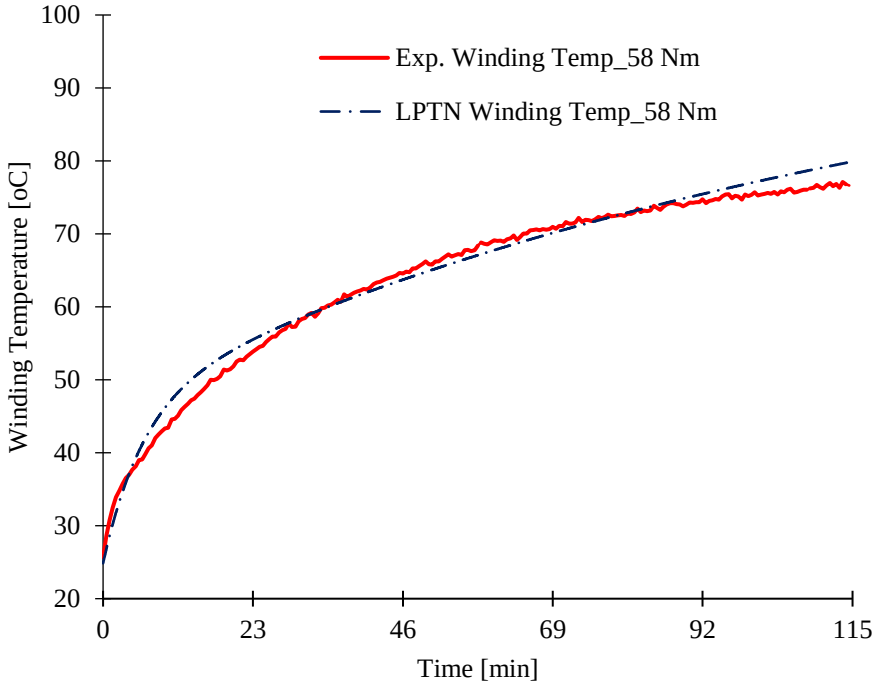

Figure 5.11. Winding temperature for 58 Nm loading torque.

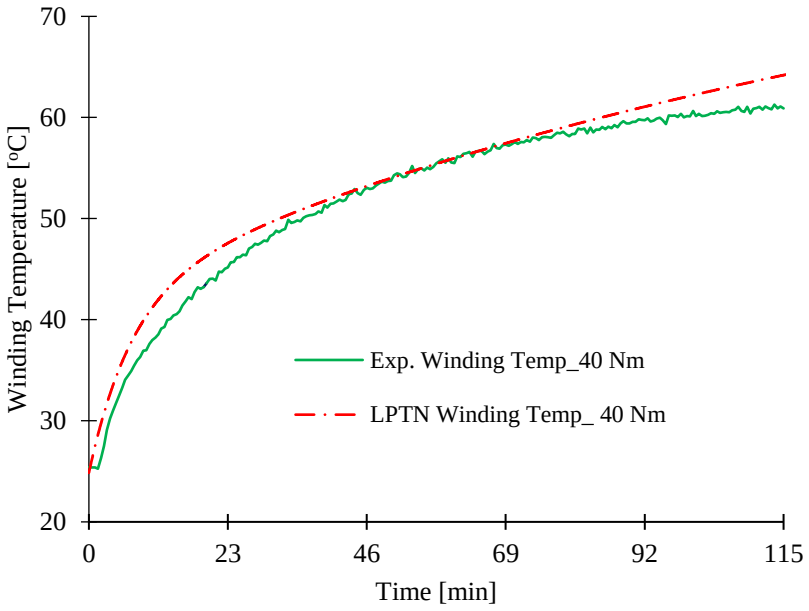

Figure 5.12. Winding temperature for 40 Nm loading torque.

Figure 5.9 shows actual temperature rise of stator winding for three different loading conditions. As expected, higher loading causes higher temperature rise than other loading conditions over two-hour period. It is important to note that no fan cooling was used during loading experiment. In order to compare LPTN calculated winding temperature with experimental winding temperature LPTN model was set to natural convection. Natural convection was achieved by setting the air velocity of less than 0.5 m/s. In this case, the motor was assumed to dissipate heat from its motor casing through natural convection only. Figure 5.10, 5.11 and 5.12 compare LPTN predicted winding temperature with experimental temperature and they agree very closely. For all loading conditions, winding temperature rises to around 100^{o}C, 80^{o}C and 60^{o}C respectively. These temperatures are not the steady state temperature and at rated loading torque of 70 Nm, winding temperature can increase even as high as more than 120^{o}C. The design temperature of the motor insulation was 120^{o}C. Hence, the prototype is reaching design temperature in 2-hour period without the use of any type of active cooling at rated condition. Fig. 5.13 shows the effect of forced cooling from a simulated fan on the winding temperature which is almost 20^{o}C difference in 2-hour period. This difference is significant enough to justify proper cooling requirements for the newly designed motor. These temperature data can be used to further

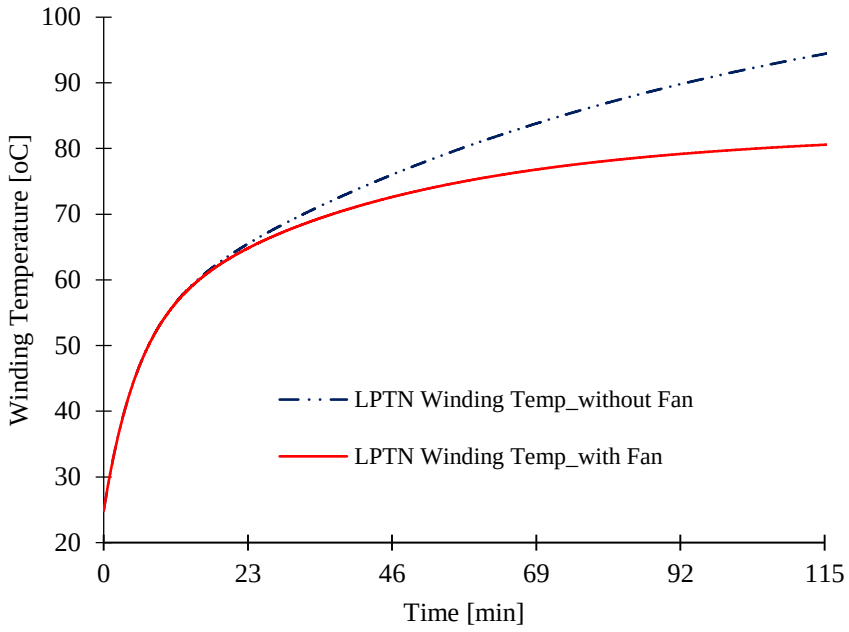

Figure 5.13. Winding temperature with/without fan cooling.

optimize the electromagnetic design of the motor. On the other hand, in electric vehicle application, air cooling would be very challenging to meet the cooling requirements for two reasons: (a) high torque density motor is very compact and requires higher cooling rate within smaller space (b) ambient conditions also constantly changes which will never be able to maintain higher cooling efficiency. As a result, the motor windings and other components like magnets will experience elevated temperature frequently which will not only reduce the electromagnetic performance of the motor as well as it will reduce the overall lifecycle of the motor. Considering the compactness of the motor with high torque and power density liquid cooling is a feasible option for electric vehicles.

5.5.2 LPTN Results – Liquid Cooling

The following section demonstrates suitability of the liquid cooling to be used for electric vehicle applications. In a compact space, liquid cooling can be designed to achieve required cooling for the traction motor. For simplicity of the liquid cooling analysis in this work, LPTN includes a cooling block in MATLAB Simulink that simulates removal of certain amount of heat by the cooling channels. Table 5.5 shows the heat removal by liquid (water-glycol mixture) cooling from the motor as a percentage of the total motor loss. If it is 90%

TABLE 5.5

HEAT REMOVAL BY THE LIQUID COOLING IN LPTN MODEL

Heat Removal (% of the total power loss of 256 Watts)			
90%	80%	70%	60%
230 W	205 W	179 W	154 W

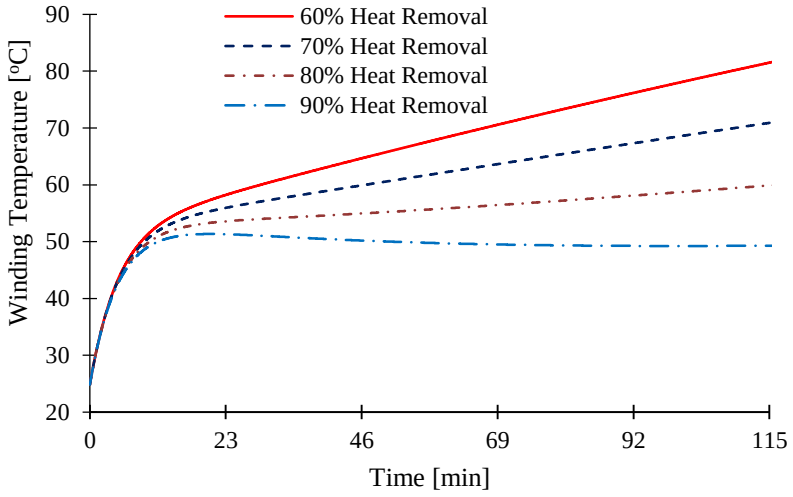

Figure 5.14. Winding temperature for different heat removal.

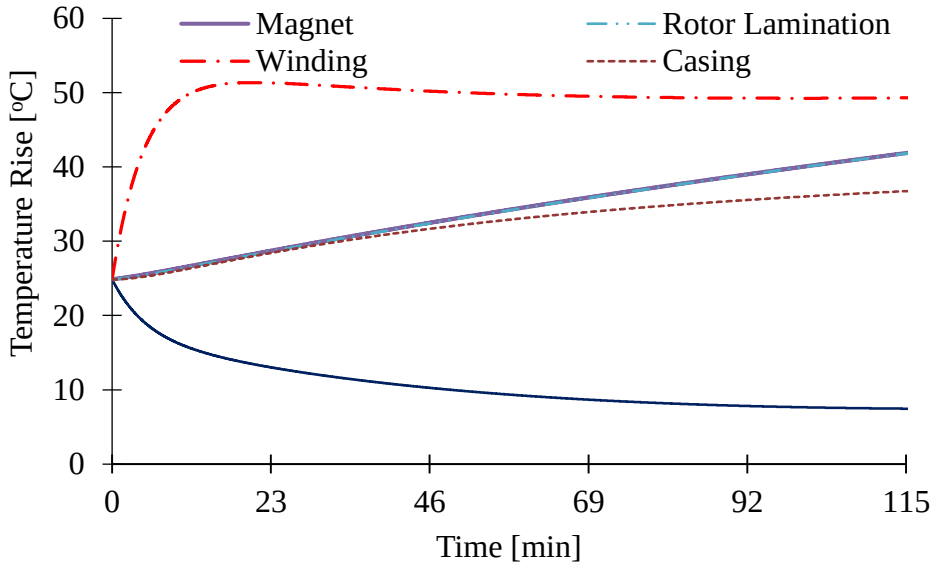

Figure 5.15. Motor parts temperature for 60% heat removal.

heat removal that means water-glycol cooling removes 90% equivalent heat generated by the 90% of the total power loss in the motor. LPTN model predicts the winding temperature for different heat removal rates which are shown in Figure 5.14. For 90% heat removal winding temperature is around 50^{o}C in the beginning and starts cooling off even at lower temperature around 40^{o}C in two-hour period. As a result, motor component temperatures as shown in Figure 5.15 clearly demonstrate that 90% heat removal is much higher than required cooling for the motor. In this case, 80% heat removal maintains steady state temperature of around 60^{o}C for this prototype. Based on the values of 80% heat removal, cooling channels can be designed and optimized.

5.6 Conclusion

In this paper, a computationally efficient LPTN model is proposed for thermal characterization of the motor. LPTN predicts temperature of all motor components to justify cooling requirements of the motor at varying loading conditions. LPTN modelling tool is an efficient and faster technique to calculate the temperature of the winding and magnet based on input of motor operating parameters, key physical dimensions of the motor parts and their thermal properties. The proposed model is validated through experimental investigations. The key objectives that are met in this work are (1) a simplified and computationally efficient LPTN model is developed to calculate motor temperature (2) predicted results from the model identifies shortfall of fan cooling for high torque and power applications (3) liquid cooling results justifies its effectiveness and suitability for high torque and power applications (4) LPTN determines thermal parameter that will be used to develop algorithm for thermal model-based motor protection mechanism.

The proposed integrated model will easily be integrated into drive model of the motor. This will take input of electrical operating parameters dynamically following the loading torque determined by the drive cycles and generate loss profile for LPTN thermal model to calculate stator winding and magnet temperature. The model will identify the need for cooling requirements by the motor for a specific loading torque and regulate the coolant flow rate to bring down the temperature of the stator winding and magnet, as needed. The model is suitable for any size of the motor as this requires only key physical dimensions of the stator and rotor parts of the motor.

5.7 References

[1] F. Ahmed and N. C. Kar, “Analysis of End-winding Thermal Effects in a Totally Enclosed Fan Cooled Induction Motor with Die Cast Copper Rotor,” *IEEE Transactions on Industry* Applications, vol. 53, no. 3, pp. 3098 – 3109, 2017.

[2] R. M. Tallam, S. B. Lee, G. C. Stone, G. B. Kilman, J. Yoo and T.G. Habetler “A Survey of Methods for Detection of Stator-Related Faults in Induction Machines” IEEE Transactions on Industry Applications, volume 43, no 4, July/August 2007.

[3] P. Zhang, Y. Du and T. G. Habetler, “A Transfer-Function-Based Thermal Model Reduction Study for Induction Machine Thermal Overload Protective Relays” IEEE Transactions on Industry Applications, volume 46, No. 5, 2010.

[4] A. Boglietti and A. Cavagnino, "Analysis of the end-winding cooling effects in TEFC induction motors," IEEE Transactions on Industry Applications, volume 43, issue 5, pp. 1214-1222, 2007.

[5] C. Micallef, S. J. Pickering, K. Simmons, and K. Bradley, "Improvements in air flow in the end region of a large totally enclosed fan cooled induction motor," Proc. of IEMDC'05 IEEE International Electric Machines and Drives Conference, San Antonio, May 2005.

[6] A. Boglietti, A. Cavagnino, D. Staton, M. Popescu, C. Cossar, and M.I. McGilp, “End space heat transfer coefficient determination for different induction motor enclosure types”, IEEE Trans. on Industry Applications, vol. 45, No. 3, May/June 2009, pp. 929-937

[7] E. Schubert, "Heat Transfer Coefficients at End Windings and Bearing Covers of Enclosed Asynchronous Machines," Elektrie, vol. 22, April 1968. pp160-162. (Translation ERA/IB 2846).

[8] A. Boglietti, A. Cavagnino, D. Staton, and M. Popescu, “Impact of different end region cooling arrangements on endwinding heat transfer coefficients in electric motors,” Proc. IEEE Conf. on Industrial Electronics, 978-1-4244-4649-0/09.

[9] A. Boglietti, A. Cavagnino, M. Lazzari, and M. Pastorelli, “A simplified thermal model for variable speed self cooled industrial induction motor,” IEEE Transactions on Industry Applications, volume.39, No.4, July/August 2003, pp. 945-952.

[10] D. A. Staton and A. Cavagnino, “Convection Heat Transfer and Flow Calculations Suitable for Electric Machines Thermal Models, Member, IEEE Transactions on Industrial Electronics, vol. 55, no. 10, October 2008.

[11] C. Micallef, S. J. Pickering, K. A. Simmons, and K. J. Bradley, "An Alternative Cooling Arrangement for the End Region of a Totally Enclosed Fan Cooled (TEFC) Induction Motor," 4th IET Conference on Power Electronics Machines and Drives, pp. 309-309, (2008).

[12] F. Ahmed, E. Ghosh, and N.C. Kar, " Transient Thermal Analysis of a Copper Rotor Induction Motor using a Lumped Parameter Temperature Network Model," in IEEE Transportation Electrification Conference and Expo (ITEC), June 2016.

[13] J.P., Holman. ‘‘Heat Transfer” 9th ed., McGraw-Hill, 2002, pp. 640-647.

[14] S. Mukundan, H. Dhulipati, L. Chauvin, A. Edrisy, J. Tjong, and N.C. Kar, “Comparative Performance Analysis of Copper and Aluminum Wound Fractional-slot PMSMs for High-speed Traction Application,” presented at the IEEE 22nd ICEMS, Harbin, China, August 2019.

[15] F. Ahmed, P. Roy, M. Towhidi, G. Feng and N. C. Kar, “CFD and LPTN Hybrid Technique to Determine Convection Coefficient in End-winding of TEFC Induction Motor with Copper Rotor,” accepted for IEEE 45th Annual Conference of Industrial Electronics Society, Portugal, October 2019

[16] J. Pyrhonen, T. Jokinen and V. Hrabovcova, “Design of Rotating Electric Machines”, 2008 John Wiley & Sons, Ltd. ISBN: 978-0-470-69516-6.

[17] E. Ghosh, F. Ahmed, A. Mollaeian, and N. C. Kar, “Online Parameter Estimation and Loss Calculation using Duplex Neural-Lumped Parameter Thermal Network for Faulty Induction Motor,” in Proc. of the IEEE Conference on Electromagnetic Field Computation, Florida, 2016.

[18] F. Ahmed, E. Ghosh, and N. C. Kar, “Transient Thermal Analysis of a Copper Rotor Induction Motor using a Lumped Parameter Temperature Network Model,”in Proc. of the IEEE Transportation Electrification Conference, Michigan, USA, 2016.

[19] E. Ghosh, F. Ahmed, N. C. Kar, “Temperature Influenced Online Stator Resistance Estimation Using an Improved Swarm Intelligence Technique for Induction Machine,” in proc. of IEEE Transportation Electrification Conference and Expo, 2015.

[20] K. Hafiz, G. Nanda and N.C. Kar, “Comparative Performance Analysis of Aluminum Rotor and Copper Rotor SEIG Considering Skin Effect,” Proc. of the IEEE International Conference on Electric Machines, Portugal, September, 2008.

CHAPTER 6

DISCUSSIONS AND CONCLUSIONS

6.1 Discussions and conclusions

First, in this thesis a higher order comprehensive lumped parameter thermal network model was proposed and developed to perform thermal analysis of copper rotor induction motor, one of the two commonly used traction motors in EV application. The proposed higher LPTN model included thermal resistances and thermal capacitances of the different material of the motor parts to determine temperature of the winding and other parts in transient perspective. Detailed calculations of thermal parameters in LPTN model were presented in this research work to understand LPTN model efficiency in calculating motor temperatures. Also, a 1st order thermal model which is generally used in thermal model-based protection technique in the industry applications was compared with higher order proposed LPTN model that considers all the motor losses to produce accurate temperature results. This comparison demonstrated that higher order LPTN model-based thermal protection will be the most reliable technique over exiting other motor thermal protection techniques.

Furthermore, it was identified that determination of one of the thermal parameters, end-winding convection coefficient in the proposed LPTN model was a challenging task. The reason was the complex nature of air circulation due to rotation of the rotor in the end-region enclosed space of the motor end-winding. In addition, it was investigated that differences in the rotor geometry was an additional factor to influence this end-winding air circulation for both copper rotor induction motor and permanent magnet induction motor as they do not have any rotor fins on its end-rings like an aluminum rotor induction motor. This research proposed a hybrid LPTN and CFD technique and determined convection coefficients in the end-winding for the motor that has no fins on its rotor end-rings. The results were further generated for the motor with any rotor and end-winding sizes.

Once, a higher order LPTN model was developed and validated then a simplified higher order LPTN model was proposed for interior permanent magnet synchronous motor, widely used another traction motor. The primary focus was to develop two part of the

integrated LPTN model, part one was motor loss model and the other was thermal model. Both models were created in MATLAB Simulink to increase the efficiency of model calculations. This integrated model was capable to take inputs dynamically of motor operating parameters such as torque, speed, voltage etc. and generate a loss model that was fed into a thermal LPTN model to produce temperature of magnets, stator winding and other components of the motor. Also, the proposed model included a motor liquid cooling block that was regulated and varied to deliver required cooling so that the motor could continue to produce the rated and peak power and torque to satisfy driving conditions.

So, in summary, this research developed and validated a higher order integrated LPTN model to determine temperatures of copper rotor induction motor and permanent magnet synchronous motor. The following key objectives were met in this research work:

- Compared higher order LPTN model with 1st order LPTN model for CR-IM and determined the temperature difference of 20-25^{o}C and this comparison demonstrated that higher order LPTN model can offer the most reliable thermal model based motor thermal protection.
- Developed a hybrid LPTN and CFD model to calculate convection coefficient in the end-winding for the motors that do not have any fins or blades on its rotor end-rings and this model can be used with any motor size.
- Finally, a simplified computationally efficient integrated LPTN determines temperature of motor components and varied the cooling requirements in order to keep the temperature within the operating limit to maintain required torque and power generation.

6.2 Future work

The future work can be focused on i) testing and validating the proposed LPTN model for traction motors with varying size and dimensions ii) developing a thermal-model based motor protection algorithm using proposed LPTN model iii) integrating LPTN model algorithm into motor drive models to test for thermal characterization and protection of different traction motors for varying drive cycles iv) refining LPTN model algorithm in order to be used dynamically in electric vehicle application.

APPENDICES

Appendix A: List of Publications

A.1. Published peer-reviewed Journal and Conference papers during my tenure as a graduate student at the University of Windsor

1. **F. Ahmed**, N. C. Kar, "Analysis of End-Winding Thermal Effects in a Totally Enclosed Fan-Cooled Induction Motor with a Die Cast Copper Rotor," IEEE Transactions on Industry Applications, Vol. 53, No. 3, May 2017.

2. **F. Ahmed**, E. Ghosh, M. Towhidi, S. Mukundan, H. Dhulipati, and N. C. Kar, "LPTN Modelling for Thermal Characterization and Protection of an Interior Permanent Magnet Synchronous Motor (IPMSM) for Electric Vehicle Application.," submitted in the Journal of Engineering (IET), JOE-2019-1294.

3. **F. Ahmed,** P. Roy, M. Towhidi, G. Feng and N. C. Kar, "CFD and LPTN Hybrid Technique to Determine Convection Coefficient in End-winding of TEFC Induction Motor with Copper Rotor," IECON - 45th Annual Conference of the IEEE Industrial Electronics Society, Portugal, October 2019.

5. P. Roy, A. Bourgault, **F. Ahmed**, M. Towhidi, S. Mukandan, H. Dhulipati, E. Ghosh, N. C. Kar "Thermal Representation of Interior and Surface Mounted PMSMs for Electric Vehicle Application," IECON - 45th Annual Conference of the IEEE Industrial Electronics Society, Portugal, October 2019.

6. P. Roy, M. Towhidi, **F. Ahmed,** A. J. Bourgault, S. Mukandan, A. Balamurali, and N. C. Kar. "A Comprehensive Review of Thermal Design and Analysis of Traction Motors," 28th International Symposium on Industrial Electronics (ISIE), June 2019.

7. **F. Ahmed**, E. Ghosh, S. Mukundan, H. Dhulipati, and N. C. Kar, "LPTN and FEA Modelling for Thermal Characterization of an Interior Permanent Magnet

Synchronous Motor (IPMSM) for Electric Vehicle Application," Energy and Sustainability Conference, June 2018.

8. E. Ghosh, **F. Ahmed**, A. Mollaeian, J. Tjong and N. C. Kar, "Online Parameter Estimation And Loss Calculation Using Duplex Neural-Lumped Parameter Thermal Network for Faulty Induction Motor," in the proc. of 2016 IEEE Conference on Electromagnetic Field Computation (CEFC), pp. 1-1, Miami, FL, 2016.

9. **F. Ahmed**, E. Ghosh, and N. C. Kar, " Transient Thermal Analysis of a Copper Rotor Induction Motor using a Lumped Parameter Temperature Network Model," in the proc. of IEEE Transportation Electrification Conference and Expo (ITEC), June 2016.

10. E. Ghosh, **F. Ahmed**, N. C. Kar, "Temperature Influenced Online Stator Resistance Estimation Using an Improved Swarm Intelligence Technique for Induction Machine," in the proc. of IEEE Transportation Electrification Conference and Expo, 2015.

11. M. Towhidi, **F. Ahmed**, S. Mukundan, Z. Lee, and N. C. Kar, "Lumped Parameter Thermal Network Modelling for Online Temperature Prediction of Permanent Magnet Synchronous Motor for Different Drive Cycles in Electric Vehicle Applications," submitted for SAE World Congress, March 2020.

Appendix B: Industrial Collaborative Research

B.1. Industrial research contributions during my tenure as a graduate student at the University of Windsor

1. Development of Lumped Parameter Thermal Network Model for Permanent Magnet Synchronous Motor for Electric Vehicle. *NSERC-Engage: Collaboration with TM4 Electrodynamic Systems, Montreal, Canada.*

2. Development of Advanced Power Electronics Thermal Management. *BorgWarner, MI, USA.*

Appendix C: Permissions for Using Publication

Title: Analysis of End-Winding Thermal Effects in a Totally Enclosed Fan-Cooled Induction Motor With a Die Cast Copper Rotor

Author: Firoz Ahmed

Publication: Industry Applications, IEEE Transactions on

Publisher: IEEE

Date: May-June 2017

Copyright © 2017, IEEE

Logged in as:
Firoz Ahmed
LOGOUT

Thesis / Dissertation Reuse

The IEEE does not require individuals working on a thesis to obtain a formal reuse license, however, you may print out this statement to be used as a permission grant:

Requirements to be followed when using any portion (e.g., figure, graph, table, or textual material) of an IEEE copyrighted paper in a thesis:

1) In the case of textual material (e.g., using short quotes or referring to the work within these papers) users must give full credit to the original source (author, paper, publication) followed by the IEEE copyright line © 2011 IEEE.
2) In the case of illustrations or tabular material, we require that the copyright line © [Year of original publication] IEEE appear prominently with each reprinted figure and/or table.
3) If a substantial portion of the original paper is to be used, and if you are not the senior author, also obtain the senior author's approval.

Requirements to be followed when using an entire IEEE copyrighted paper in a thesis:

1) The following IEEE copyright/ credit notice should be placed prominently in the references: © [year of original publication] IEEE. Reprinted, with permission, from [author names, paper title, IEEE publication title, and month/year of publication]
2) Only the accepted version of an IEEE copyrighted paper can be used when posting the paper or your thesis on-line.
3) In placing the thesis on the author's university website, please display the following message in a prominent place on the website: In reference to IEEE copyrighted material which is used with permission in this thesis, the IEEE does not endorse any of [university/educational entity's name goes here]'s products or services. Internal or personal use of this material is permitted. If interested in reprinting/republishing IEEE copyrighted material for advertising or promotional purposes or for creating new collective works for resale or redistribution, please go to http://www.ieee.org/publications_standards/publications/rights/rights_link.html to learn how to obtain a License from RightsLink.

If applicable, University Microfilms and/or ProQuest Library, or the Archives of Canada may supply single copies of the dissertation.

BACK CLOSE WINDOW

Copyright © 2019 Copyright Clearance Center, Inc. All Rights Reserved. Privacy statement. Terms and Conditions.
Comments? We would like to hear from you. E-mail us at customercare@copyright.com

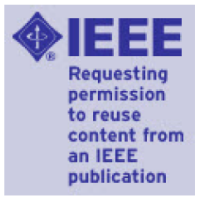

Title: Transient thermal analysis of a copper rotor induction motor using a lumped parameter temperature network model

Conference Proceedings: 2016 IEEE Transportation Electrification Conference and Expo (ITEC)

Author: Firoz Ahmed

Publisher: IEEE

Date: June 2016

Copyright © 2016, IEEE

Logged in as:
Firoz Ahmed
LOGOUT

Thesis / Dissertation Reuse

The IEEE does not require individuals working on a thesis to obtain a formal reuse license, however, you may print out this statement to be used as a permission grant:

Requirements to be followed when using any portion (e.g., figure, graph, table, or textual material) of an IEEE copyrighted paper in a thesis:

1) In the case of textual material (e.g., using short quotes or referring to the work within these papers) users must give full credit to the original source (author, paper, publication) followed by the IEEE copyright line © 2011 IEEE.
2) In the case of illustrations or tabular material, we require that the copyright line © [Year of original publication] IEEE appear prominently with each reprinted figure and/or table.
3) If a substantial portion of the original paper is to be used, and if you are not the senior author, also obtain the senior author's approval.

Requirements to be followed when using an entire IEEE copyrighted paper in a thesis:

1) The following IEEE copyright/ credit notice should be placed prominently in the references: © [year of original publication] IEEE. Reprinted, with permission, from [author names, paper title, IEEE publication title, and month/year of publication]
2) Only the accepted version of an IEEE copyrighted paper can be used when posting the paper or your thesis on-line.
3) In placing the thesis on the author's university website, please display the following message in a prominent place on the website: In reference to IEEE copyrighted material which is used with permission in this thesis, the IEEE does not endorse any of [university/educational entity's name goes here]'s products or services. Internal or personal use of this material is permitted. If interested in reprinting/republishing IEEE copyrighted material for advertising or promotional purposes or for creating new collective works for resale or redistribution, please go to http://www.ieee.org/publications_standards/publications/rights/rights_link.html to learn how to obtain a License from RightsLink.

If applicable, University Microfilms and/or ProQuest Library, or the Archives of Canada may supply single copies of the dissertation.

BACK CLOSE WINDOW

Copyright © 2019 Copyright Clearance Center, Inc. All Rights Reserved. Privacy statement. Terms and Conditions.
Comments? We would like to hear from you. E-mail us at customercare@copyright.com

VITA AUCTORIS

NAME:	Firoz Uddin Ahmed
PLACE OF BIRTH:	Bangladesh
YEAR OF BIRTH:	1975
EDUCATION:	Rajshahi College, Rajshahi, Bangladesh, 1992
	Rajshahi University of Engineering and Technology, Rajshahi, Bangladesh, B.Sc., 1998
	Carl Von Ossietzky University of Oldenburg, Germany, M.Sc., 2004